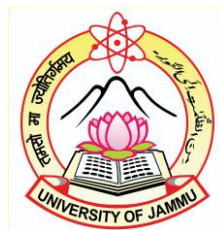# UNIVERSITY OF JAMMU, JAMMU 180006
DEPARTMENT OF PHYSICS

FINAL REPORT

F.No.-43-398/2014 (SR) Dated: 18 Sep. 2015 & 08 Dec. 2017
MAJOR RESEARCH PROJECT IN MATERIAL SCIENCE

PROJECT TITLE

$Cu(In_{1-x}Al_x)Se_2$ Thin Films Optimization and Device Fabrication for Photovoltaic Applications

PRINCIPAL INVESTIGATOR
Prof. Naresh Padha

Certificate of Declaration

I, Prof. Naresh Padha, declare that the work presented in this report is original and carried throughout independently by me during the complete tenure of the Major Research Project of UGC New Delhi.

Principal Investigator
Prof. Naresh Padha
Department of Physics
University of Jammu
Jammu-180006

UGC Sanction Letters

FD Diary No. - 3054
Dated - 20.08.2015

UNIVERSITY GRANTS COMMISSION
BAHADURSHAH ZAFAR MARG
NEW DELHI-110002

F. No. - 43-398/2014(SR)

Dated :- Sep, 2015

1 8 SEP 2015

MRP-MAJOR-MATE-2013-11424
(GENERAL)

The Under Secretary (FDIII),
University Grants Commission,
Bahadur Shah Zafar Marg,
New Delhi-110002.

Sub.:- Release of Grants-in-aid to **University of Jammu, Baba Saheb Ambedkar Road, Jammu-180006 J&K (INDIA)** for the year **2015-16** under Plan in respect of Major Research Project entitled **"Cu(In1-xAlx)Se2 Thin Films.......... Photovoltaic Applications "** awarded to **Prof. Naresh Padha (Material Science)** , **Department of Physics & Electronics** , Tenure of project for **3** year(s) w.e.f. **01/07/2015** .

Madam,

I am directed to convey the approval sanction of the University Grants Commision for payment of grant of **Rs. 9,65,000/-** (Rupees: **NINE LAKHS SIXTY FIVE THOUSAND ONLY**) as **1st instalment** for the years **2015-16** towards Major Research Project to the **REGISTRAR** , **University of Jammu, Baba Saheb Ambedkar Road, Jammu-180006 J&K (INDIA)** for the Plan expenditure to be incurred during **2015-16** .

S. No.	Items	Head of Account	Amount Approved(Rs.)	Grant being Released as 1st Installment(Rs.)	Grant Already Released(Rs.)	Total Grant(Rs.)
A.	**Non-Recurring**					
1.	Books & Journals	3(A).49(a).35	Rs. 0/-	Rs. 0/-	-	Rs. 0/-
2.	Equipment		Rs. 5,00,000/-	Rs. 5,00,000/-	-	Rs. 5,00,000/-
B.	**Recurring**					
1.	Honorium to Retd. Teacher @ Rs. 18,000/- p.m.		Rs. 0/-	Rs. 0/-	-	Rs. 0/-
2.	a. Project Fellow (Non-Gate/Non NET) @ Rs. 14,000/- p.m. b. Project Fellow (Gate/NET/GPAT) @ Rs. 16,000/- p.m. Tenure - 3 year(s)		Rs. 6,00,000/-	Rs. 3,00,000/-	-	Rs. 3,00,000/-
3.	Chemical/Glassware/Consumable (Raw Material & Packaging Material etc.)	3(A).49(a).31	Rs. 1,00,000/-	Rs. 50,000/-		Rs. 50,000/-
4.	Contingency		Rs. 30,000/-	Rs. 15,000/-	-	Rs. 15,000/-
5.	Hiring Services		Rs. 20,000/-	Rs. 10,000/-	-	Rs. 10,000/-
6.	Travel / Field Work		Rs. 30,000/-	Rs. 15,000/-	-	Rs. 15,000/-
7.	Any Other		Rs. 0/-	Rs. 0/-		Rs. 0/-
8.	Overhead Charges 10% of approved recurring Grant (Except Travel & Field Work)		Rs. 75,000/-	Rs. 75,000/-	-	Rs. 75,000/-
	Total (A + B)		Rs. 13,55,000/-	Rs. 9,65,000/-		Rs. 9,65,000/-

1. The sanctioned amount is debitable to the Major **Head 3(A).49(a).31 Rs. 4,65,000/- & Head 3(A).49(a).35 Rs. 5,00,000/-** and is valid for payment during financial year **2015-16** .

2. The amount of the Grant shall be drawn by the Under Secretary (Drawing and Distributing Officer), University Grants Commission on the Grants-in-aid Bill and shall be disbursed to and credited to the **REGISTRAR , University of Jammu, Baba Saheb Ambedkar Road, Jammu-180006 J&K (INDIA)** through Electronic mode as per the following details.

	Payment Details	
(a)	Bank Name & Address of Branch	**The Jammu & Kashmir Bank Ltd., J & k Bank, New University Campus, Jammu-180006**
(b)	Account No.	**0345010100000001**
(c)	Type of Account (SB/Current/Cash Credit)	**CURRENT**
(d)	IFSC Code	**JAKA0CANAAL**
(e)	MICR Code of Branch	**180051018**
(f)	Whether Bank Branch is RTGS or NEFT enabled? :	**Yes (RTGS/NEFT/Both)**
(g)	Name & Address of Account Holder	**The Registrar, University of Jammu, Jammu-180006**

3. The Grant is subject to the adjustment of the basis of Utilization Certificate in the prescribed performa submitted by the University/Colleges/Institution.

4. The University/College/Institution shall maintain proper accounts of the expenditure out of the grants which shall be utilized only on approved items of expenditure.

5. The University/Institution may follow the General Financial Rules, 2005 and take Urgent necessary action to amend their manuals of financial procedures to bring them in conformity with GFRs, 2005 and those don't have their own approved manuals on financial procedures may adopt the provisions of GFR's 2005 and instructions/guideline there under from time to time.

6. The Utilization Certificate to the effect that the grant has been utilized for the purpose for which it has been sanctioned shall be furnished to the University Grants Commission as early as possible after the close of the current financial year.

7. The assets acquired wholly or substantially out of University Grant Commission's grant shall not be disposed or encumbered of utilized for the purposes other than those for which the grant was given, without proper sanctioned of the University Grants Commission and should, at any time the College/University cease in function such assets shall revert to the University Grants Commission.

8. A register of assets acquired wholly or substantially out of the grant shall be maintained by the University/College in the prescribed proforma.

9. The grantee institution shall ensure the utilization of grant-in-aid for which it is being **sanction/paid**. In case non-utilization/part utilization, thereof simple interest @ 10% per annum as amended from time to time on unutilized amount from the date of drawl to the date of refund as per provisions contained in General Financial Rules of Govt. of India will be charged.

10. The University/College/Institute shall follow strictly the Government of India / University Grants Commission guidelines regarding implementation of the reservation policy **[both vertical (for SC, ST & OBC) and horizontal (for persons with disability etc.)]** in teaching and non-teaching posts.

11. The University/College shall fully implement the Official Language Policy of Union Govt. and comply with the Official Language Act, 1963 and Official Languages (Use for Official purposes of the Union) Rules, 1976 etc.

12. The sanction is issued in exercise of the delegation of powers vide University Grants Commission Office Order No. **69/2014 F.No.10-11/12 (Admn. IA & B) dated 26/03/2014** .

13. The University/Institution shall strictly follow the University Grants Commission Regulations on curbing the menace of Ragging in Higher Educational Institutions, 2009.

14. The University/Institution shall take immediate action for its accreditation by National Assessment & Accreditation Council (NAAC).

15. The accounts of the University/Institution will be open for audit by the Comptroller & Auditor General of India in accordance with the provisions of General Financial Rules, 2005.

16. The annual accounts i.e. balance sheet, income and expenditure statement and statement of receipts and payments are to be prepared strictly in accordance with the Uniform Format of Accounting prescribed by

Government.

17. It is certified from the B.C.R. that the funds are available under the scheme. Entered in BCR at S.No783 P. No. 47.

18. The funds to the extent of Rs. _____ Crores are available under the scheme or BE/RE of the year 2015-16.

19. This issue with the concurrence of IFD Vide No. Diary No. 10946 Dated, 10.03.2015 .

20. This issue with the approval of the Chairman, (UGC) Vide Diary No. 28731 Dated 30.04.2015 .

Yours faithfully,

(G.S. AULAK)
Under Secretary

Copy forwarded for information and necessary action to :-

1. The REGISTRAR , - A
2. Office of the Director General of Audit, Central Revenues, A.G.C.R. Building, I.P. Estate, New Delhi.
3. Accountant General, Govt. of State, Jammu and Kashmir .
4. Dr. Prof. Naresh Padha (Material Science) , Principal Investigator, Department of Physics & Electronics , University of Jammu, Baba Saheb Ambedkar Road, Jammu-180006 J&K (INDIA) .
5. The Principal, University of Jammu, Baba Saheb Ambedkar Road, Jammu-180006 J&K (INDIA)

Registrar

(ARUN KUMAR SINHA)
SECTION OFFICER

5

UNIVERSITY GRANTS COMMISSION
BAHADUR SHAH ZAFAR MARG
NEW DELHI 110002

ज्ञान-विज्ञान विमुक्तये

8 DEC 2017

(GENERAL)

F .No.43-398/2014(SR)   Dated: Nov, 2017

The Under Secretary (FD-III)
University Grants Commission
Bahadur Shah Zafar Marg
New Delhi – 110002

Sub: Release of Grant-in aid to **University of Jammu, Jammu** for the year 2017-18 under revenue in respect of Major Research Project entitled **"Cu(In1-xAlx)......................applications"** awarded to **Prof. Naresh Padha, Dept. of Material Science** tenure of the project from **01.07.2015 to 30.06.2018. (3 years)**

Sir,

I am directed to convey the sanction of the University Grants Commission for payment of grant of Rs. **1,48,726/-** **(Rupees One Lakh Forty Eight Thousand Seven Hundred Twenty Six Only)** as **2nd installment** for the year 2017-18 towards Major Research Project to **The Registrar, University of Jammu, Jammu** for the revenue expenditure to be incurred during 2017-18.

Name of the Item	Amount Allocated	Head of Account	Grant now Being Sanctioned	Grant already Released	Total Grant
Books & Journals	....	3.A (65)(a). 35	....	....	....
Equipment	5,00,000/-		....	5,00,000/-	5,00,000,
Project Fellow @ Rs. 14,000/-p.m for 2 years 16,000 p.m for 3rd year	4,18,581/-	3.A (65)(a). 31	76,726/-	3,00,000/-	3,76,726
Hr..	....		....	....	....
Contingency	30,000/-		12,000/-	15,000/-	27,000
Chemical	1,00,000/-		40,000/-	50,000/-	90,000
Hiring Services	20,000/-		8,000/-	10,000/-	18,000
Travel/ Field Work	30,000/-		12,000/-	15,000/-	27,000
Overhead Charges	75,000/-		....	75,000/-	75,000
Total	11,73,581/-		1,48,726/-	9,65,000/-	11,13,726

6

UNIVERSITY GRANTS COMMISSION
BAHADUR SHAH ZAFAR MARG
NEW DELHI 110002

8 DEC 2017

(GENERAL)

F .No.43-398/2014(SR)   **Dated: Nov, 2017**

The Under Secretary (FD-III)
University Grants Commission
Bahadur Shah Zafar Marg
New Delhi – 110002

Sub: Release of Grant-in aid to **University of Jammu, Jammu** for the year 2017-18 under revenue in respect of Major Research Project entitled **"Cu(In1-xAlx).....................applications"** awarded to **Prof. Naresh Padha, Dept. of Material Science** tenure of the project from **01.07.2015 to 30.06.2018. (3 years)**

Sir,

I am directed to convey the sanction of the University Grants Commission for payment of grant of Rs. **1,48,726/-** **(Rupees One Lakh Forty Eight Thousand Seven Hundred Twenty Six Only)** as **2nd installment** for the year 2017-18 towards Major Research Project to **The Registrar, University of Jammu, Jammu** for the revenue expenditure to be incurred during 2017-18.

Name of the Item	Amount Allocated	Head of Account	Grant now Being Sanctioned	Grant already Released	Total Grant
Books & Journals	....	3.A (65)(a). 35	....	....	....
Equipment	5,00,000/-		....	5,00,000/-	5,00,000
Project Fellow @ Rs. 14,000/-p.m for 2 years 16,000 p.m for 3rd year	4,18,581/-	3.A (65)(a). 31	76,726/-	3,00,000/-	3,76,726
Hr..			....	....	....
Contingency	30,000/-		12,000/-	15,000/-	27,000
Chemical	1,00,000/-		40,000/-	50,000/-	90,000
Hiring Services	20,000/-		8,000/-	10,000/-	18,000
Travel/ Field Work	30,000/-		12,000/-	15,000/-	27,000
Overhead Charges	75,000/-		....	75,000/-	75,000
Total	11,73,581/-		1,48,726/-	9,65,000/-	11,13,726

7

1. The sanctioned amount is debitable to **Major Research Project head 3.A (65) (a) 31** and is valid for payment during the financial year 2017-18 only.

2. The amount of the Grant shall be drawn by the Under Secretary (Drawing and Disbursing Officer) UGC on the Grants-in-aid bill and shall be disbursed to and credited to **The Registrar, University of Jammu, Jammu** through Electronic mode as per the following details:-

(a)	Bank Name & Address of Branch	The Jammu & Kashmir Bank Ltd., J & K Bank, new University Campus, Jammu-180006
(b)	Account no.	0345040160000001
(c)	Type of Account : SB /Current /Cash Credit	Cuurent
(d)	IFSC Code	JAKA0CANAAL
(e)	MICR Code	180051018
(f)	Whether Bank Branch is RTGS or NEFT enabled : RTGS / NEFT /Both	Yes
(g)	Name & Address of Account Holder	The Principal, University of Jammu, Jammu

3. The Grant is Subject to the adjustment on the basis of Utilization Certificate in the prescribed proforma submitted by the University / Institution.

4. The University / Institution shall maintain proper accounts of the expenditure out of the Grants which shall be utilized only on the approved items of expenditure.

5. The University / Institution may follow the General Financial Rules, 2005 and take urgent necessary action to amend their manuals of financial procedures to bring them in conformity with GFRs, 2005 and those don't have their own approved manuals on financial procedures may adopt the provisions of GFRs, 2005 and instructions / guidelines there under from time to time.

6. The Utilization Certificate to the effect that the grant has been utilized for the purpose for which it has been sanctioned shall be furnished to UGC as early as possible after the close of current financial year.

7. The assets acquired wholly for substantially out of University Grants Commission's Grant shall not be disposed or encumbered or utilized for the purposes other than those for which the grants was given without proper sanction of the UGC and should at any time the University ceased to function, such assets shall revert to the University Grants Commission.

8. A Register of Assets acquired wholly or substantially out of the grant shall be maintained by the University in the prescribed proforma.

9. The grantee institution shall ensure the utilization of grants-in-aid for which it is being sanctioned / paid. In case of non-utilization / part utilization thereof, simple interest @ 10% per annum, as amended from time to time on the unutilized amount from the date of drawal to the date of refund as per provisions contained in General Financial Rules of Govt. of India, will be charged.

10. The University / Institutions shall follow strictly the Government of India / UGS's guidelines regarding implementation of the reservation policy [both vertical (for SC,ST & OBC) and horizontal (for persons with disability etc.)] in teaching and non-teaching posts.

11. The University / Institution shall fully implement the Official Language Policy of Union Government and comply with the Official Language Act, 1963 and Official Languages (Use for Official Purposes of the Union) Rules, 1976 etc.

12. The sanction is issued in exercise of the delegation of powers vide UGC Order No. 69/2014 [F.No.10-11/12 (Admn. IA & B)] dated 26/3/2014.

13. The University / Institution shall strictly follow the UGC Regulations on curbing the menace of Ragging in Higher Education Institutions, 2009.

14. The University / Institution shall take immediate action for its accreditation by National Assessment & Accreditation Council (NAAC).

15. The accounts of the University / Institution will be open for audit by the Comptroller & Auditor General of India in accordance with the provisions of General Financial Rules, 2005.

16. The annual accounts i.e. balance sheet, income and expenditure statement and statement of receipts and payments are to be prepared strictly in accordance with the Uniform Format of Accounting prescribed by Government.

17. The grantee institution shall remit the amount of grants in aid and / or interest through e-mode (RTGS/NEFT) directly to UGC account as per following bank details:-

Account Holder	Secretary, UGC, New Delhi-110 002
Name of Bank & Address	Canara Bank, UGC Office, New Delhi-110 002
A/C No.	8627101002122
Type of A/C	Savings
IFSC Code	CNRB0008627
MICR Code	110015170

18. An amount of **Rs. 9,16,739/-** out the grant of **Rs. 9,65,000/-** sanctioned vide letter No.**F.43-398/2014(SR)** dated **18.09.2015** has been utilized by University/College/Institution for the purpose for which it was sanctioned. Utilization Certificate for **Rs. ....** has already been entered at S. No. ...... Now we may enter Utilization Certificate for **Rs. 9,16,739/-** S.No. 614 and in the U.C. Registrar at page No. 34...

19. Funds to the extent of Rs...... are available under the scheme or BE / RE of the year.

20. This issues with the concurrence of IFD vide Diary No. **3168** (IFD) dated **18.10.2017**.

21. This issues with the approval of Joint Secretary (MRP) vide Diary No. **49322** dated **01.11.2017**.

Yours faithfully,

(Suresh Rani)
Under Secretary

Copy forwarded for information and necessary action for :-

1. **The Registrar, University of Jammu, Jammu**
2. Office of the Director General of Audit, Central Revenues, AGCR Building, I.P. Estate, New Delhi.
3. Accountant General, State Govt. of **Srinagar, Kashmir**
4. **Prof. Naresh Padha, Dept. of Material Science, University of Jammu, Jammu**
5. Guard file.

(Arun Kumar Sinha)
Section Officer

9

MANDATE - FORM

ELECTRONIC CLEARING SERVICE (CREDIT CLEARING)/REAL TIME GROSS SETTLEMENT (RTGS) FACILITY FOR RECEIVING PAYMENTS

A. DETAIL OF ACCOUNT HOLDER

NAME OF THE ACCOUNT HOLDER	The Registrar, University of Jammu, Jammu.
COMPLETE CONTACT ADDRESS	1st Floor, New Administration Block, Babasaheb Ambedkar Road, New University Campus, Jammu Tawi, Jammu 180 006
TELEPHONE NUMBER/FAX/EMAIL	0191 – 2431365/2430935 manojkdhar@redifmail.com

B. BANK ACCOUNT DETAIL

BANK NAME	The Jammu & Kashmir Bank Ltd
BRANCH NAME WITH COMPLETE ADDRESS	J & K Bank, New University Campus, Jammu – 180 006.
TELEPHONE NUMBER AND EMAIL	0191 – 2458663/ canal@jkbmail.com
WHETHER THE BRANCH IS COMPUTERISED?	YES
WHETHER THE BRANCH IS RTGS ENABLED? IF YES, THEN WHAT IS THE BRANCH'S **IFCS CODE**	YES IFCS Code: JAKA0CANAAL
IS THE BRANCH ALSO **NEFT** ENABLED?	YES
TYPE OF BANK ACCOUNT (SB/CURRENT/CASH CREDIT)	CURRENT
COMPLETE BANK ACCOUNT NUMBR (LATEST)	0345010100000001
MICR CODE OF BANK	180051018
BRANCH CODE	0345

I hereby declare that the particulars given above are correct and complete. If the transaction is delayed or not effected to all for reason of incomplete or incorrect information I would not hold the user Institution responsible. I have read the option inviting letter and agree to discharge responsibility expected of me as a participant under the scheme.

(...............................)
Registrar
University of Jammu
REGISTRAR
University of Jammu
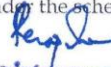
Date:

Certified that the particulars furnished above are correct as per our records.

(Bank's Stamp)

(...............................)
REGISTRAR
University of Jammu

Date:

1. Please attach a photocopy of cheque along with the verification obtained from the bank
2. In case your bank branch is presently not RTGS enabled,' then upon its up-gradation to "RTGS Enabled" branch, please submit the information again in the above proforma to the Department at earliest.

UNIVERSITY GRANTS COMMISSION
BAHADUR SHAH ZAFAR MARG
NEW DELHI – 110 002

STATEMENT OF EXPENDITURE IN RESPECT OF MAJOR RESEARCH PROJECT

1. Name of Principal Investigator : **Prof. Naresh Padha**

2. Deptt. of Principal Investigator: **Department of Physics & Electronics**

   University: **University of Jammu**, Jammu, J&K, India

3. UGC approval Letter No. and Date: **F.No. -43-398/2014(SR) Dated 18th Sep. 2015**

4. Title of the Research Project: **Cu(In1-xAlx)Se2 Thin Films optimization, Device Fabrication and their use in Photovoltaic Applications.**

5. Effective date of starting the project : **01/07/2015**

6. a. Period of Expenditure: From 16/08/2017 to 30/06/2018

   b. Details of Expenditure _____

S.No.	Item	Amount Approved (Rs.)	Amount Released as 2nd Instalment (Rs.)	Balance of Ist Instalment (Rs)	Total Amount (Rs.)	Expenditure Incurred (Rs.)	Balance (Rs.)
i.	Books & Journals	Nil	Nil	Nil	Nil	NIL	Nil
ii.	Equipment	5,00,000/-	Nil	Nil	Nil	Nil	Nil
iii.	Contingency	30,000/-	12,000/-	13/-	12,013/-	11,203/-	810/-
iv.	Field Work/Travel (Give details in the proforma at Annexure-IV).	30,000/-	12,000/-	1,821/-	13,821/-	NIL	13,821/-
v.	Hiring Services	20,000	8,000/-	Nil	8,000/-	8,000/-	Nil
vi.	Chemicals & Glassware	1,00,000	40,000/-	Nil	40,000/-	39,963/-	37/-
vii.	Overhead	75,000	Nil	233/-	233/-	Nil	233/-
viii.	Any other items (Please specify)	--	---	----	---		--
	Total	**7,55,000/-**	**72,000/-**	**2,067/-**	**74,067/-**	**59,166/-**	**14,901/-**

- Order has been placed and equipment been despatch by the company.

c. Staff *The equipment was commissioned in the lab and working satisfactorily.*

Date of Appointment: **27.01.2016**

S.No	Items	From	To	Amount Approved (Rs.)	Amount Released As 2nd Installment	Balance of Ist Instalment (Rs)	Total Amount (Rs.)	Expenditure incurred (Rs.)	Balance (Rs.)
1	Honorarium to PI (Retired Teachers) @ Rs. 18,000/-p.m.	Nil	Nil	Nil	Nil			Nil	Nil
2	**Project fellow:** i) **NET/GATE qualified-** Rs. 16,000/- p.m. for initial 2 years and Rs. 18,000/- p.m. for the third year. ii) **Non-GATE/Non-NET-** Rs. 14,000/-p.m. for initial 2 years and Rs. 16,000/-p.m. for the third year	01.08.2017	30.06.2018	6,00,000/-	76,726/-	46,194/-	1,22,920/-	1,22,920/-	Nil

1. It is certified that the appointment(s) have been made in accordance with the terms and conditions laid down by the Commission.

2. If as a result of check or audit objection some irregularly is noticed at later date, action will be taken to refund, adjust or regularize the objected amounts.

3. Payment @ revised rates shall be made with arrears on the availability of additional funds.

4. It is certified that the grant of **Rs. 01,48,726/- (Rupees One Lakh forty eight thousand seven hundred twenty six only)** received from the University Grants Commission under the scheme of support for Major Research Project entitled "Cu(In1-xAlx)Se2 **Thin Films optimization, Device Fabrication and their use in Photovoltaic Applications.** vide UGC letter No. **F.No. -43-398/2014(SR) Dated 18th Sep. 2015 and F.No. -43-398/2014(SR) Dated 8th Dec 2017 as 2nd instalment** with an amount of **Rs. 48,261/-** was carry forwarded and has been utilized for the purpose for which it was sanctioned and in accordance with the terms and conditions laid down by the University Grants Commission with an unspent balance of Rs. **14,901/-** .

SIGNATURE OF PRINCIPAL INVESTIGATOR

Prof Naresh Padha
Principal Investigator,
UGC-MRP,
Department of Physics & Electronics
University of Jammu
Jammu-180006

Registrar
University of Jammu
REGISTRAR/PRINCIPAL
12/6/19

(Seal)

UNIVERSITY GRANTS COMMISSION
BAHADUR SHAH ZAFAR MARG
NEW DELHI – 110 002

STATEMENT OF EXPENDITURE INCURRED ON FIELD WORK

Name of the Principal Investigator: Prof. Naresh Padha

Name of the Place visited	Duration of the Visit		Mode of Journey	Expenditure Incurred (Rs.)
	From	To		
---	---	---	---	Nil

Certified that the above expenditure is in accordance with the UGC norms for Major Research Projects.

SIGNATURE OF PRINCIPAL INVESTIGATOR

Prof Naresh Padha
Principal Investigator,
UGC-MRP,
Department of Physics & Electronics
University of Jammu
Jammu-180006

REGISTRAR/PRINCIPAL

Registrar
12/6/15

(Seal)

N.A.

SIGNATURE OF THE CO-INVESTIGATOR

UNIVERSITY GRANTS COMMISSION

BAHADUR SHAH ZAFAR MARG

NEW DELHI – 110 002

STATEMENT OF EXPENDITURE INCURRED ON FIELD WORK

Name of the Principal Investigator: Prof. Naresh Padha

Name of the Place visited	Duration of the Visit		Mode of Journey	Expenditure Incurred (Rs.)
	From	To		
SSPL, DRDO New Delhi	27.02.2017	02.03.2017	Air	13,179/-

Certified that the above expenditure is in accordance with the UGC norms for Major Research Projects.

SIGNATURE OF PRINCIPAL INVESTIGATOR

Prof Naresh Padha
Principal Investigator,
UGC-MRP,
Department of Physics & Electronics
University of Jammu
Jammu-180006

Registrar
University of Jammu
REGISTRAR/PRINCIPAL

(Seal)

14

UNIVERSITY GRANTS COMMISSION

BAHADUR SHAH ZAFAR MARG

NEW DELHI – 110 002

Utilization certificate

Certified that the grant of **Rs. 01, 48, 726/-** (Rupees One Lakh **forty eight thousand seven hundred twenty six only**) received from the University Grants Commission under the scheme of support for Major Research Project entitled <u>**Cu(In1-xAlx)Se2 Thin Films optimization, Device Fabrication and their use in Photovoltaic Applications**</u> vide UGC letter No. <u>**F.No. -43-398/2014(SR) Dated 18th Sep. 2015**</u> and **F.No. -43-398/2014(SR) Dated 8th Dec 2017 with an amount of Rs. 48,261/-** was carry forwarded, from a **total amount of Rs. 1, 96, 987/-** an amount of **Rs. 01, 82, 086/-** has been utilized for the purpose for which it was sanctioned and in accordance with the terms and conditions laid down by the University Grants Commission and a balance grant of **Rs. 14,901/-**has remained unspent.

**SIGNATURE OF THE
PRINCIPAL INVESTIGATOR**

Prof Naresh Padha
Principal Investigator,
UGC-MRP,
Department of Physics & Electronics
University of Jammu
Jammu 180006

REGISTRAR/PRINCIPAL

Registrar
of Jammu

(Seal)

STATUTORY AUDITOR

(Seal)

NA

SIGNATURE OF THE CO-INVESTIGATOR

PERFORMA FOR SUPPLYING THE INFORMATION IN RESPECT OF
THE STAFF APPOINTED UNDER THE SCHEME OF MAJOR
RESEARCH PROJECT

UGC FILE No. **F.No. -43-398/2014(SR) Dated 18th Sep. 2015**
Year of Commencement: **2015**

TITLE OF THE PROJECT: **Cu(In1-xAlx)Se2 Thin Films optimization, Device
Fabrication and their use in Photovoltaic Applications**

1.	Name of the Principal Investigator:	**Prof. Naresh Padha**				
2.	Name of The University	**University of Jammu**				
3.	Name of the Research Personal appointed	**Arun Banotra**				
4.	Academic qualification	**S.No.**	**Qualifications**	**Year**	**Marks**	**%age**
		1.	**M.Sc.**	**2013**	**1884/2400**	**78.50**
5.	Date of Joining	**28/01/2016**				
6.	Date of Birth of Research Personal	**10/07/1990**				
7.	Amount of HRA, if Drawn	**Nil**				
8.	Number of Candidates applied for the post	**06**				

CERTIFICATE

This is to certify that all the rules and regulations of UGC Major Research Project
outlined in the guidelines have been followed. Any lapses on the part of the
University will liable to terminate of said UGC project.

Principal Investigator   Head of the Department   Registrar

Head 11-5-19
F.G Deptt. of Physics
University of Jammu, Jammu

PERFORMA FOR SUPPLYING THE INFORMATION IN RESPECT OF THE STAFF APPOINTED UNDER THE SCHEME OF MAJOR RESEARCH PROJECT

UGC FILE No. **F.No. -43-398/2014(SR) Dated 18th Sep. 2015**
Year of Commencement: **2015**

TITLE OF THE PROJECT: **Cu(In1-xAlx)Se2 Thin Films optimization, Device Fabrication and their use in Photovoltaic Applications**

1.	Name of the Principal Investigator:	**Prof. Naresh Padha**				
2.	Name of The University	**University of Jammu**				
3.	Name of the Research Personal appointed	**Shafiq Ahmed**				
4.	Academic qualification	**S.No.**	**Qualifications**	**Year**	**Marks**	**%age**
		1.	**M.Sc.**	**2015**	**1393/2400**	**58.04**
5.	Date of Joining	**21/11/2017**				
6.	Date of Birth of Research Personal	**02/03/1987**				
7.	Amount of HRA, if Drawn	**Nil**				
8.	Number of Candidates applied for the post					

CERTIFICATE

This is to certify that all the rules and regulations of UGC Major Research Project outlined in the guidelines have been followed. Any lapses on the part of the University will liable to terminate of said UGC project.

Principal Investigator

Prof Naresh Padha
Principal Investigator,
UGC-MRP,
Department of Physics & Electronics
University of Jammu
Jammu-180006

Head of the Department

Head
P.G Deptt. of Physics
University of Jammu, Jammu

Registrar

UNIVERSITY GRANTS COMMISSION
BAHADUR SHAH ZAFAR MARG
NEW DELHI – 110 002

MAJOR RESEARCH PROJECT COPY OF THE SPECIMEN OF HOUSE RENT
FOR PROJECT FELLOW

Not Applicable

Certified that Shri/Dr._____ is paying House Rent of
Rs. _____ and is eligible to draw   House Rent Allowances
@_____ as per University Rules.

Registrar/Principal
(Signature with Seal)

Certified that Shri/Dr. _____ is not staying independently and
therefore is eligible to draw House Rent @ of Rs. _____p.m. minimum admissible to
a Lecturer as per University Rules.

Registrar/Principal
(Signature with Seal)

Certified that Shri/Dr. _____ has been provided
accommodation in the Hostel. But he/she could not be provided with single seated flat type
accommodation as recommended by the Commission, Hostel fee @
Rs._____ per month w.e.f. _____ is being charged from
him/her.

NOT APPLICABLE

Prof Naresh Padha
Principal Investigator,
UGC-MRP,
Department of Physics & Electronics
University of Jammu
Jammu-180006

Registrar/Principal
(Signature with Seal)

18

Month-Wise detailed Statement of Expenditure towards salary and HRA of the Project Fellow

Period for Which Salary drawn 01.08.2017 to 30.06.2018

Month & Year	Amount Drawn (Rs.)	HRA Drawn (Rs.)
August 2017	14,000/-	Nil
September 2017	12,133/-	Nil
October 2017	Nil	Nil
November 2017	4,667/-	Nil
December 2017	14,000/-	Nil
January 2018	14,000/-	Nil
February 2018	14,000/-	Nil
March 2018	14,000/-	Nil
April 2018	14,000/-	Nil
May 2018	14,000/-	Nil
June 2018	8,120/-	Nil
Total	**1,22,920/-**	**Nil**

SIGNATURE OF THE PRINCIPAL INVESTIGATOR

Prof Naresh Padha
Principal Investigator,
UGC-MRP,
Department of Physics & Electronics
University of Jammu
Jammu-180006

UNIVERSITY OF JAMMU

No: Grants/2020/ 825
Dated: 13/11/20

Prof. Naresh Padha
Principal Investigator, UGC MRP Project
University of Jammu

Sub:- Refund of the Unspent balance of Rs. 14901/- of the UGC MRP Project.

Sir,

    This is in response to your letter regarding the subject cited above. In this context, as desired by you, refund of unspent balance of Rs. 14,901/- has been done in favour of Secretary, UGC under the project" **Cu(In1-xAlx) Se2 films.....Photovoltaic Application**" through RTGS/NEFT vide instrument No. JAKA201112729531 dated 12/112020 of Jammu & Kashmir Bank, New University Campus Branch, Jammu.

    You are, therefore, requested kindly to acknowledge the receipt from UGC at the earliest so that the account of the above said project is closed properly.

    Thanking you,

Yours faithfully,

Deputy Registrar (Grants)

13/4

Copy to: -.
1. Sr. P. A. to J.R. (Finance).

20

The Jammu & Kashmir Bank Limited
Business Unit : New University campus, Jammu (J&K)-180006
T +91 (0)191 2458663 F E –canaal@jkbmail.com W www.jkbank.net

J&K Bank

Ref No.JKb/NUC/2021-

Dated: 19.01.2021

To Whom It May Concern

It is certified that University of Jammu is maintaining current with our branch bearing A/c No.0345010100000001 under the title REGISTRAR UNIVERSITY OF JAMMU having IFSC- JAKA0CANAAL, MICR Code- 180051018 and Branch Code-0345, operated by the Registrar, University of Jammu.

Since the said account is current in nature, therefore, no interest is earned on the same. The certificate is issued at the request of customer.

Yours faithfully

Branch Head
JK Bank
New University campus

REGISTRAR
University of Jammu.
Jammu.

21

Objectives :

i) The exploration of new material compositions, their constituent ratio, processing skills and device geometry to recommend future strategies for Schottky barrier and pn-heterojunction device applications. (Identification of metals which show ideal ohmic as well as Schottky contacts on to CIAS semiconductor, which can be possible by detailed analysis of barrier properties).

ii) The identification and control of defects or dislocations as well as strains which influence the electrical and/or optical properties of the films. Efforts shall be made to improve the quality of deposited films by optimizing processes and conditions for deposition.

iii) Given that devices of $CuIn_{1-x}Al_xSe_2$ are good candidates for space solar cells and other related optoelectronic applications. Attempts shall also be made to realize the Schottky barrier as well as heterojunction diodes by tailoring their bandgaps and analysing their temperature dependence response.

iv) The optimization of CIAS solar cells in terms of their absorption coefficient, fill–factor and efficiency will be undertaken to have better quality CIAS solar cells.

UNIVERSITY GRANTS COMMISSION
BAHADUR SHAH ZAFAR MARG
NEW DELHI – 110002

Final Report of the work done on the Major Research Project

1. **Project Report No. :** FINAL

2. **UGC Reference No.** F.No. -43-398/2014(SR) 18th Sep. 2015
   (Material Science)

3. **Period of report:** From 01/07/2015 to 30/06/2018

4. **Title of the research project:** $Cu(In_{1-x}Al_x)Se_2$ Thin Films optimization, Device Fabrication and their use in Photovoltaic Applications.

5. **(a) Name of the Principal Investigator:** Prof. Naresh Padha

   (b) Deptt. Physics & Electronics

   (c) University/~~College~~ where work has progressed:
   University of Jammu, Jammu-180006

6. **Effective date of starting of the project:** 01-07-2015

7. **Grant approved and expenditure incurred during the period of the report:**

   a. **Total Amount Approved Rs.** : 13,55,000/-

   b. **Total Amount Received Rs.** : 11,13,726/-

   c. **Total Expenditure incurred Rs. :** 10,98,825/-

   d. **Amount Refunded Rs.** : 14,901/-

   e. **Work done of the Project.** : (**separate sheet attached**)

   i. **Brief objective of the project:**

   - The exploration of new material compositions of Cu,In,Al, and Se precursurs, their constituent ratio, processing skills and device geometry to recommend future strategies for schottky barrier and pn-hetrojunction device applications.

- The identification and control of defects or dislocations as well as strains. The efforts shall be to improve the quality of deposited films by optimizing processes and conditions for deposition.

- Given that of $CuIn_{1-x}Al_xSe_2$ materials are good candidates for solar cells. Attempts shall also be made to optimise the layers quality – bandgap and absorption coefficient. The phenomenon of tailoring the bandgaps and analyze their temperature dependence will be undertaken..

- Thrust will be given to realize the schottky barrier as well as hetrojunction diodes and study their characteristics. The optimization of CdS/CIAS heterojunction solar cells in terms of their fill–factor and efficiency will be undertaken.

ii. Work done so far and results achieved and publication, if any, resulting from the work (Give details of the papers and names of the journals in which it has been published or accepted for publication).

1. Introduction

$CuAl_xIn_{1-x}Se_2$ (CIAS) chalcopyrite material attracted the research community due to the successful substitution of 'Al' into the CIS tetragonal lattice at 'In' sites, providing their better use in photovoltaic (PV) cells. The recent results have exhibited a solar cell efficiency (η) value of 23.35 $\pm$ 0.5 % for a Cd-free CIGS cell through optimization of the CIS absorber layer, which is better than multi-crystalline Si cells [1]. It is an alternative to CIGS's scarce and expensive gallium (Ga). The bandgap value of CIAS is controllable between 1.0 eV ($CuInSe_2$) to 2.7. eV ($CuAlSe_2$) by 'Al' substitution to 'In' sites [2]. The terrestrial PV applications accept an ideal bandgap of semiconductors as 1.37 eV[3]. Therefore, more attention is given to identifying an alternate absorber material that can offer a direct bandgap (E_g) ~ 1.4 eV with a high absorption coefficient value (α) ~10^5 cm^{-1}. Besides this, the material should be radiation-resistant and possess a considerable minority carrier diffusion length to get high-efficiency solar cells [4]. The mass production of $CuInAlSe_2$ and its launching into the market for use and reliability feedback is possible with low-cost, eco-friendly, easily scalable production. Various methods have been reported for the growth of CIAS thin films, viz. thermal evaporation, flash evaporation, co-evaporation of precursors, radio-frequency magnetron sputtering, DC magnetron sputtering, molecular beam deposition (MBD), chemical bath deposition (CBD), multi-source elemental

evaporation method (MSED), spray pyrolysis, electro-deposition, and pulsed laser deposition (PLD), etc [5-16]. The main problem in growing quaternary (CIAS) material thin films is the differences in constituents' physical parameters [7]. Most of the research reports are based on other methods which show the coexistence of secondary phases of $Cu_{11}In_9$, Cu_2Se, $CuSe$, Se, etc., or have weak reflections of chalcopyrite $CuInSe_2$ and $CuAlSe_2$ [16]. The SELD technique provides better control over the elemental fluxes during the film deposition. Moreover, it is one of the most appropriate techniques for developing large-area thin films [17]. Many researchers have attempted to remove the binary selenide and native oxide phases from CIS and CIAS thin layers that appeared on the selenisation of Cu-In and Cu-Al precursors in Ar, Se, and H_2Se environments [9,18]. However, excessive use of selenium, toxic H_2Se, and contamination caused by using separate chambers for selenisation are vital issues in the growth of chalcopyrite thin films [19].

In the present research, Cu, In, Al, and Se elemental layers were grown on the corning glass substrate using the SELD technique to achieve the $CuAl_xIn_{1-x}Se_2$ from the Cu/In/Al/Se stack. In the undertaken work, the structural, optical, morphological, and compositional studies of $CuIn_{1-x}Al_xSe_2$ are reported. Furthermore, the $FTO/p-CuInAlSe_2/n-CdS/In$ heterojunction diodes were studied for rectifying behaviour. In addition, the structure of the photovoltaic cell using a nano-polycrystalline p-CIAS absorber layer was tested.

2. Experimental Section/Methods

The copper, indium, aluminum, and selenium materials having a purity range of 99.995-99.999 are deposited sequentially with thicknesses values of 90, 190, 13, and 430 nm, respectively, to achieve the desired stoichiometry for $CuIn_{0.63}Al_{0.37}Se_2$ (Fig. 1). The layer depositions are obtained on corning glass substrates at room temperature in a vacuum coating unit 12A4DM (HindiVac, India) under vacuum ~ $2x10^{-6}$ mbar. The pre-deposition cleaning of glass substrates is carried out by dipping the substrates into hydrogen peroxide (H_2O_2) solution for ten minutes and its further processing in trichloroethylene, acetone, and methanol (TAM) for ten minutes each in a hot ultrasonic bath. The rotary motor attached to the substrate holder rotates the substrate during the deposition of the elemental layers to get the homogeneous layers. The evaporation rate of elemental Cu, In, Al, and Se corresponds to 1-2 Å/s, 2-3 Å/s, 1-3 Å/s, and 3-4 Å/s, respectively. The thickness of in-situ grown elemental layers is monitored with the help of thickness monitor DTM-101 (HindiVac, India) using a quartz crystal sensor attached to the vacuum coating unit. The post-deposition annealing was performed in VCU at 523 K for 1 hour(h) under vacuum ~ $1x10^{-5}$ mbar. The annealing has also been carried out in a muffle

tubular furnace at a vacuum ~ 10^3 mbar from 523 to 623 K for 2h at each temperature. DekTak 150 (Veeco) profilometer is used for the thickness measurement of the layers. X'pert^3 (PANalytical) Powder X-ray diffractometer was used to record the diffraction data of the layers in line mode at a scan speed of 0.03^0/s in 2θ range of 10^0-70^0. The diffractometer is equipped with HD Bragg Brentano incident geometry utilizing filtered $CuK_{\alpha 1}$ radiations (λ=1.5406 Å). The scanning electron microscope SUPRA-55 (Zeiss) at an acceleration voltage of 5 kV was used to determine the surface morphology. The average grain size and surface area were measured from SEM micrographs using ImageJ software (NHI & LOCI, University of Wisconsin, USA). The elemental composition of the constituents in the films was established using the K-emission line (copper and aluminum) and L-emission line (selenium and indium) using energy dispersive X-ray analysis attachment JEOL JSM-7426 (Oxford Instruments). The transmission spectra were recorded from UV-Vis-NIR spectrophotometer UV-3600 (Shimadzu) at room temperature with a slit width of 2 nm in the 300-1800 nm wavelength range. The Raman spectra are obtained using a laser excitation source of 532 nm in the wavenumber range of 100-300 cm^{-1} from a LabRam HR Evolution spectrometer (HORIBA). The heterojunction diode's current-voltage (I-V) characteristics are recorded using source meter 2400 (Keithley), probe station (Miller Design Corp), and open-source I-V software developed by Michael D. Kelzenberg. The open-circuit voltage (V_{oc}) of the FTO/p-CIAS/n-CdS/In heterojunction photocell is calculated using a digital multimeter VC-203 (Victor). The experimental data were analyzed using OriginLab 8.5 (MicroCal) software.
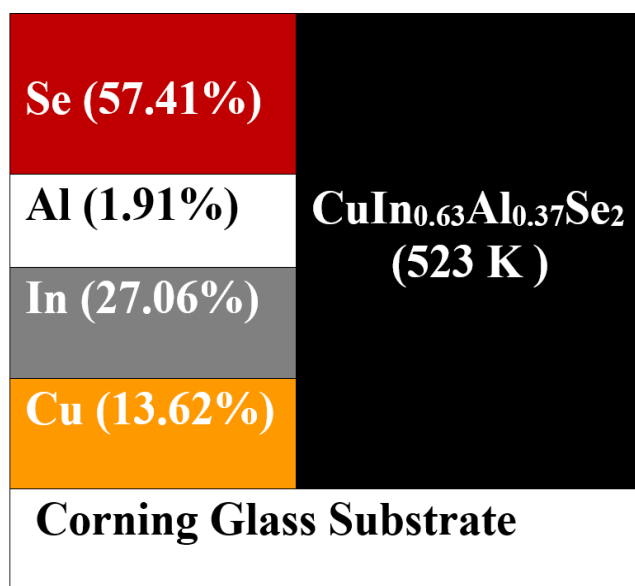
Fig. 1: The schematic diagram of the stack obtained by sequentially evaporated layered deposition (SELD) and $CuIn_{0.63}Al_{0.37}Se_2$ thin layers obtained on annealing at 523 K.

3. Results and Discussion

3.1. Structural Characterisation

The post-deposition thermal treatment of the sequentially evaporated layered deposition (SELD) stack was undertaken to understand the material's phase transformation to obtain CIAS thin layers.

3.1.1 Effect of high vacuum annealing

Thin films of CIAS re-grown at 523 K on annealing exhibit three intense peaks along (112), (220), and (312)/(116) orientations and provides a tetragonal structure having space group $1\bar{4}2d(122)$ (Fig. 2). As no standard JCPDS card is available for CIAS; consequently, the JCPDS cards of CuInSe$_2$ (CIS) (JCPDS: 40-1478) and CuAlSe$_2$ (CAS) (JCPDS: 44-1269) are considered to determine the CIAS phase. An emergence of (101) and (103) planes was also observed on substitution of 'Al' at 'In' sites in the chalcopyrite (tetragonal) structure at 523 K [9]. Several researchers have already reported the different concentrations of 'Al' in CuIn$_{1-x}$Al$_x$Se$_2$ [7-9].

The unit cell parameters (a=b, c) of the tetragonal structure were evaluated using the relation given in Eq. 1 [20].

$$\frac{1}{d^2} = \frac{h^2 + k^2}{a^2} + \frac{l^2}{c^2} \qquad (1)$$

Where h, k, l are Miller indices, d is the interplanar separation between lattice planes, and a,b, and c are unit cell parameters.
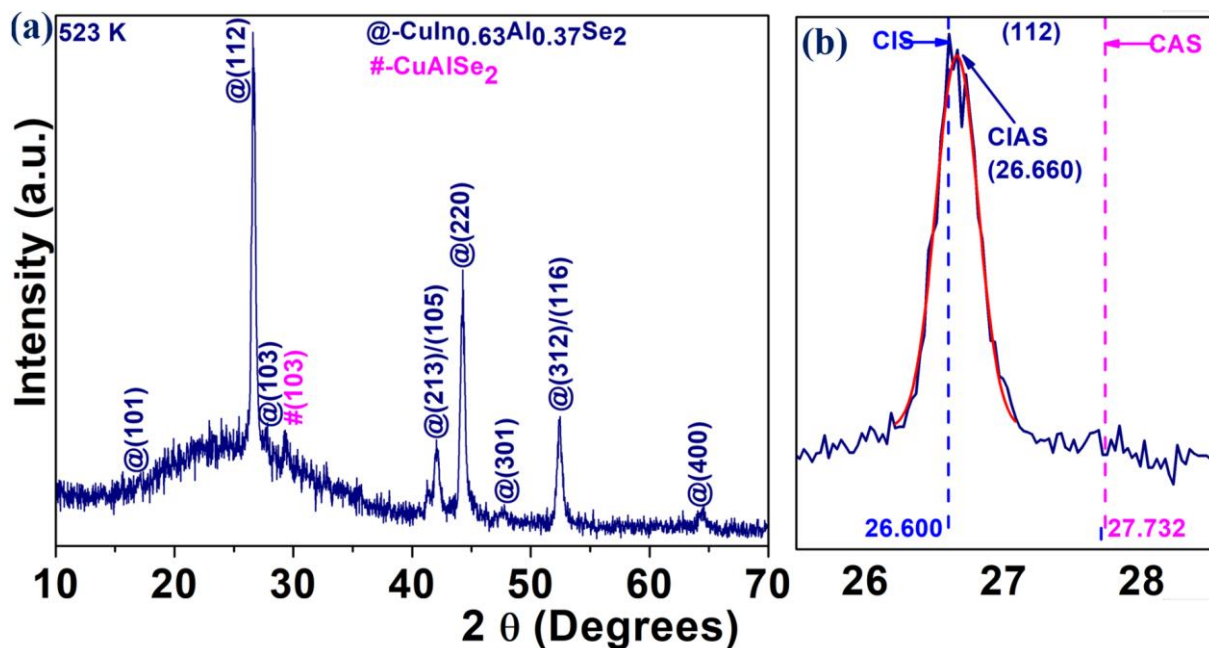
Fig 2: (a) The XRD plot of $CuIn_{0.63}Al_{0.37}Se_2$ thin films of 700 nm annealed at 523 K for 1h in a vacuum coating unit ~ $1x10^{-5}$ mbar, (b) magnified view of the (112) peak.

The grown CIAS films possess a tetragonal crystal system having unit cell parameters: a,b; 5.781(5) Å, c; 11.593(7) Å, and cell volume (V)=387.523(4) $Å^3$. The grown layers' average crystallite size (D) is calculated using the Debye Scherrer represented in Eq. 2 [20].

$$D = \frac{0.9\ \lambda}{\beta\ Cos\theta} \qquad (2)$$

Where λ represents the wavelength of X-rays, β (radians) is the full width at half maximum (FWHM), and θ is the Bragg's angle.

The average particle size of the CIAS corresponding to the most prominent peak (MSP) along (220) planes is 25.66(1) nm (Table 1). The shift in 2θ to the higher value of 26.660(1) from CIS in the (112) planes was observed [8]. At the same time, the unit cell volume of CIAS { 387.523(4) $Å^3$} is smaller than the unit cell volume of CIS {390.182(3) $Å^3$} (Table 2). The reduction in the cell volume of CIAS to that of CIS confirms the substitution of smaller atomic radii (125 pm) of 'Al' to higher radii of 'In' (155 pm) [21], which exhibits compressive stress in CIAS unit cells.

Table 1. The (hkl), 2θ, peak intensity, FWHM, and the crystallite size of thin films of ~ 700 nm of $CuIn_{1-x}Al_xSe_2$ obtained on annealing at 523-623 K for 1h and 2h.

Sample details	plane	2θ (Degrees)	Intensity	FWHM (degrees)	Crystallite size (nm)	Dislocation density (δ) $(x10^{15})$ (lines/m^2)	Microstrain (ε) $(x10^{-3})$
523 K@1h	(112)	26.660	360=100%	0.3764(3)	23.67(5)	1.784(7)	1.464(4)
	(220)	44.270	188=51%	0.4327(1)	25.66(1)	1.518(8)	1.350(9)
	(312)	52.436	87=24 %	0.5158(6)	25.25(3)	1.568(9)	1.373(1)
523 K@2h	(112)	26.679	605	0.37476	23.78(7)	1.768(4)	1.457(6)
	(220)	44.258	337	0.41081	27.02 (1)	1.369(5)	1.282(8)
	(312)	52.395	165	0.45127	28.83 (3)	1.202(8)	1.202(2)
573 K@2h	(112)	26.662	1119	0.38131	23.37 (7)	1.831(3)	1.483(3)
	(220)	42.235	552	0.39201	27.40(1)	1.332(1)	1.265(1)

	(312)	44.383	252	0.44915	24.77(2)	1.630(2)	1.399(5)
623 K@2h	(112)	26.653	1276	0.36059	24.71(6)	1.637(9)	1.402(8)
	(220)	44.220	642	0.38073	29.14(6)	1.177(8)	1.189(6)
	(312)	52.369	279	0.43843	29.66(4)	1.136(7)	1.168(6)

Table 2. The 2θ, d-spacing, lattice constant (a, c), tetragonal lattice distortion and unit cell volume of ~ 700 nm thin films of $CuIn_{1-x}Al_xSe_2$ obtained on annealing at 523-623 K for 1h and 2h.

Sample details	2θ (Degrees) (112) Plane	d-spacing (112) plane	2θ (Degrees) (312) Plane	d-spacing (312) plane	Lattice parameters (Å)		Tetragonal lattice distortion (c/2a)	Unit Cell Volume (Å)³
					a	c		
523 K@1h	26.661	3.3408	52.436	1.7436	5.781(5)	11.593(7)	1.336(6)	387.523(4)
523 K@2h	26.680	3.3386	52.395	1.7449	5.788)8)	11.540(3)	1.331(3)	386.711(9)
573 K@2h	26.662	3.3408	52.383	1.7452	5.789(1)	11.562(1)	1.333(1)	387.479(2)
623 K@2h	26.653	3.3419	52.369	1.7457	5.790(2)	11.568(6)	1.333(3)	387.864(6)
CIS-JCPDS (40-1487)	26.600	3.3484	52.435	1.7436	5.776(8)	11.692(3)	1.345(1)	390.182(3)

3.1.2. Impact of annealing temperature variation

Cu/In/Al/Se stack Annealing is carried out from 523 to 623 K for 2 hours(h) at each temperature. The XRD peaks intensity was found to increase with the increase in T_A (Fig. 3). The appearance of low-intense peaks viz. (101), (103), (211), and well-resolved doublet peaks (220/204) and (312/116) have already been reported, confirming the CIAS chalcopyrite phase [9]. Moreover, the crystallite size increases from 28.83(3) to 29.66(4) nm by an increase in T_A (Table 1). The tetragonal lattice distortion in CIAS films also increases with the T_A from 523 – 623 K; the value is small compared to that of CIS since 'Al' atoms are lesser than 'In' in size [9]. CIAS unit cell volume shows some increase with T_A (Table 2). Better growth in terms of crystallinity was observed at higher T_A. Further, CIAS provides higher peak intensities and larger grain sizes of (112) and (220) oriented planes, as shown in Fig. 4. These variations are attributed to the higher reactivity and thermal conductivity of 'Al.' Some reports mention an

increase in intensity as the outcome of 'Al' incorporation in CIS [7]. Thus, the present procedure for obtaining chalcopyrite from stacked elemental layers is more convenient.
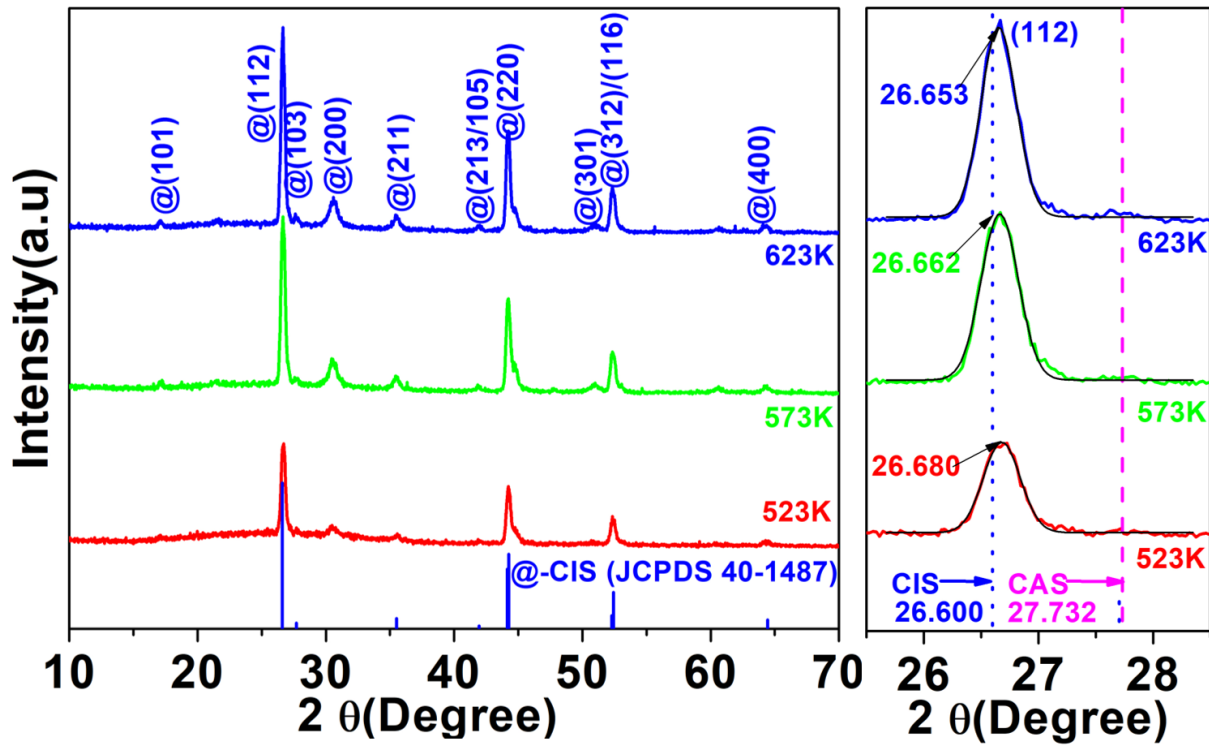
Fig. 3: The XRD plots of $CuIn_{1-x}Al_xSe_2$ thin films of 700 nm obtained on T_A of 523-623 K for 2h inside a tubular furnace at the vacuum of ~$1x10^{-3}$ mbar.

The $CuIn_{0.63}Al_{0.37}Se_2$ layers grown on annealing for 1h at 523 K show larger microstrain (ε) values. In contrast, the $CuIn_{1-x}Al_xSe_2$ layers on annealing from 523 to 623 K for 2h show larger grain size, lower microstrain (ε) and dislocation density (δ) values. As reported in the literature, the increased grain size of crystals gives lesser grain boundaries and causes a reduction in strain (ε) and dislocation density (δ) [22]. On the other hand, $CuIn_{1-x}Al_xSe_2$ films grown on annealing have ordered crystal structures when their defects and disorders are reduced. The lower strain values are due to lesser lattice imperfections in the annealed films. Thus, higher temperature and longer time annealed films show a relaxed nano-polycrystalline phase [23].
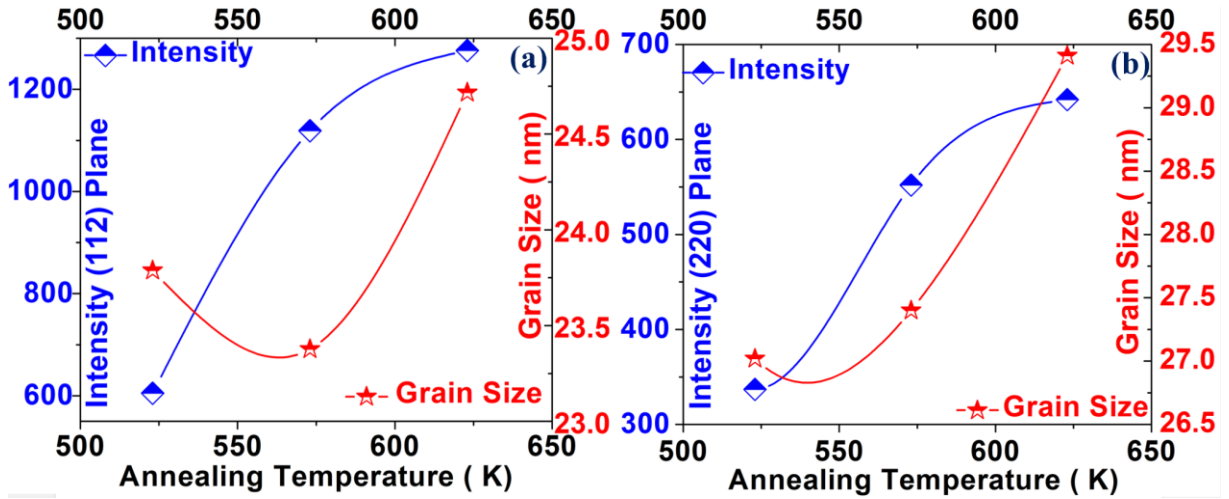
Fig. 4: The variations in peak intensity and grain size of $CuIn_{1-x}Al_xSe_2$ thin films grown on annealing under vacuum ~ 10^{-3} mbar for 2h inside a tubular furnace corresponding to (a) (112) and (b) (220) oriented planes from 523 to 623 K.

3.2. Raman Analysis

The Raman spectra for the 523 K annealed CIAS layers of 700 nm were obtained using the excitation wavelength of 532 nm (Fig. 5). The A_1, B_1, B_2, and E optical modes are Raman active, and A_2 modes are inactive in chalcopyrites. The most substantial A_1 mode is generally observed in $A^I B^{III} C_2^{VI}$ chalcopyrite compounds. The most intense line is in the range 172–186 cm^{-1}, which is of A_1 mode. The A_1 mode phonon frequency indicates a significant shift from 172 cm^{-1} (CIS phase) to 186 cm^{-1} (CAS phase) according to the increase in Al/(In+Al) content [9]. In the present case, A_1 mode was observed at 180.72(7) cm^{-1}, which is in good agreement with the CIAS phase, as already reported by others [24].
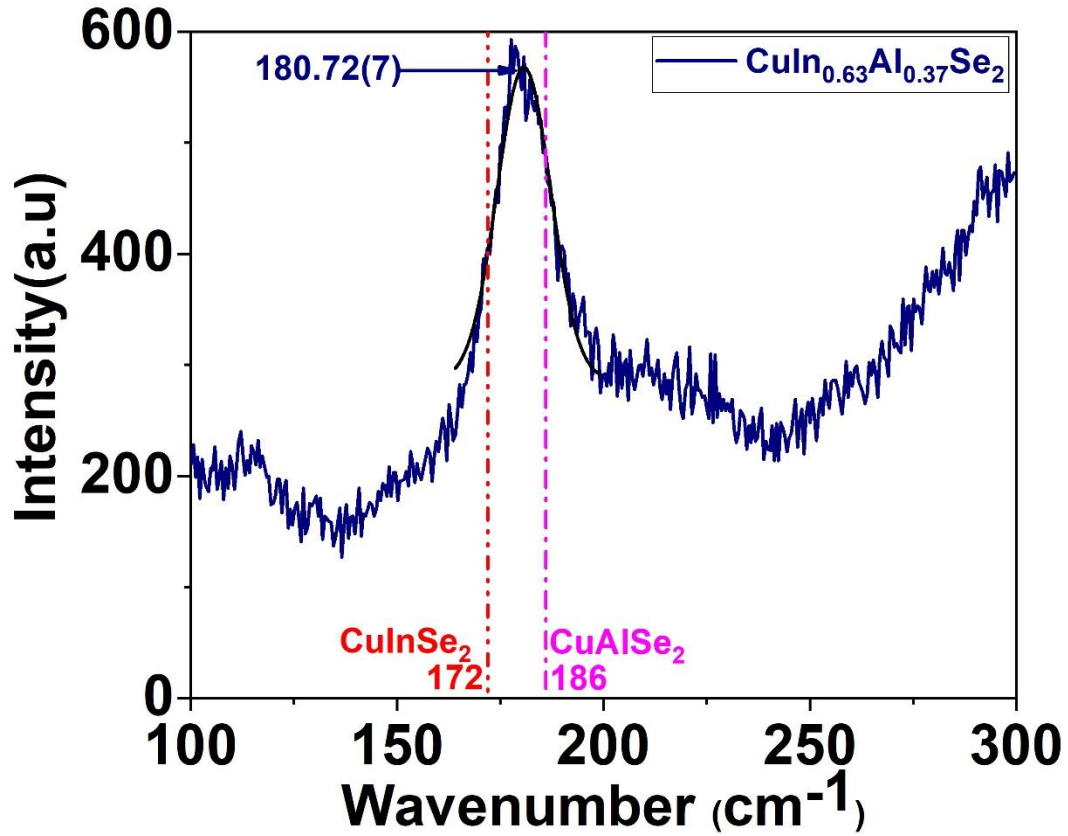
Fig. 5: The typical Raman spectra of $CuIn_{0.63}Al_{0.37}Se_2$ grown on annealing for 1h at 523 K in a vacuum coating unit (~ $1x10^{-5}$ mbar).

The prominent peak observed in 523 K for 2-hour annealed CIAS thin films was at 174.74(4) cm^{-1}, with another peak having low intensity at 215.65(6) cm^{-1}. Both peaks represented the A_1 mode of the spectra. The A_1 mode was also observed at 573 K and 673 K; the corresponding peaks were at 174.24(1) cm^{-1} and 177.36(6) cm^{-1}. In addition, the FWHM values increased with T_A (Fig. 6). Thus, the detected peak values of A_1 mode agree with the reported values of the CIAS phase.
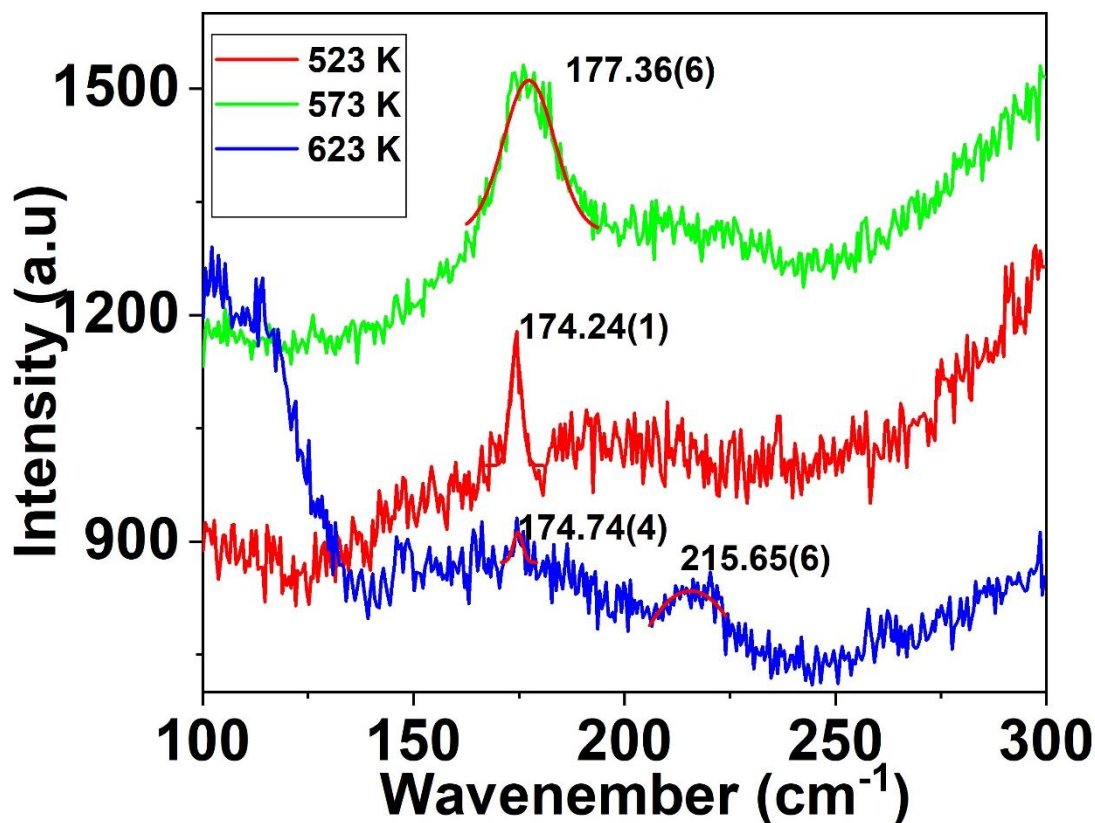
Fig. 6: The typical Raman spectra of $CuIn_{1-x}Al_xSe_2$ thin films grown on annealing under vacuum $\sim 10^{-3}$ mbar for 2h inside a tubular furnace at 523-623 K.

3.3. Morphological and Compositional Analysis

The surface morphology of the CIS and CIAS layers is determined by scanning electron microscopy (SEM). The comparative views of the 2D SEM images of CIAS and CIS crystallites obtained on annealing at 523 K for one hour (1h) in a tubular furnace are shown in Fig. 7(a)-(b). Both these layers represent particles of different sizes constituting spherical and cylindrical shapes. These films show densely packed crystallites with uniform distribution over the entire surface. The average grain length evaluated from SEM micrographs of CIS is 284.75(6) nm, whereas for CIAS, it is 413.67(4) nm. The average surface area of grains evaluated from SEM micrographs of CIS is 6.60(7) x 10^4 nm^2, whereas for CIAS, it is 2.21(7) x 10^5 nm^2. It indicates that the grains of CIAS are bigger than the CIS (Fig. 8). The larger grain size of CIAS samples is due to the high thermal conductivity of A_l, which led to a better reaction among precursors and caused coalescence. The EDAX spectra of the annealed thin films of CIAS obtained at 523 K exhibit atomic percentage ratios (Al/In+Al) and (Cu/In+Al) as 0.376, 0.877, respectively; these are shown in Fig. 9(a). The stoichiometry of CIAS thin films is $CuIn_{0.63}Al_{0.37}Se_2$, assigned based on the (Al/In+Al) ratio.
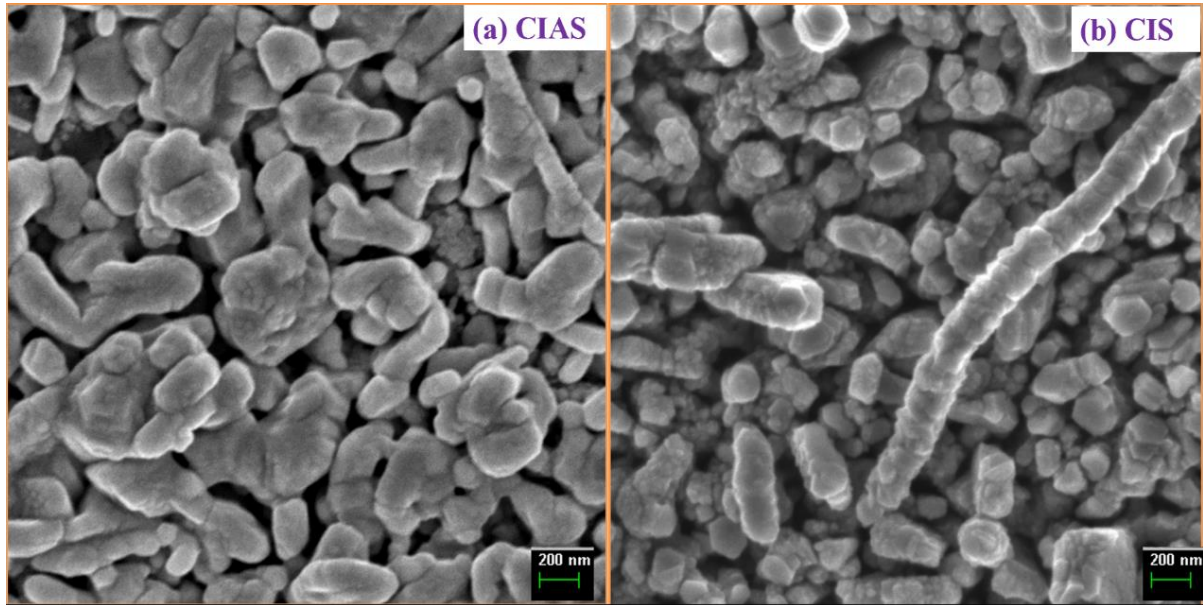
Fig. 7:   The scanning electron microscopic (SEM) images (50 K resolution) of (a)
           CuIn$_{0.63}$Al$_{0.37}$Se$_2$ and (b) CuInSe$_2$ (CIS) thin films both obtained on annealing
           at 523 K at vacuum ~ 1x10^{-5} mbar.
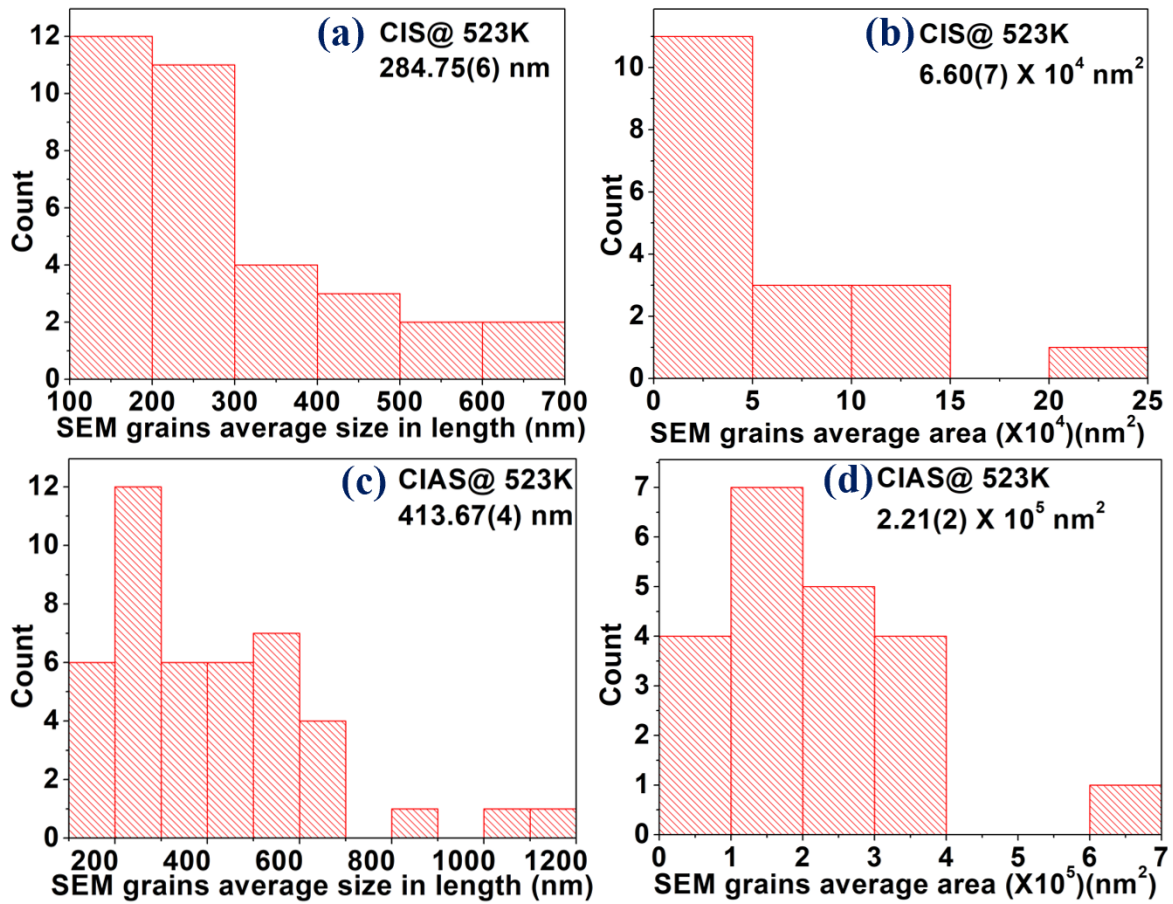
Fig. 8a-d: The SEM grains average length and average surface areas histogram plot and their
            stats for (a-b) CuInSe$_2$ (CIS) and (c-d) CuIn$_{0.63}$Al$_{0.37}$Se$_2$ thin films obtained on
            annealing at 523 K at vacuum ~ 1x10^{-5} mbar.
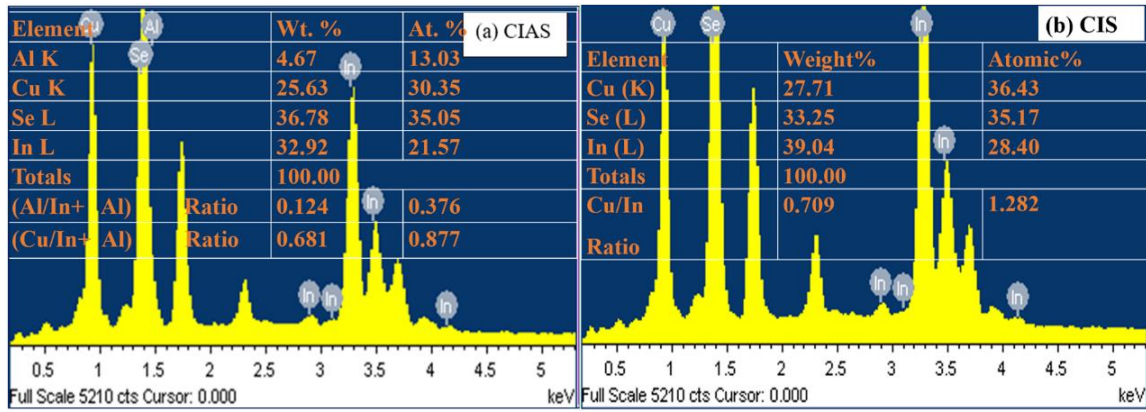
Fig. 9: Energy dispersive X-ray analysis (EDAX) spectra of (a) $CuIn_{0.63}Al_{0.37}Se_2$ and (b) $CuInSe_2$ (CIS) thin films obtained on annealing at 523 K at vacuum $\sim 10^{-5}$ mbar.

3.4. Optical Studies

The electronic transition in the energy band of the material is studied from transmission /absorption spectroscopy [25]. First, the values of the absorption coefficient (α) are determined using the transmission spectra as per the relation given in Eq. 3 [25]:

$$\alpha = \frac{1}{t} ln\left(\frac{100}{T\%}\right)$$

$$(3)$$

Where α represents an absorption coefficient, T% *is* the optical transmission percentage, and *t* is the film thickness. The optical bandgap (E_g) values are calculated from Tauc's relation given in Eq. 4 [25]

$$\alpha h\nu = A(h\nu - E_g)^n$$

$$(4)$$

where *A* is a constant, $\upsilon;$ the photon frequency, $h;$ the plank constant, $E_g;$ the optical bandgap, and *n* is a number. The allowed direct and indirect bandgap transitions in materials are determined from the values of n equals l/2 and 2, respectively. The extinction coefficient (k) determines the degree of surface uniformity. It also specifies the effectiveness of the absorption of photons of a particular wavelength in a material [26]. The extinction coefficient (k) is determined using the relation given in Eq. 5 [27]:

$$\kappa = \frac{\alpha\lambda}{4\pi}$$

$$(5)$$

where λ represents the wavelength of incident photons. Fig. 10(a) shows the transmission percentage (*T%)* versus the wavelength (λ) plot. Whereas (α), $(\alpha h\nu)^{2,}$ and (k) versus *(h\nu)* plots of CIAS thin films grown at T_A of 523 K for A_T of 1h are presented in Fig. 10(b)-(d). The optical bandgap (E_g) increases from 1.42 eV (CIS) to 1.50 eV (CIAS) due to the 'Al' replacement of 'In' in the chalcopyrite tetragonal structure [28]. Fig. 11(a) shows the T% versus λ plot of CIAS

layers grown at T_A between 523 – 623 K for 2h. Whereas their α versus $(\alpha h\nu)^2$ and ḳ versus photon energy $(h\nu)$ plots are shown in Fig. 11(b)-(d). The optical bandgap values increase from 1.35 to 1.45 eV with the increase in T_A due to an increase in the particle sizes on substitution of Al to In. This bandgap increase may occur because of modification in the crystallographic planes at higher T_A. The bandgap (E_g) increase with increasing T_A is ascribed to improved crystallinity of the $CuIn_{1-x}Al_xSe_2$ phase on annealing, i.e., the phenomenon is temperature dependent. In addition to this, the variation in direct allowed bandgap values is also affected due to a decrease in grain boundaries, crystalline imperfections, and the quantum size effect in the thin layers [29]. Several authors have also reported increased bandgap (E_g) with the increase in T_A [30-31].

The extinction coefficient (k) value increases at higher temperatures because of the stronger absorption of photons {Fig. 11(b)}. Moreover, a higher absorption coefficient $(\alpha) \sim 10^5$ cm^{-1} of CIAS was observed in this temperature range. Thus, obtained CIAS thin films suit absorber layers in solar cell fabrication.
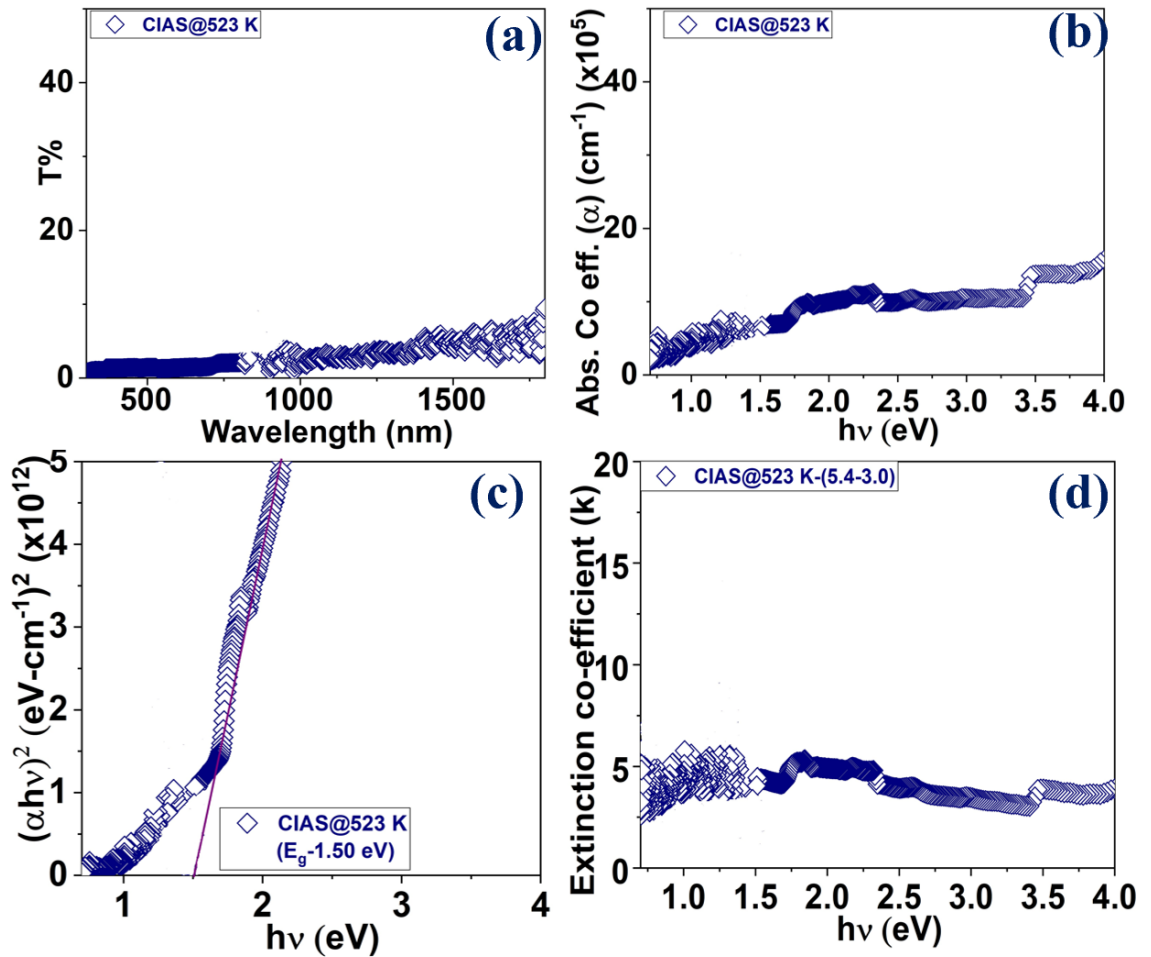
Fig. 10: (a) The transmission percentage versus wavelength (λ) plot, (b) absorption coefficient, (c) $(\alpha h\nu)^2$, and (d) κ (extinction coefficient) versus energy $(h\nu)$ plots of $CuIn_{0.63}Al_{0.37}Se_2$ (CIAS) thin films obtained on annealing at 523 K.
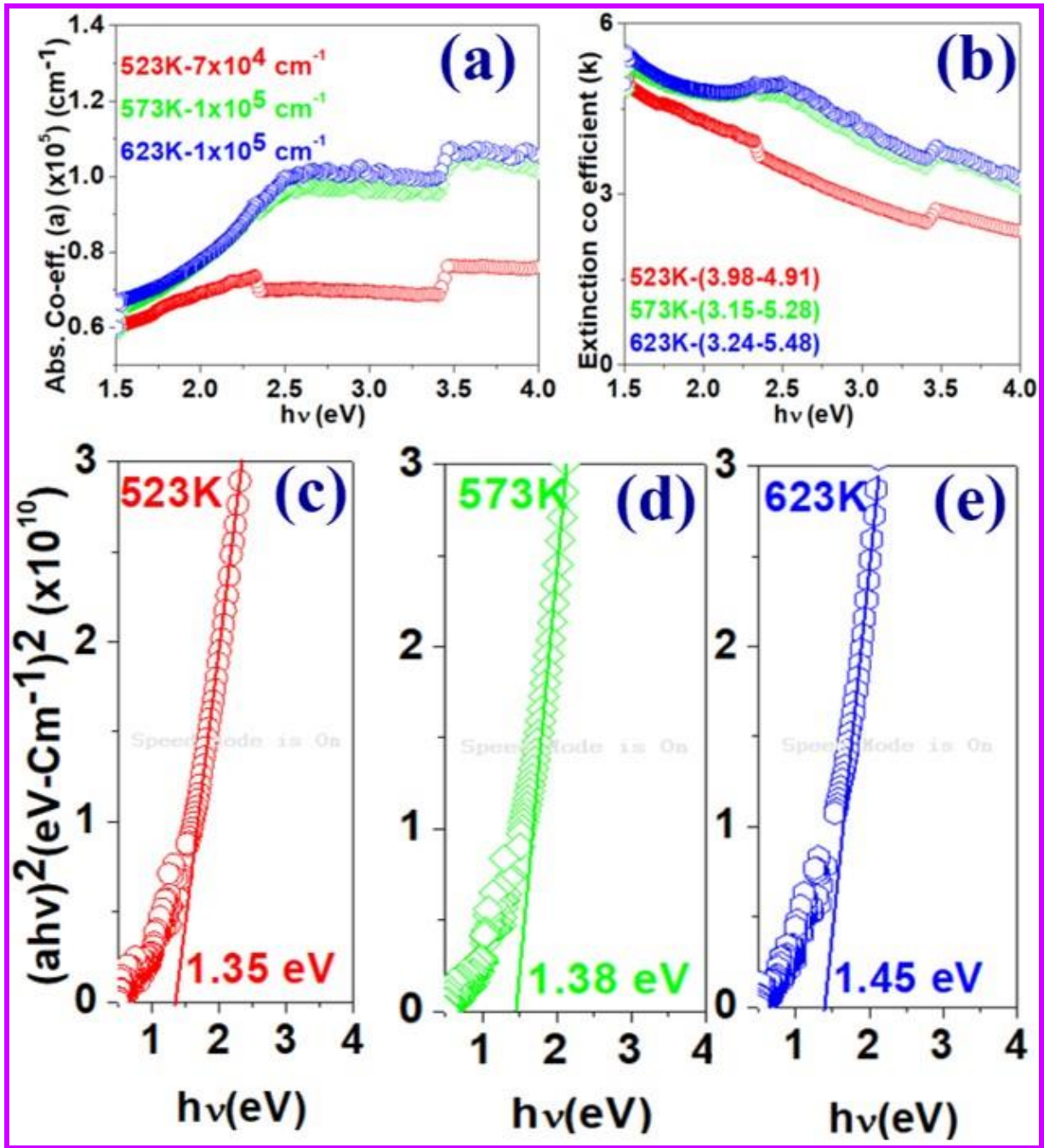
Fig. 11: (a) Absorption coefficient, (b) ƙ (extinction coefficient), and (c)-(e) $(\alpha h v)^2$ verses energy $(h v)$ plots of CuIn$_{1-x}$Al$_x$Se$_2$ (CIAS) thin films obtained on annealing for 2 h at 523- 623K.

3.5. Current transport of CIAS thin films

3.5.1. The Current-Voltage (I-V) characteristics for ohmic behaviour

The FTO/p-CIAS/Ag structure was established by depositing CIAS layers on the FTO-coated glass (substrate); these layers were grown on annealing the Cu/In/Al/Se stack from 523 to 623 K. Circular contacts of 'Ag' were formed on the top of the CIAS layer. The current-voltage (I-V) characteristics of the FTO/p-CIAS/Ag structure provide ohmic behaviour, as shown in Fig.

37

12. A rise in the slope of the I-V plots was noticed with an increase in the annealing temperatures. Therefore, the resistivity of the grown samples decreases with an increase in T_A.
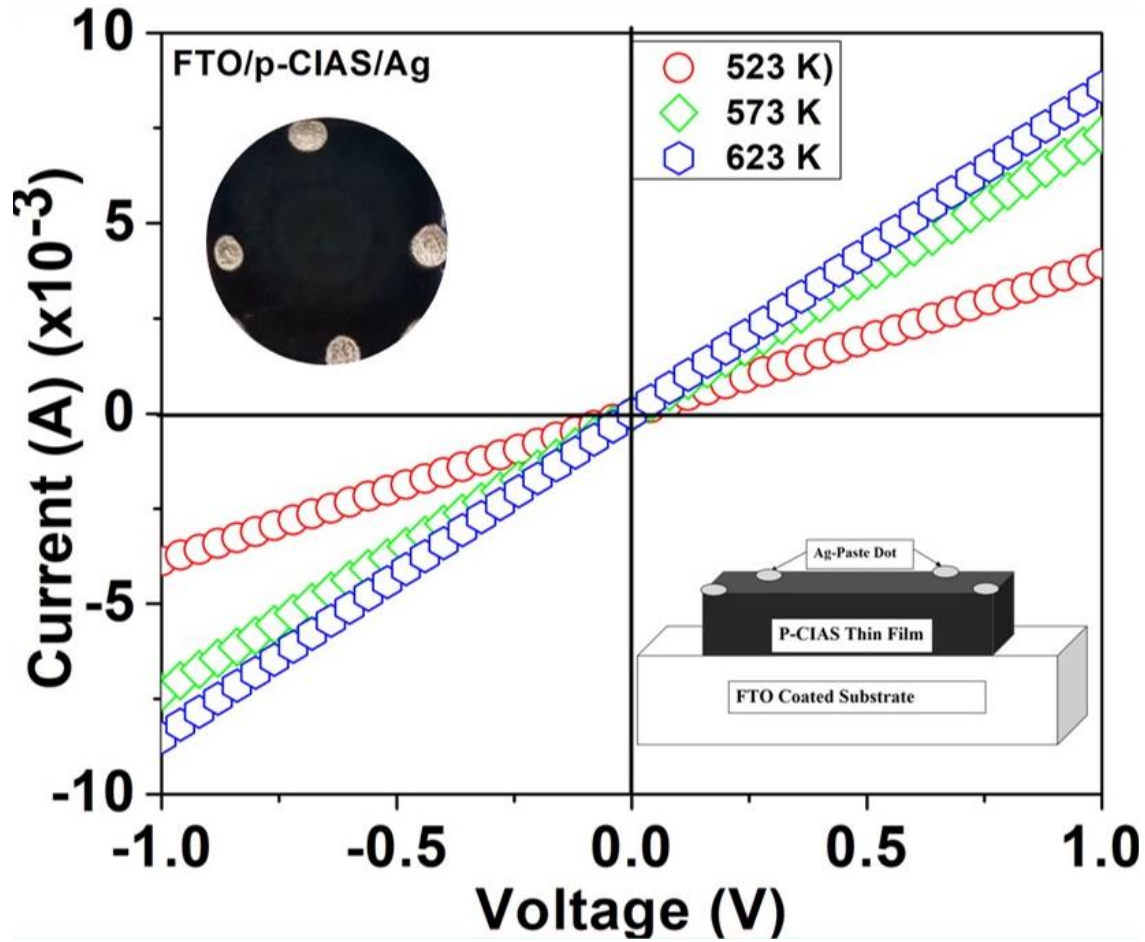
Fig. 12: The current-voltage (I-V) plots of the FTO/p-CIAS/Ag structure, having $CuAl_xIn_{1-x}Se_2$ thin films obtained on annealing at 523-623 K, exhibiting ohmic behaviour.

3.5.2. The Current-Voltage (I-V) characteristics of FTO/p-CIAS/n-CdS/In diode/photo-cell

Out of various annealing temperatures, the E_g of CIAS at 623 K {Fig. 11(e)}is closest to the optimum value of the PV cells reported in the literature [32]; thus, the p-CIAS/n-CdS/In heterojunction diodes were fabricated using CIAS thin films at 623 K. The n-CdS thin film of thickness ~ 300 nm was deposited over p-CIAS using thermal evaporation. The circular contacts were subsequently formed at the top of n-CdS using a physical mask of a diameter of 1.0 mm. The forward-reverse semi-log current-voltage (I-V) characteristics of heterojunction diodes exhibit rectifying behaviour, as shown in Fig. 13. The high voltage conduction at forward bias is due to an unintentional oxide layer formed during PN junction formation. The zero-bias barrier height (ϕ_{bo}), calculated from the non-linear fitting of the I-V curve, is 0.50(5) eV (Fig. 13).
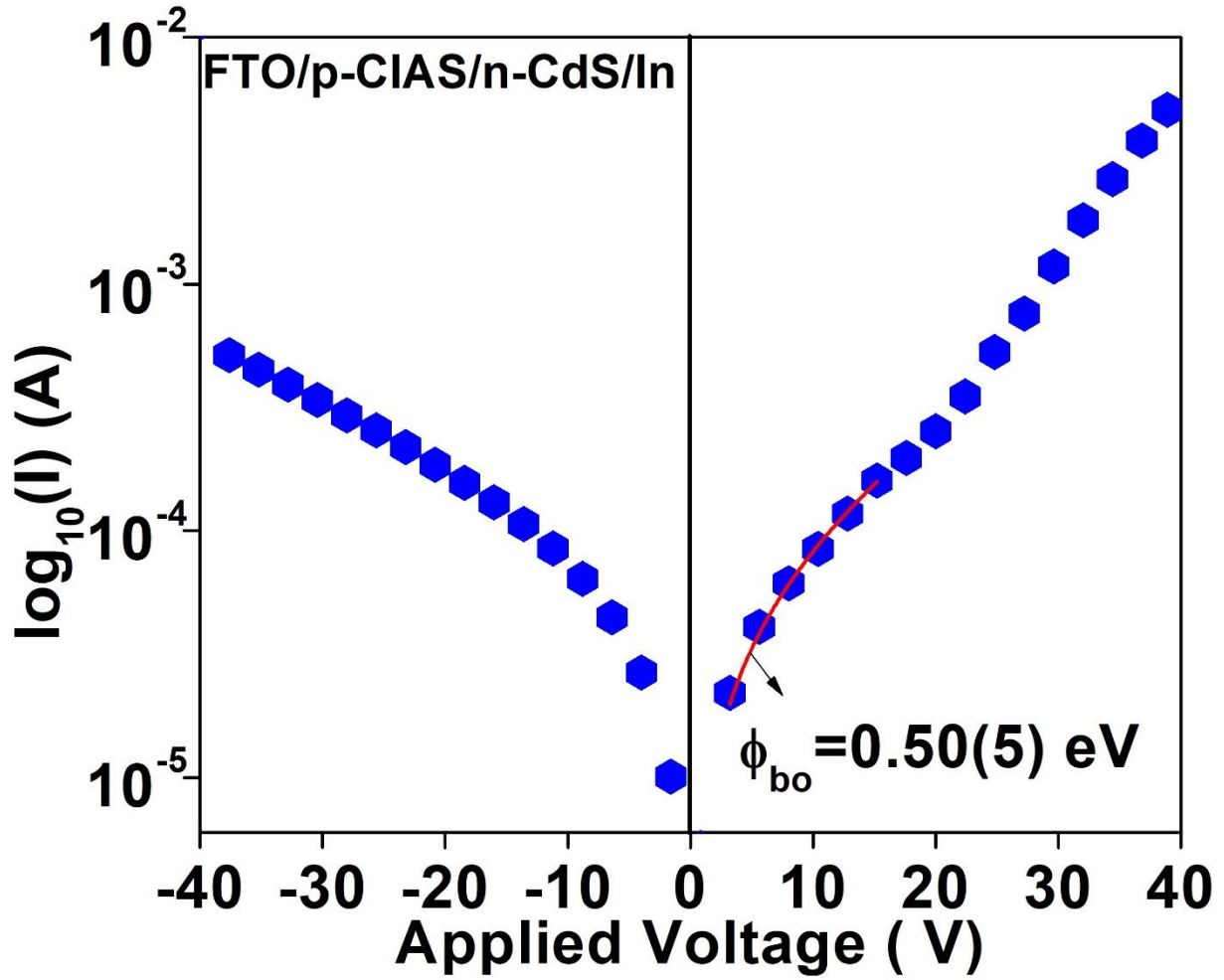
Fig. 13: Semi-logarithmic forward and reverse current-voltage (I-V) characteristics of the FTO/p-CIAS/n-CdS/In heterojunction diode formed on the p-CuAl$_x$In$_{1-x}$Se$_2$ thin films obtained on annealing at 623 K and non-linear fitting of forward l-V plots as fitted with I-V equation of the diode.

The 700 nm layers of p-CIAS grown over FTO-coated glass were also used as an absorber layer to fabricate photocell structure using a CdS (~300 nm) window layer and 'In' metal fingers as the top electrode. The cell area was kept at ~ 1 cm^2. The open-circuit voltage (*V$_{oc}$*) of the FTO/p-CIAS/n-CdS/In device under illumination was observed to be 2.5 mV (Fig. 14). The low barrier height (*ϕ$_{bo}$*), and open-circuit voltage (V$_{oc}$) is due to presence of oxide layer traps at the interface, which restricts the movement of flow of photons to the PN-junction, and flow of charge carriers from it (junction).
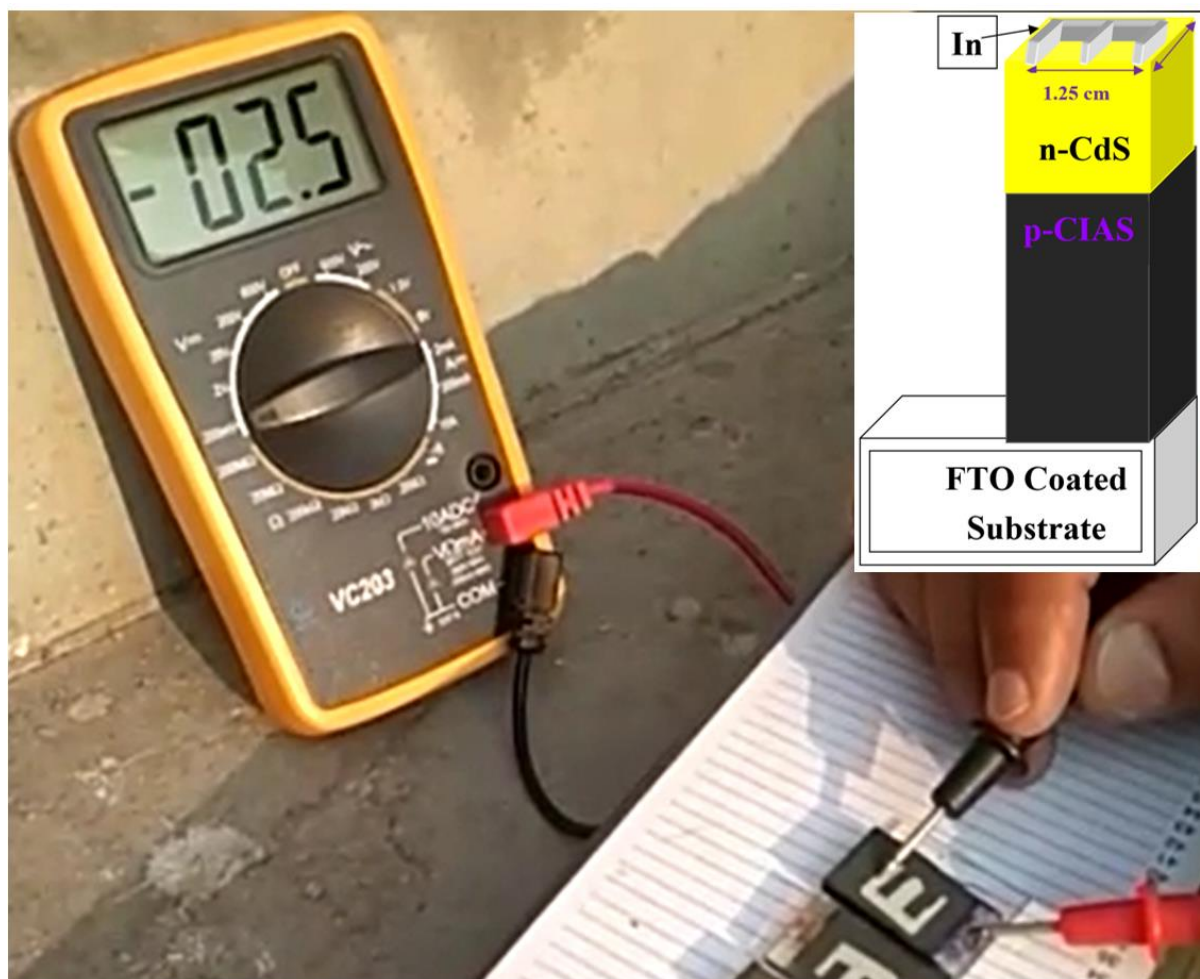
Fig.14: The open circuit voltage (V_{oc}) of the fabricated heterojunction FTO/p-CIAS/ n-CdS/In photovoltaic cell formed using the p- $CuAl_xIn_{1-x}Se_2$ thin films grown on annealing at 623 K.

4. Conclusion

Thin layers of $CuIn_{0.63}Al_{0.37}Se_2$ are grown on annealing at 523 K using a low-cost sequentially evaporated layer deposition (SELD) method. The single chalcopyrite phase of CIAS was observed from 523 to 623 K. The CIAS phase was confirmed from the A_1 mode of Raman Spectra. The films exhibited a high absorption coefficient (α) and demonstrated bandgap (E_g) tuning. There is an improvement in the crystallinity of the CIAS phase at higher annealing temperatures; the phenomenon is attributed to the increased bandgap. Thus, the grown CIAS layers can be used as absorber layers in solar cell structures. Furthermore, the FTO/p-CIAS/n-CdS/In heterojunction photocell provides an open-circuit voltage (V_{oc}) of 2.5 mV. Thus, the developed CIAS films demonstrate a photovoltaic response.

References:

[1] MA Green, E.D. Dunlop, J. Hohl-Ebinger, M. Yoshita, N. Kopidakis, X. Hao, Solar cell efficiency tables (Version 58), Prog. Photovoltaics Res. Appl. 29 (2021) 657–667. https://doi.org/10.1002/pip.3444.

[2] P.D. Paulson, M.W. Haimbodi, S. Marsillac, R.W. Birkmire, W.N. Shafarman, $CuIn_{1-x}Al_xSe_2$ thin films and solar cells, J. Appl. Phys. 91 (2002) 10153–10156. https://doi.org/10.1063/1.1476966.

[3] M.A. Contreras, K. Ramanathan, J. Abushama, F. Hasoon, D.L. Young, B. Egaas, R. Noufi, Diode characteristics in state-of-the-art ZnO/CdS/ $Cu(In_{1-x}Ga_x)Se_2$ solar cells, Prog. Photovoltaics Res. Appl. 13 (2005) 209–216. https://doi.org/10.1002/pip.626.

[4] T. Hayashi, T. Minemoto, G. Zoppi, I. Forbes, K. Tanaka, S. Yamada, T. Araki, H. Takakura, Effect of composition gradient in $Cu(In,Al)Se_2$ solar cells, Sol. Energy Mater. Sol. Cells. 93 (2009) 922–925. https://doi.org/10.1016/j.solmat.2008.11.007.

[5] F. Itoh, O. Saitoh, M. Kita, H. Nagamori, H. Oike, Growth and characterisation of $Cu(InAl)Se_2$ by vacuum evaporation, Sol. Energy Mater. Sol. Cells. 50 (1998) 119–125. https://doi.org/10.1016/S0927-0248(97)00132-3.

[6] G. Hema Chandra, C. Udayakumar, S. Rajagopalan, A.K. Balamurugan, S. Uthanna, Influence of substrate temperature on structural, electrical and optical properties of flash evaporated $CuIn_{0.60}Al_{0.40}Se_2$ thin films, Phys. Status Solidi Appl. Mater. Sci. 206 (2009) 704–710. https://doi.org/10.1002/pssa.200925010.

[7] Y. Bharath Kumar Reddy, V. Sundara Raja, Preparation and characterisation of $CuIn_{0.75}Al_{0.25}Se_2$ thin films by co-evaporation, Phys. B Condens. Matter. 381 (2006) 76–81. https://doi.org/10.1016/j.physb.2005.12.256.

[8] J. Zhang, H. Deng, J. He, X. Meng, T. Liu, L. Sun, P. Yang, J. Chu, Structural and electrical properties of $CuIn_{1-x}Al_xSe_2$ thin films prepared by radio-frequency magnetron sputtering process, Appl. Surf. Sci. 326 (2015) 211–215. https://doi.org/10.1016/j.apsusc.2014.11.131.

[9] J. Olejníček, C.A. Kamler, S.A. Darveau, C.L. Exstrom, L.E. Slaymaker, A.R. Vandeventer, N.J. Ianno, R.J. Soukup, Formation of $CuIn_{1-x}Al_xSe_2$ thin films studied by Raman scattering, Thin Solid Films. 519 (2011) 5329–5334. https://doi.org/10.1016/j.tsf.2011.02.030.

[10] M. Nishitani, T. Negami, M. Terauchi, T. Hirao, Preparation and characterisation of $CuInSe_2$ thin films by Molecular-Beam Deposition Method, Jpn. j. Appl. Phys. 31 (1992) 192–196. https://doi.org/10.1143/JJAP.31.192.

[11] B. Kavitha, M. Dhanam, Raman, photoluminescence analysis on $Cu(InAl)Se_2$ thin films and the fabrication of $Cu(InAl)Se_2$ based thin film solar cells, J. Mater. Sci. Mater. Electron. 25

(2014) 4404–4411. https://doi.org/10.1007/s10854-014-2180-z.

[12] S. Marsillac, P.D. Paulson, M.W. Haimbodi, R.W. Birkmire, W.N. Shafarman, High-efficiency solar cells based on Cu(InAl)Se$_2$ thin films, Appl. Phys. Lett. 81(2002) 1350–1352. https://doi.org/10.1063/1.1499990.

[13] Muhammad Aamir Hassan, Spray pyrolysis synthesised Cu(In,Al)(S,Se)$_2$ thin films solar cells, Mater. Res. Express. 5 (2018) 1–31. https://doi.org/10.1088/2053-1591/aab116.

[14] C.R. Dhas, A.J. Christy, R. Venkatesh, E.S.M. S., SK Panda, B. Subramanian, K. Ravichandran, P. Sudhagar, A.M.E. Raj, Low-cost and eco-friendly nebuliser spray coated CuInAlS$_2$ counter electrode for dye-sensitised solar cells, Elsevier BV, **2018**. https://doi.org/10.1016/j.physb.2018.01.042.

[15] Y. Ganjkhanlou, V. Crocellà, M. Kazemzad, G. Berlier, T. Ebadzadeh, I. Safaee, A. Kolahi, A. Maghsoudipour, Hydrothermal–electrochemical deposition of semiconductor thin films: the case of CuIn(Al)Se$_2$ compound, J. Mater. Sci. Mater. Electron. 28 (2017) 15596–15604. https://doi.org/10.1007/s10854-017-7446-9.

[16] K.H. Kim, Fianti, Growth of single-phase CuInAlSe$_2$ thin films by using pulsed laser deposition and selenization, J. Korean Phys. Soc. 60 (2012) 2001–2006. https://doi.org/10.3938/jkps.60.2001.

[17] R. Niranjan, A. Banotra, N. Padha, Development of CuInSe$_2$ thin films by SELD method for photovoltaic absorber layer application, J. Mater. Sci. Mater. Electron. 31 (2020) 3172–3183. https://doi.org/10.1007/s10854-020-02865-2.

[18] D. Dwyer, I. Repins, H. Efstathiadis, P. Haldar, Selenization of co-sputtered CuInAl precursor films, Sol. Energy Mater. Sol. Cells. 94 (2010) 598–605. https://doi.org/10.1016/j.solmat.2009.12.005.

[19] H. Cao, H. Deng, J. Tao, W. Zhou, X. Meng, L. Sun, P. Yang, J. Chu, Microstructural and morphological properties of sputtered Cu(In, Al)Se$_2$ thin films for solar cell applications, Mater. Lett. 157 (2015) 42–44. https://doi.org/10.1016/j.matlet.2015.05.021.

[20] BD. Cuilty and S.R. Stock, Elements of X-Ray Diffraction, Third, Pearson New Internation Edition, 2014.

[21] J.C. Slater , Atomic Radii in Crystals, J. Chem. Phys. 41 (1964) 3199-3204. http://dx.doi.org/10.1063/1.1725697

[22] G. K. Williamson, R. E. Smallman, III. Dislocation densities in some annealed and cold-worked metals from measurements on the X-ray Debye-Scherrer spectrum, Philos. Mag. 1 (1956) 34–46. https://doi.org/10.1080/14786435608238074

[23] S. Kumar, A. Banotra, N. Padha, S. Ahmed, Effect of substrate and annealing temperature on the physical properties of the thin films of $SnSe_2$-SnSe alloy, Optical Materials 134 (2022) 113078. https://doi.org/10.1016/j.optmat.2022.113078

[24] F.W. Ohrendorf, H. Haeuseler, Lattice dynamics of chalcopyrite type compounds. Part III. Rigid ion model calculations, Cryst. Res. Technol. 34 (1999) 363–378. https://doi.org/10.1002/(SICI)1521-4079(199903)34:3<363::AID-CRAT363>3.0.CO;2-Q.

[25] J. Tauc, Optical Properties and Electronic Structure of Amorphous Germanium BY, Phys. Stat. Sol. 15 (1966) 627–637. https://doi.org/10.1002/pssb.19660150224.

[26] R. Niranjan, N. Padha, Growth of γ- In_2Se_3 monolayer from multifaceted In_xSe_y thin films via annealing and study of its physical properties, Mater. Chem. Phys. 257 (2021) 123823. https://doi.org/10.1016/j.matchemphys.2020.123823.

[27] W.Q. Hong, Extraction of extinction coefficient of weak absorbing thin films from special absorption, J. Phys. D: Appl. Phys. 22(9) (1989) 1384-1385. https://doi.org/ 10.1088/0022-3727/22/9/024

[28] U. Parihar, K. Sreenivas, J.R. Ray, C.J. Panchal, N. Padha, B. Rehani, Influence of substrate temperature on structural, optical, and electrical properties of flash evaporated $CuIn_{0.81}Al_{0.19}Se_2$ thin films, Mater. Chem. Phys. 139 (2013) 270–275. https://doi.org/10.1016/j.matchemphys.2013.01.034.

[29] R. Jayakrishnan, V. Ganeshan, On the multi-channel conduction in β-In_2S_3 thin films. Mater Sci Semicond Process 24 (2014) 220-4. https://doi.org/10.1016/j.mssp.2014.03.031

[30] A. S. Pugalenthi et al., Effect of post-deposition annealing on the structure, morphology, optical and electrical properties of $CuInGaSe_2$ thin films, Opt. Mater. (Amst). 62 (2016) 132–138. https://doi.org/10.1016/j.optmat.2016.09.045.

[31] P.U. Londhe, A. B. Rohom, N. B. Chaure, Solar cell studies on $CuIn_{1-x}Ga_xSe_2$ nanoparticles derived from chemical reduction process, Solar Energy 206 (2020) 18–26. https://doi.org/10.1016/j.solener.2020.05.096

[32] T. Zdanowicza, T. Rodziewiczb, M. Zabkowska-Waclawek, Theoretical Analysis of the Optimum Energy Band Gap of Semiconductors for Fabrication of Solar Cells for Applications in Higher Latitudes Locations, Sol. Energy Mater Sol. Cells 87 (2005) 757–769. https://doi.org/10.1016/j.solmat.2004.07.049

iii. **Has the progress been according to the original plan of work and towards achieving the objective, if not, state the reasons.**

Yes, the progress has been in accordance with the original plan of work and all objectives were met.

iv. **Please indicate the difficulties, if any, experienced in implementing the project.**
No, difficulty was faced while pursuing the project.

v. **If project has not been completed, please indicate the approximate time by which it is likely to be completed. A summary of the work done for the period (Annual basis) may please be sent to the Commission on a separate sheet.**

The project was completed in the specified tenure of three years, however, the publication of some of the papers took more time.

vi. **If the project has been completed, please enclose a summary of the findings of the study. One bound copy of the final report of work done may also be sent to the University Grants Commission.**

The study of selenium thin films indicated that nanocrystalline Se alone is highly useful as an absorber layer in the solar cell structure. The optimization of Se-based thin films in terms of their thickness and annealing temperature was performed and finally, these were used as an absorber layer in the formation of FTO/ p-Se/n- CdS/In photovoltaic cell. Their heterojunction was also studied. The research paper of this study has been published.

It was observed that the Se when combined with Cu (I) and In (III) provides a tetragonal CIS phase. The CIS phase provides a high absorption coefficient and tunable bandgap that touches the visible-NIR region of the spectrum. Furthermore, these films show low electrical resistivity, high mobility, and high carrier concentration. The grown CIS layer of two different thickness values was processed at different annealing temperatures. The results were published as a research paper.

It is also observed that when Se combines with In exhibits high transmission, bandgap tuning, and high absorption coefficient values. It also shows changes in the electrical parameters on annealing due to changes in composition and phase. This combination shows the γ-In$_2$Se$_3$ phase which is suitable as a buffer layer in solar cell structure. The results were published as a research paper.

The partial substitution of aluminum (Al) with Indium (In) in the CIS structure provides a CuIn$_{1-x}$Al$_x$Se$_2$ phase, here the bandgap varies from 1.35 -1.45 eV which is a wavelength that provides maximum photovoltaic efficiency. Further FTO/p-CIAS/n-CdS/In pn heterojunction diodes have been fabricated and their I-V analysis shows rectifying behaviour. A photovoltaic cell of this configuration was tested which provided V$_{oc}$ and confirmed the photovoltaic response of the heterojunction diode. A research paper based on these results has been communicated.

The analyses of undertaken chalcopyrites have created a scope for further investigations on $CuIn_{1-x}Al_xSe_2$ semiconducting materials. The characterizations of alloy/compound materials provided a successful methodology for fabricating photovoltaic solar cells with high efficiency, stability, and fill factor.

vii. Any other information which would help in the evaluation of work done on the project. At the completion of the project, the first report should indicate the output, such as (a) Manpower trained (b) Ph. D. awarded (c) Publication of results (d) other impacts, if any

(a) Manpower trained:

Five students were trained in the following trades:

(i)   Growth of nano-sized thin films and multilayered deposition/growth for the fabrication of devices.

(ii)   Study of the characteristics of semiconductor materials and thin films

(iii)   Testing of the pn-junction diodes and photovoltaic cells

(iv)   Handling of the semiconductor thin layers under high vacuum.

(v)   Thermal evaporation and annealing techniques, contact formations, and current-voltage (I-V)/ capacitance-voltage (C-V) measurements.

(vi)   Development of Metal-semiconductor Schottky barrier diodes and pn-heterojunction diodes and pn-photocells.

The single-phase $CuIn_{1-x}Al_xSe_2$ (CIAS) thin films have been successfully grown through annealing of the stack of precursors obtained by the sequentially evaporated layer deposition (SELD) method. Further, that FTO/p-CIS/n-CdS/In heterojunction diodes have been fabricated, and their photovoltaic cell response was tested successfully.

(b) PhD Awarded:

S. No	Name of Programme	Candidate's Name	Title of the PhD thesis supervised	Notification No. & Date
1	PhD in Physics University of Jammu	Mr Arun Banotra	Preparation and characterization of Sn(S, Se) semiconducting thin films and diodes for solar cell application	No. Eval. -Prof-I/18/5234-5335 Dated 28-09-2018
2	PhD in Electronics University of Jammu	Ms Anjali Verma	Fabrication and Characterization of Sn, Se & Te-based Polycrystalline Compound Semiconductor Thin Films and Devices	No. Eval.-Prof-I/20/1577-1626 Dated 31-07-2020

3	PhD in Physics University of Jammu	Mr Rajesh Niranjan (Year 2022)	Study of some chalcopyrite compound semiconductor materials and thin films for electronic device applications	No. Eval. -Prof-I/22/7349-7400 Dated 11-11-2022
4	PhD in Physics University of Jammu	Mr Shammi Kumar (Year 2023)	Study of some chalcogenide based thin films and junction barriers for photovoltaic and optoelectronic device applications	No. Eval. -Prof-I/22/5657-5755 Dated 08-09-2023
5	PhD in Physics University of Jammu	Mr Shafiq Ahmed (Year 2023)	Study of thin films of some chalcopyrite materials and formations of diodes for photovoltaic applications	Thesis Submitted

(c) **Publication of results:**

S. No	Date	Title of the Paper	Name of journal/ Impact Factor	Whether Refereed or not
1	Sep 2023 (Vol 13)	Processing of nanocrystalline thin films of selenium and formation of FTO/ p-Se/n-CdS/In heterojunctions for photovoltaic response doi.org/10.1016/j.rio.2023.100533	*Results in Optics* *Science Direct (ELSEVIER SCIENCE)* Impact Factor 2.12 *Cite Score 1.8*	Referred
2	Dec 2022 (Vol 135)	Effect of substrate and annealing temperature on the physical properties of the thin films of $SnSe_2$-SnSe alloy doi.org/10.1016/j.optmat.2022.113078	*Optical Materials* *Science Direct (ELSEVIER SCIENCE) Impact Factor 3.754 Cite Score 5.2*	Referred
3	Sep 2022	Impact of annealing on the growth dynamics of indium sulphide buffer layers doi.org/10.1016/j.jmrt.2022.09.094	Journal of Materials Research and Technology *Science Direct (ELSEVIER SCIENCE)* Impact Factor 6.267	Referred
4	Aug 2022	Sequentially evaporated layer deposition stack of Cu_xS thin films for photonics applications doi.org/10.1016/j.jmrt.2022.08.097	Journal of Materials Research and Technology *Science Direct (ELSEVIER SCIENCE)* Impact Factor 6.267	Referred
5	Jnne 2022	Growth Dynamics of SnSe Thin Films on Annealing of Precursor Layers Stacked by Multisource Sequential Elemental LayerDeposition doi.org/10.1080/10584587.2022.2102805	Integrated Ferroelectrics (Taylor & Francis Publication) Impact Factor 0.836	Referred
6	May 2022	Organic coordinated SnS and $SnS_{1-x}Se_x$ crystals:	Optical and quantum Electronics,	Referred

		synthesis, characteristics and optical behaviour for photonic applications doi.org/10.1007/s11082-022-03739-z	Springer Link Impact Factor 2.89	
7	October 2021	A two-step method to obtain the 2D layers of SnSe2 single phase and study its physical characteristics for photovoltaic and photo-converter devices doi.org/10.1007/s00339-021-04992-x	Applied Physics A Materials Science and Processing Springer Link Impact Factor 2.584	Referred
8	September 2021	MSELD SnS1-xSex alloy thin films towards efficient structural and bandgap engineering for photonic devices doi.org/10.1557/s43578-021-00394-0	Journal of Material Research (Springer Link) Impact Factor 2.95	Referred
9	October 2020	SnxSy MSELD stack thin films: Processing, characteristics and devices for photonic applications doi.org/10.1016/j.solener.2020.10.005	Solar Energy Science Direct (ELSEVIER) Impact Factor 5.742	Referred
10	October 2020	Effect of CuIn1-xAlxSe2 (CIAS) thin film thickness and diode annealing temperature on Al/p-CIAS Schottky diode doi.org/10.1007/s12034-020-02245-w	*Bulletin of Materials Science* Science Direct (Springer Link) Impact Factor 1.783	Referred
11	September 2021	Growth of γ- In2Se3 monolayer from multifaceted InxSey thin films via annealing and study of its physical properties doi.org/10.1016/j.matchemphys.2020.123823	Materials Chemistry and Physics Science Direct (Elsevier Science) Impact Factor 3.408	Referred
12	January 2020	Development of CuInSe2 thin films by SELD method for photovoltaic absorber layer application doi.org/10.1007/s10854-020-02865-2	Journal of Materials Science: Materials in Electronics (Springer Nature) Impact Factor 2.478	Referred
13	January 2020	Development of SnS nanocrystals and tuning of parameters for use as spectral selective photoabsorbers doi.org/10.1016/j.jcrysgro.2019.125460	Journal of Crystal Growth Science Direct (Elsevier Science) Impact Factor 1.573	Referred
14	December 2019	Facile growth of SnS and $SnS_{0.40}Se_{0.60}$ thin films as an absorber layer in the solar cell structure doi.org/10.1016/j.matpr.2019.11.154	Materials Today: Proceedings Growth Science Direct (Elsevier Science)	Referred
15	April 2019	SnTexSe1-x alloy: An effective	Journal of Electronic	Refereed

			Materials (Springer) Impact Factor 1.676	
		alternate to SnSe nanocrystalline thin films for optoelectronic applications doi.org/10.1007/s11664-019-07202-w		
16	October 2019	Development of $SnS_{0.4}Se_{0.6}$ Ternary Alloy on Annealing of Thermally Deposited Films doi.org/10.1007/s11664-018-6710-y	Journal of Electronic Materials (Springer) Impact Factor 1.676	Refereed
17	May 2018	Impact of additional sulphur on structure, morphology and optical properties of SnS thin films by thermal evaporation doi.org/10.1063/1.5032986	AIP Conference Proceedings	Refereed
18	April 2018	Structural and optical properties of tin disulphide thin films grown by flash evaporation doi.org/10.1063/1.5028884	AIP Conference Proceedings	Refereed
19	November 2017	Effect of substrate temperature on the characteristics of mixed phase $SnTe_xSe_{1-x}$ (x = 0.32) thin films doi.org/10.1088/2053-1591/aa98b0	Mater. Res. Express (IOP Science) Impact Factor 1.618	Refereed
20	November 2017	Effect of annealing on physical characteristics of the vacuum evaporated mixed phase Sn_xS_y thin films doi.org/10.1088/2053-1591/aa982e	Mater. Res. Express (IOP Science) Impact Factor 1.618	Refereed
21	May 2016	Influence of temperature on Al/p-CuInAlSe2 thin-film Schottky diodes Doi.org/10.1007/s00339-016-0105-9	Applied Physics A Materials Science and Processing (Springer) Impact Factor 2.584	Refereed
22	Sep 2023 Vol 61 pp. 739-743	A Two-step Method to Grow ZnSe Thin Films and To Study their Characteristics doi.org/10.56042/ijpap.v61i9.3209	Indian Journal of Pure & Applied Physics Vol. 61, September 2023, pp. 739-743	Referred

(d) Other Impacts:

A vacuum tube sealing unit was sanctioned under this project which has become an asset for future research of the university in this emerging area of noble semiconductor materials.
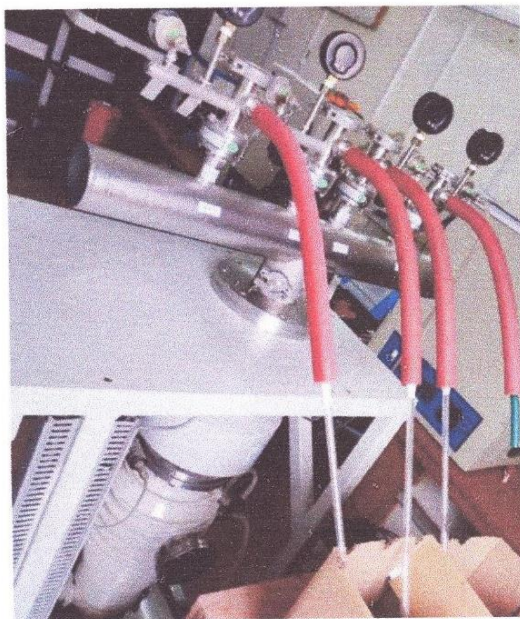
Vacuum Tube Sealing Setup

SIGNATURE OF THE PRINCIPAL INVESTIGATOR

REGISTRAR/PRINCIPAL
REGISTRAR
University of Jammu
Jammu.

UNIVERSITY GRANTS COMMISSION
BAHADUR SHAH ZAFAR MARG
NEW DELHI – 110 002

PROFORMA FOR SUBMISSION OF INFORMATION AT THE TIME OF SENDING THE FINAL REPORT OF THE WORK DONE ON THE PROJECT

1. Title of the Project: $Cu(In_{1-x}Al_x)Se_2$ Thin Films optimization, Device Fabrication and their use in Photovoltaic Applications.

2. NAME AND ADDRESS OF THE PRINCIPAL INVESTIGATOR:
    Name: Prof. Naresh Padha
    Office: Solid State Electronics Lab., Department of Physics and Electronics, University of Jammu, Jammu-180006.
    Resi: H. No. 723, Sector E, Sainik Colony, Jammu-180011, Jammu Kashmir, INDIA.

3. NAME AND ADDRESS OF THE INSTITUTION: University of Jammu,
    Baba Saheb Ambedkar road
    Jammu-180006, J&K UT

4. UGC APPROVAL LETTER NO. AND DATE: F.No. -43-398/2014(SR)
    Dated: 18th September, 2015
5. DATE OF IMPLEMENTATION: 02-12-2015

6. TENURE OF THE PROJECT: Three (03) Years

7. TOTAL GRANT ALLOCATED: Rs 13,55,000/-

8. TOTAL GRANT RECEIVED: Rs 11,13,726/-

9. FINAL EXPENDITURE: Rs 10,98,825/-

10. TITLE OF THE PROJECT: $Cu(In_{1-x}Al_x)Se_2$ Thin Films Optimization, Device Fabrication and their use in Photovoltaic Applications.
11. OBJECTIVES OF THE PROJECT:
i) The exploration of new material compositions, their constituent ratio, processing skills and device geometry to recommend future strategies for Schottky barrier and pn-heterojunction device applications. (Identification of metals which show ideal ohmic as well as Schottky contacts on to CIAS semiconductor, which can be possible by detailed analysis of barrier properties).
ii) The identification and control of defects or dislocations as well as strains which influence the electrical and/or optical properties of the films. Efforts shall be made to improve the quality of deposited films by optimizing processes and conditions for deposition.
iii) Given that devices of $CuIn_{1-x}Al_xSe_2$ are good candidates for space solar cells and other related optoelectronic applications. Attempts shall also be made to realize the Schottky barrier as well as heterojunction diodes by tailoring their bandgaps and analysing their temperature dependence response.
iv) The optimization of CIAS solar cells in terms of their absorption coefficient, fill–factor and efficiency will be undertaken to have better quality CIAS solar cells.

12. WHETHER OBJECTIVES WERE ACHIEVED: YES

13. ACHIEVEMENTS FROM THE PROJECT:

The single-phase $CuIn_{1-x}Al_xSe_2$ (CIAS) thin films have been successfully grown through annealing of the stack of precursors obtained by the sequentially evaporated layer deposition (SELD) method. Further, that FTO/p-CIS/n-CdS/In heterojunction diodes have been fabricated, and their photovoltaic cell response was tested successfully.

The students were trained in the area of thin film fabrication, optimization and development of multiple-layered devices for photovoltaic response. Five research students have used the resources of the projects and Four were successfully awarded their doctorate degrees. Five high-quality publications have been achieved in the research domain during the intervening period. Moreover, 17 other high-standard publications were achieved using the resources of the projects.

14. SUMMARY OF THE FINDINGS:

The present project focused on the development of $Cu(In_{1-x}Al_x)Se_2$ (CIAS) based photovoltaic cells. The target was achieved and the FTO/p-CIAS/n-CdS/In structure was successfully tested for photovoltaic response. In achieving the target, another type of solar cell (FTO/p-Se/n-CdS/In) was also tested successfully. In addition to achieving the main objective, Se, γ-In_2Se_3 and CIAS thin films were successfully grown and optimised for their structural, optical, electrical, and compositional properties. Further, their current transport behaviour was tested and optimised. It was also observed that the undertaken materials can also be used for the fabrication of sensors, optical detectors, and transducers.

15. CONTRIBUTION TO THE SOCIETY:

The energy demand is increasing rapidly whereas, the resources of conventional energy are depleting very fast. Moreover, these conventional energy sources have created a lot of environmental issues therefore, there is an urge for the generation of energy using renewable energy sources. Several efforts have been made in this regard and solar energy has been found to be a viable alternative to conventional energy resources. Although silicon solar cells have been used widely but there are limitations in this technology. Research is, therefore, going on to make use of alternative materials to fabricate solar cells in order to achieve higher efficiency and better stability. Furthermore, there is an effort to decrease the effective thickness of the solar cells in order to make them more flexible.

In the present project, important aspects of solar cell materials and technology were studied. The results and findings would be highly useful for carrying forward this work to meet the future requirements of society. Further, the present time is an era of automation and sensors and detectors have a greater role in creating the automation system. The materials and thin films studied in the project have been used in the fabrication of sensors, optical detectors and transducers. So these may contribute to the future technology of these devices and systems.

16. WHETHER ANY PHD. ENROLLED/PRODUCED OUT OF THE PROJECT: yes Five PhD
have been awarded in this area during the intervening period.

17. NO. OF PUBLICATIONS OUT OF THE PROJECT: 22 (List of publications is mentioned
Above and five publications which pertain to the undertaken work are attached below)

(PRINCIPAL INVESTIGATOR)

(REGISTRAR/PRINCIPAL)

REGISTRAR
University of Jammu
Jammu.

51
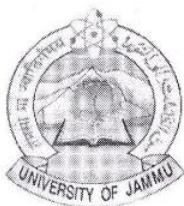
OFFICE OF THE DEAN RESEARCH STUDIES
UNIVERSITY OF JAMMU, JAMMU

No. 4469-70

Dated: 7/12/23

Prof. Naresh Padha
Principal Investigator UGC MRP
Department of Physics
University of Jammu
Jammu

Subject: Final Report Assessment certificate of UGC-MRP (F.No 43-398/2014(SR) Dated: 18th September, 2015 of Prof. Naresh Padha.

Sir,

With reference to your letter on the subject cited above, it is to inform you that the Vice-Chancellor has approved Dr. Balaji Rao, Head, Department of Nanoscience and Material, Central University of Jammu, Rahya-Suchani (Bagla), District Samba and Dr. Ashok Kumar Sharma, Professor, Department of Physics, SMVDU, Katra as experts for assessment of the final report of UGC Major Research Project entitled "Cu(In$_{1-x}$Al$_x$)Se$_2$ Thin Films Optimization, Device Fabrication and their use in Photovoltaic Applications". The expenditure for the TA/DA and honorarium of the experts shall be met out of appropriate head of the project grant .

Yours sincerely

7/12/2023
Assistant Registrar (R&A)

REGISTRAR
University of Jammu
Jammu.

Copy to:

1. Head, Department of Physics, University of Jammu
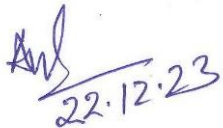
52

UNIVERSITY GRANTS COMMISSION
BAHADUR SHAH ZAFAR MARG
NEW DELHI – 110 002

ASSESSMENT CERTIFICATE
(to be submitted with the proposal)

It is certified that the proposal entitled "$Cu(In_{1-x}Al_x)Se_2$ **Thin Films Optimization, Device Fabrication and their use in Photovoltaic Applications**" by **Prof. Naresh Padha, Dept. of Physics, University of Jammu** has been assessed by the two-member experts committee consisting of the following members for submission to the University Grants Commission, New Delhi for financial support under the scheme of Major Research Projects:

Details of Expert Committee:

S.No.	Name of Expert	Name of Department	Signature with Date
1.	Prof. R. Balaji Rao	Head, Dept. of Nanoscience and Material, Central University of Jammu, Samba, Jammu.	
2.	Prof Ashok Kumar Sharma	Professor, Dept. of Physics, Shri Mata Vaishno Devi Univ. Katra, Jammu	

विभागाध्यक्ष / Head
नैनो विज्ञान एवं पदार्थ विभाग
Department of Nano Sciences & Materials
जम्मू केंद्रीय विश्वविद्यालय
Central University of Jammu

Dr. Ashok Kumar Sharma
Professor
School of Physics
Shri Mata Vaishno Devi University
Kakryal, Katra-182320 (J&K) India

The proposal is as per the guidelines.

(REGISTRAR/ PRINCIPAL)
REGISTRAR
University of (Seal)
Jammu.

53

Final Report Assessment / Evaluation Certificate
(Two Members Expert Committee Not Belonging to the Institute of Principal Investigator)
(to be submitted with the final report)

It is certified that the final report of the Major Research Project entitled "**Cu(In$_{1-x}$Al$_x$)Se$_2$ Thin Films Optimization, Device Fabrication and their Use in Photovoltaic Applications.**" by Dr./Prof. **Naresh Padha** Dept. of **Physics, University of Jammu** has been assessed by the committee consisting of the following members for final submission of the report to the UGC, New Delhi under the scheme of Major Research Project.

Comments/Suggestions of the Expert Committee:-

The research undertaken in the project has been carried out systematically and is very well structured. The findings are clear and focused. The goals set for this project have been achieved. The outcomes of the projects provide an ample scope for meeting the future needs of society. It is proposed that the research should be extended to the areas of photodetectors and sensors as mentioned by the principal investigator in the findings of this report.

Name & Signatures of Experts with Date:-

S.N.	Name of Expert	University/College name	Signature with Date
1.	Prof. R. Balaji Rao	Professor and Head Dept. of Nanoscience and Material, Central University of Jammu, Samba, Jammu.	28/12/2023 विभागाध्यक्ष / Head नैनो विज्ञान एवं पदार्थ विभाग Department of Nano Sciences & Materials जम्मू केंद्रीय विश्वविद्यालय Central University of Jammu
2.	Prof Ashok Kumar Sharma	Professor, Dept. of Physics, Shri Mata Vaishno Devi Univ. Katra, Jammu	Dr. Ashok Kumar Sha Professor School of Physics Shri Mata Vaishno Devi Un Katra-182320 (J&K)

It is certified that the final report has been uploaded on UGC-MRP portal on .... It is also certified that the final report, Executive summary of the report, Research documents, and monograph academic papers provided under Major Research Project have been posted on the website of the University/College.

(Registrar/Principal)
Seal
REGISTRAR
University of Jammu
Jammu.

54

Influence of temperature on Al/p-CuInAlSe$_2$ thin-film Schottky diodes

Usha Parihar[1] · Jaymin Ray[2] · C. J. Panchal[3] · Naresh Padha[1]

Abstract Al/p-CuInAlSe$_2$ Schottky diodes were fabricated using the optimized thin layers of CuInAlSe$_2$ semiconductor. These diodes were used to study their temperature-dependent current–voltage (I–V) and capacitance–voltage (C–V) analysis over a wide range of 233–353 K. Based on these measurements, diode parameters such as ideality factor (η), barrier height (ϕ_{bo}) and series resistance (R_s) were determined from the downward curvature of I–V characteristics using Cheung and Cheung method. The extracted parameters were found to be strongly temperature dependent; ϕ_{bo} increases, while η and R_s decrease with increasing temperature. This behavior of ϕ_{bo} and η with change in temperature has been explained on the basis of barrier inhomogeneities over the MS interface by assuming a Gaussian distribution (GD) of the ϕ_{bo} at the interface. GD of barrier height (BH) was confirmed from apparent BH (ϕ_{ap}) versus $q/2kT$ plot, and the values of the mean BH and standard deviation (σ_s) obtained from this plot at zero bias were found to be 1.02 and 0.14 eV, respectively. Also, a modified $\ln(J_s/T^2) - q^2\sigma_s^2/2k^2T^2$ versus q/kT plot for Al/p-CuInAlSe$_2$ Schottky diodes according to the GD gives ϕ_{bo} and Richardson constant (A^{**}) as 1.01 eV and 26 Acm^{-2} K^{-2}, respectively. The Richardson constant value of 26 Acm^{-2} K^{-2} is very close to the theoretical value of 30 Acm^{-2} K^{-2}. The discrepancy between BHs obtained from I–V and C–V measurements has also been interpreted.

1 Introduction

Cu(In,Al)Se$_2$ (CIAS) is a direct bandgap quaternary semiconductor, with bandgap varying between 1.0 eV (CIS) to 2.7 eV (CuAlSe$_2$) by Al addition, and has been found to be a potential candidate for low-cost solar cells [1]. Further, there are two main families of possible photovoltaic devices in the form of metal-to-semiconductor Schottky and semiconductor–semiconductor of homo-/hetero-junction variety. The later can be made via the same semiconductor through different types of doping, yielding relatively more complex structure compared to MS Schottky junction [2, 3].

Moreover, metal–semiconductor structures are important research tools for the characterization of new semiconductor materials and simultaneously play a vital role in constructing some useful devices [4, 5]. The electrical properties of the Schottky contacts depend on the density of interface states, and therefore, the control of interface quality has been found promising for device performance, stability and reliability [6]. The current–voltage (I–V) characteristics of the Schottky diode measured at room temperature do not provide satisfactory information about the conduction process and the nature of barrier at the metal–semiconductor (MS) interface, whereas the temperature-dependent I–V characteristics allow us to understand the different aspects of the conduction mechanisms. Thermionic emission (TE) current transport mechanism has widely been used to extract the Schottky diode parameters; however, several anomalies have been reported at both low and high temperatures [7–12]. Further, it has

✉ Jaymin Ray
  jayminray@gmail.com

1 Department of Physics and Electronics, University of Jammu, Jammu, J&K, India

2 Department of Physics, Indian Institute Teacher Education, Gandhinagar, Gujarat, India

3 Applied Physics Department, The M.S. University of Baroda, Vadodara, Gujarat, India

Springer

55

been found that BH (ϕ_{bo}) increases and ideality factor (η) decreases with increasing temperature [13–16]. Various models have been used to explain these deviations. Some authors suggest 'inhomogeneities at a real MS interface' be the cause of the anomalous behavior [8–12]. Further, the same authors suggest that the temperature dependence of BHs and ideality factors can be successfully explained on the basis of TE coupled with GD of BHs. The ballistic electron emission microscopy (BEEM) has also supported the existence of a GD of the BHs in Schottky diodes [16]. In addition, we could say the study of the absorber layer in Schottky diode application to explore the capability of the material to be used in other optoelectronics devices. Regarding the photovoltaic devices, one could try for by taking the thinner aluminum contact in order to use it as a Schottky solar cell.

In this paper in addition to the temperature-dependent I–V, C–V measurements, in the temperature range 233–353 K, of Al/p-CuInAlSe$_2$ Schottky diodes are reported and studied. The temperature dependence of BHs and ideality factors has been interpreted on the basis of existence of GD of the BHs around a mean value.

2 Experimental details

Polycrystalline chalcopyrite composition $CuIn_{1-x}Al_xSe_2$ (CIAS) with $x = 0.19$ was prepared by using melt-quenching method as described earlier [17]. Thin films of this material were then deposited on organically cleaned glass substrate under varying substrate temperatures and film thicknesses by using flash evaporation techniques [17]. In order to prepare Al/p-CuInAlSe$_2$ Schottky diodes, initially silver was deposited over organically cleaned glass substrate which was followed by the flash deposition of 700 nm thick annealed CIAS layer. The annealing for this purpose was performed at 573 K for the duration of 1 h in a vacuum chamber at a base pressure of 10^{-2} mbar. Finally, circular Schottky diodes of area 6×10^{-3} cm^2 were formed by thermally depositing aluminum over the optimized CIAS layer. The rate of deposition of all the metals was kept at 0.5–0.6 nm s^{-1}, whereas rate of 0.3–0.4 nm s^{-1} was maintained for CIAS deposition at a base pressure of 2×10^{-6} mbar. The prepared diodes were then tested for the temperature-dependent (233–353 K) I–V as well as capacitance–voltage (C–V) behavior using computer-interfaced I–V/C–V setup comprising of a programmable source meter (Keithley make, model 2400), precision programmable LCR meter (Agilent make, model 4284A), Hot plate, thermocouple, cryogenic setup (Lake Shore make, model Cryodyne 22CP CTI) equipped with compressor (model 8200 CTI) and temperature controller (Lake Shore make, model 321). The interfacing of these instruments was established by using LabVIEW software by National Instruments, USA.

3 Results and discussion

3.1 Current–voltage–temperature analysis

The temperature-dependent I–V characteristics of Al/p-CuIn$_{0.81}$Al$_{0.19}$Se$_2$ Schottky diodes of the area of 6×10^{-3} cm^2 in the temperature range from 233 to 353 K are shown in Fig. 1. The reverse characteristics of the diode demonstrate nonsaturating response with bias as shown in Fig. 1. The behavior may be explained on the basis of the spatial inhomogeneity of BH [11]. For inhomogeneous MS contacts, the reverse characteristics may be dominated by the current which flow through the low-BH patches. The semilogarithmic forward I–V curves as shown in Fig. 1 have also been found nonlinear in nature; the nonlinearity in the I–V characteristics is a complex feature which arises due to several factors when a number of noninteracting parallel diodes with a GD of BHs act simultaneously, and thus is not preferred for the extraction of barrier parameters [18]. However, the linear range of the forward I–V plot in the undertaken diodes is short; therefore, the determination of the diode parameters using it is not possible. Thus, an alternative approach developed by Cheung and Cheung [19] in the light of Eqs. (1) and (2) has been used to extract Schottky diode parameters corresponding to downward curvature of temperature-dependent forward I–V plots (Fig. 1). The ideality factors (η), BHs (ϕ_{bo}) and series resistances (R_s) as measured on the basis of Eqs. (1) and (2) are presented in Table 1.
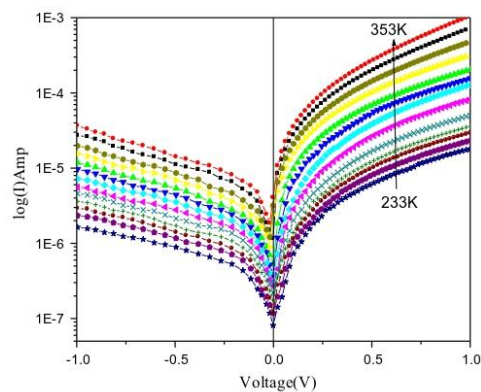

Fig. 1 log(I) versus V characteristics of Al/p-CuIn$_{0.81}$Al$_{0.19}$Se$_2$ Schottky diode

56

**Table 1** Diode parameters extracted from temperature-dependent I–V characteristics by Cheung's method

Temp. (K)	Ideality factor (η)	Barrier height ϕ_{IV} (eV)	Barrier height ϕ_{CV} (eV)	Series resistance R_s (kΩ)	Acceptor density of states $\times 10^{19}$ N_A (cm^{-3})
233	6.40	0.46	0.81	36	0.97
243	4.15	0.49	0.79	31	1.02
253	3.10	0.52	0.78	29	1.08
263	2.53	0.54	0.76	25	1.09
273	2.26	0.56	0.74	21	1.13
283	2.02	0.57	0.73	14	1.17
293	1.76	0.59	0.71	10	1.23
303	1.64	0.60	0.68	7	1.44
318	1.54	0.61	0.67	5	1.74
323	1.41	0.62	0.66	4	1.76
333	1.28	0.64	0.65	3	1.83
343	1.18	0.64	0.63	2	1.93
353	1.13	0.65	0.62	1	2.01

$$\frac{d(V)}{d(\ln J)} = R_s AJ + \frac{\eta}{\beta} \qquad (1)$$

$$H(J) = R_s AJ + \eta \phi_{bo} \qquad (2)$$

As shown in Table 1, the values of ϕ_{bo} for the Al/p-CuIn$_{0.81}$Al$_{0.19}$Se$_2$ Schottky diodes vary significantly from 0.46 to 0.65 eV, while η changes from 6.40 to 1.13 for the temperature range from 233 to 353 K. Such high value of ideality factor at 233 K, compare to the 353 K, is may be due to the interface roughness, interfacial reactions, diffusion/interdiffusion of the contaminations of applied materials on semiconductor surface, inhomogeneities of thickness and composition of the layer and nonuniformity of interfacial charges or the presence of a thin insulating layer, because of trace quantities of oxygen, between the metal and the semiconductor [20]. Figure 2 shows the graphical representation of experimental value of ϕ_{bo}, η as in the temperature of 233–353 K.

Since current transport across the metal–semiconductor interface is a temperature-activated process, electrons at low temperature pass over the lower barriers and the current is dominated by diodes with lower SBH and a larger ideality factor. In other words, as the temperature increases, more and more electrons have sufficient energy to overcome the higher barrier; thus, the dominant BH will increase with the temperature [21, 22]. Further, the higher values of the ideality factor ($\eta > 1$) indicate deviation of the current mechanism from TE theory. Idealities greater than one can also be attributed to the presence of a thick interfacial insulator layer between the metal and semiconductor [1, 23].
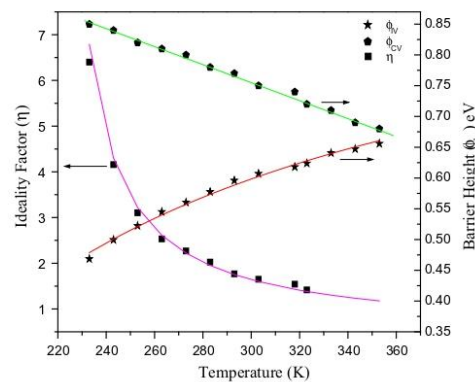
Fig. 2 Barrier height (ϕ_{CV}) obtained from C–V data and zero-bias barrier height (ϕ_{IV}) as well as the ideality factor (η) for the Al/p-CuInAlSe₂ Schottky diodes obtained from the forward bias I–V data at various temperatures

Moreover, the variation of series resistance with temperature can be seen from Table 1 which depicts a decrease in its value with increase in temperature; the change is more predominant at low temperatures in comparison with high temperatures. Such behavior of series resistance variation has been ascribed to the particular distribution of the interface states. In the case of metal–semiconductor interface as explained above, the electrons at low temperature pass over the lower barriers and therefore current will flow through patches of the lower Schottky BH and results in a larger ideality factor and hence higher series resistance [24].

3.2 Richardson plots

Thermionic emission theory is normally used to extract the SBD parameters. However, there have been several reports about the deviation of these parameters from this classical TE theory [8, 25]. One can also evaluate the BH by using the Richardson plot of the saturation current as follows,

$$\ln\left(\frac{J_s}{T^2}\right) = \ln(A^{**}) - \frac{q\phi_{bo}}{KT} \tag{3}$$

According to Eq. (3), the plot of ln (J_s/T^2) versus 1000/T provides a straight line with slope giving the activation energy and intercept at the ordinate yielding the effective Richardson constant (A^{**}). However, the plot of ln (J_s/T^2) versus 1000/T of the experimental data has been found deviating from linearity below 293 K (refer Fig. 3).

The nonlinearity may be explained on the basis of temperature dependence of η and ϕ_{bo} as been reported by several authors [14–16]. The experimental data fit asymptotically with a straight line, yielding Richardson constant (A^{**}) value of 2.14 × 10^{-4} Acm^{-2} K^{-2}. This value of A^{**} is lower than the reported A^{**} (=30 Acm^{-2} K^{-2}) value of CIS. The deviation in the Richardson plot as well as A^{**} value may be due to image force lowering, tunneling current, recombination in the space charge region appearing at low voltage and variation of the charge distribution near the interface [26]. According to Horvath [7], the A^{**} value obtained from the temperature-dependent I–V characteristics may be affected by the lateral inhomogeneity of the barrier and the fact that it is different from the theoretical value may be connected to real effective mass which is different from that of the calculated one.
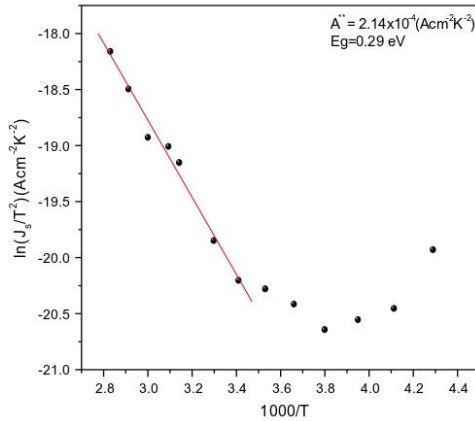
Fig. 3 Richardson plot of ln(J_s/T^2) versus 1000/T for Al/p-CuInAlSe$_2$ SBD

3.3 Barrier height inhomogeneities

Barrier height inhomogeneity model is based on an assumption that there are large number of parallel diodes having different SBD's, and every SBD can independently make contribution to the current so that the total current across the diode is sum of the current flowing in individual diodes with different areas; however, the apparent BH (ϕ_{ap}) and ideality factor (η_{ap}) are both temperature dependent [8, 11]. The above discussed contact behavior has been explained on the basis of an 'Analytical Potential Fluctuation Model' which assumes spatially inhomogeneous BHs at the interface [7, 27]. This model propagates that the distribution of the BHs is Gaussian in character with a mean value (ϕ_{bo}) and a standard deviation (σ_s), and is described as [9, 27].

$$P(\phi_{bo}) = \frac{1}{\sigma\sqrt{2\pi}}\exp\left(\frac{\phi_{bo} - \bar{\phi}_{bo}}{2\sigma_s}\right) \tag{4}$$

where $1/\sigma_s\sqrt{2\pi}$ is the normalization constant of the Gaussian barrier height distribution. The total current I(V) across a Schottky diode containing barrier inhomogeneities for any forward bias V is then given by,

$$I(V) = \int I(\phi_{bo}, V)P(\phi_{bo})d\phi \tag{5}$$

$$I(V) = A^{**}T^2 \exp\left[\frac{-q}{KT}\left(\bar{\phi}_{bo} - \frac{\sigma_s^2 q}{2KT}\right)\right]\exp\left(\frac{q(V_s)}{KT}\right)$$
$$\times \left[1 - \exp\left(\frac{-q(V_s)}{KT}\right)\right] \tag{6}$$

with,

$$I_s = AA^{**}T^2\exp\left(\frac{q\phi_{ap}}{KT}\right) \tag{7}$$

where η_{ap} and ϕ_{ap} are the apparent ideality factor and BH at zero bias, respectively, and the later is given by,

$$\sigma_{ap} = \bar{\phi}_{bo}(T=0) - \frac{\sigma_s^2 q}{2KT} \tag{8}$$

In the ideal case ($\eta = 1$), the expression is obtained as,

$$\left(\frac{1}{\eta_{ap}} - 1\right) = \rho_2 - \frac{q\rho_3}{KT} \tag{9}$$

The temperature dependence of σ_s is usually small and thus can be neglected [16]. However, it is assumed that σ_s and ϕ_{bo} are linearly bias dependent on Gaussian parameters such that $\bar{\phi}_b = \phi_{bo} + \rho_2 V$ and $\sigma_s = \sigma_{so} + \rho_3 V$, where ρ_2 and ρ_3 are the voltage coefficients that may depend on temperature and they quantify the voltage deformation of the BH distribution [16]. It is obvious that the decrease in zero-bias BH is caused by the existence of the GD, and the
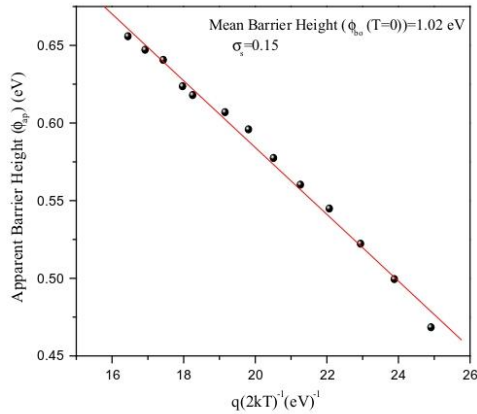
Fig. 4 Zero-bias apparent barrier height (ϕ_{ap}) versus $q/2KT$ Al/p-CuInAlSe₂ Schottky diode as per to Gaussian distribution of the barrier heights
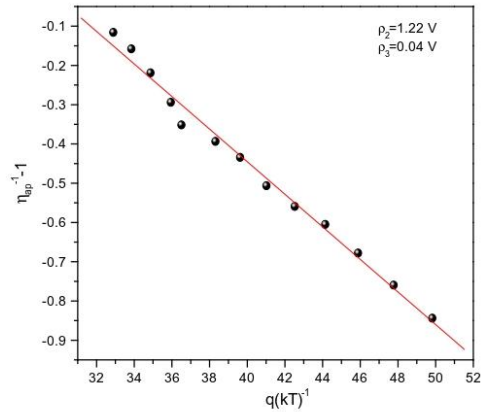

Fig. 5 Ideality factor (η_{ap}) versus q/KT plot of Al/p-CuInAlSe₂ Schottky diodes as per to Gaussian distribution of the barrier heights

extent of influence is determined by the standard deviation itself. Also, the effect is particularly significant at low temperatures. On the other hand, the abnormal increase in ideality factor occurs due to the variation of mean BH and standard deviation with bias, i.e., terms involving voltage coefficients ρ_2 and ρ_3.

The plot of ϕ_{ap} versus $q/2KT$ shown in Fig. 4 should be a straight line giving mean BH (ϕ_{bo}) and standard deviation (σ_s) as intercept and slope with values of 1.02 and 0.15 eV, respectively.

The solid line curves in Fig. 2 represent data generated from these parameters on their re-substitution to Eq. (8). This plot obeys TE model comprising GD of BHs given by the Eq. (8). By comparing ($\bar{\phi}_{bo}$) and (σ_s) parameters, it is seen that the standard deviation (a measure of the barrier inhomogeneity) is ≈ 15 % of the mean BH value. It has been noted that the lower value of σ_s corresponds to a more homogeneous character of BHs, the result thus indicates Al/p-CuInAlSe₂ Schottky diodes to possess inhomogeneous BH character, and these inhomogeneities as per the GD function represented in Eqs. (8) and (9). The cause of these deviations may be attributed to the variation in the composition of the interfacial oxide layer, nonuniformity of interfacial charges and variation of the interfacial oxide layer thickness, etc. [9, 14]. The temperature dependence of the ideality factor has been established to be controlled by lognormal function as represented by Eq. (9). The fitted ideality factor η plot shown in Fig. 5 is a straight line that gives voltage coefficients $\rho_2 = 1.22$ V and $\rho_3 = 0.04$ V from the intercept and slope. Furthermore, as can be seen from Fig. 5, the experimental results of η show good agreement with Eq. (9) for the same parameters. The linear
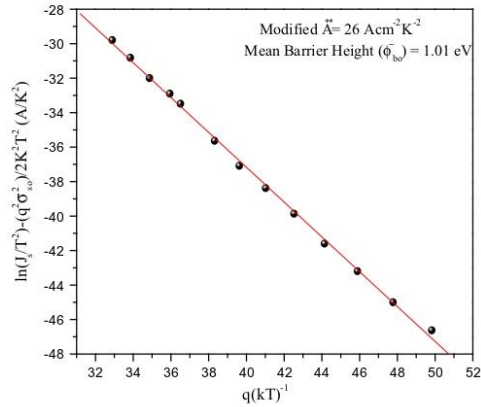
Fig. 6 Modified $\ln(J_s/T^2) - (q^2\sigma_s^2/2k^2T^2)$ versus q/kT plot for Al/p-CuInAlSe₂ Schottky diodes

plot of $(1/\eta_{ap} - 1)$ versus q/kT confirms that the ideality factor does indeed denote the voltage deformation of the GD of the BH. The continuous line in Fig. 2 represents data estimated with these parameters.

The Richardson plot presented at Fig. 3 according to Eq. (3) is now modified by combining Eqs. (8) and (9) we get,

$$\ln\left(\frac{J_s}{T^2}\right) - \left(\frac{q^2\sigma_s^2}{2k^2T^2}\right) = \ln(A^{**}) - \frac{q\overline{\phi_{bo}}}{kT} \qquad (10)$$

The modified $\ln(J_s/T^2) - (q^2\sigma_s^2/2k^2T^2)$ versus q/kT plot, given in Fig. 6, should also be a straight line with the

🔷 Springer

59

slope and the intercept at the ordinate yielding the mean BH ($\bar{\phi}_{bo}$) and A^{**}, respectively. The modified Richardson plot shows linearity according to the GD of BHs over the entire temperature range corresponding to single activation energy around ($\bar{\phi}_{bo}$) value. By the least squares linear fitting of the data, $\bar{\phi}_{bo} = 1.01$ eV it can be seen that the value of $\bar{\phi}_{bo}$ is in close agreement with the value of $\phi_{bo} = 1.02$ V obtained from the plot of ϕ_{ap} versus $q/2kT$ shown in Fig. 4, while modified Richardson constant $A^{**} = 26$ Acm^{-2} K^{-2} is found to be in close agreement with the theoretical value of $A^{**} = 30$ Acm^{-2} K^{-2}. The modifications in the Richardson equations on adding the current components determined on the basis of barrier inhomogeneities caused barrier parameters $\bar{\phi}_{bo}$ and A^{**} to shift closer to their reported values, thus confirming the existence of 'barrier inhomogeneities.'

3.4 Capacitance–voltage–temperature (C–V–T) analysis

The C–V relationship for Schottky diode is [3, 4],

$$\frac{1}{C^2} = \left(\frac{2}{\varepsilon_s q N_a A^2}\right)\left(V_{bi}\frac{kT}{q} - V\right) \tag{11}$$

where ε_s is the permittivity of the semiconductor ($\varepsilon_s = 8.1\varepsilon_0$), V is the applied voltage. The x-intercept of the plot of ($1/C^2$) versus V gives V_0, and it is related to the built in potential V_{bi} by the equation:

$$V_{bi} = V_o + \frac{KT}{q} \tag{12}$$

where T is the absolute temperature. The BH is given by the equation,

$$\phi_{bo} = V_0 + \frac{KT}{q} + V_n \quad \text{or} \quad \phi_{bo} = V_{bi} + V_n \tag{13}$$

Here,

$$V_n = \left(\frac{kT}{q}\right)\ln\left(\frac{N_v}{N_A}\right) \tag{14}$$

The density of states in the conduction band edge is given by,

$$N_v = 2\left(\frac{2\pi m_e kT}{h^2}\right)^{3/2} \tag{15}$$

where m^* is hole effective mass ($m^* = 0.71\ m_o$) for CuInSe$_2$, h is the Planck's constant, and k is the Boltzmann constant. In order to access the doping concentration and BH reverse bias, C^{-2}–V characteristics of the Al/p-CuInAlSe$_2$ SBD in the temperature range of 233–353 K were obtained as shown in Fig. 7.

The junction capacitance is measured at a frequency of 1 MHz. The experimental C^{-2}–V plot measured at different temperatures has been found deviating from linearity. The nonlinearity of the curves indicates that the carrier concentration at the diode interface is not uniform. Further to that, the slope of the curves decreases with increasing bias, indicating an increase in N_A with increasing bias. This case indicates the presence of acceptor like deep traps (i.e., neutral when occupied, positively charged when empty) within the space charge region. The charge state of the acceptor like traps will depend on the position of the Fermi level.

The estimated Schottky BH of Al/p-CuInAlSe$_2$ Schottky diode is in the range of 0.81 eV at 233 K to 0.62 eV at 353 K, respectively (shown in Table 1). It is noted that the BH obtained from CV plot (ϕ_{CV}) increased with decrease in temperature. However, the BH obtained from the I–V curve decreases with decrease in temperature; this is attributed to inhomogeneous MS contacts. In the present case, the current transport at low temperatures has been dominated by current flowing through the patches of the lower BH with larger ideality factor as a result of the inhomogeneous MS contacts. The dominant BH obtained from the forward bias I–V characteristics will increase with the temperature due to barrier inhomogeneity in MS interface. This may be the reason of why the characteristics of the BH versus temperature plot obtained from the C–V measurements are completely opposite to those obtained from the I–V measurements [11]. Also, as clearly seen from Fig. 2, ϕ_{CV} increases with decreasing temperature as per the equation given as under:
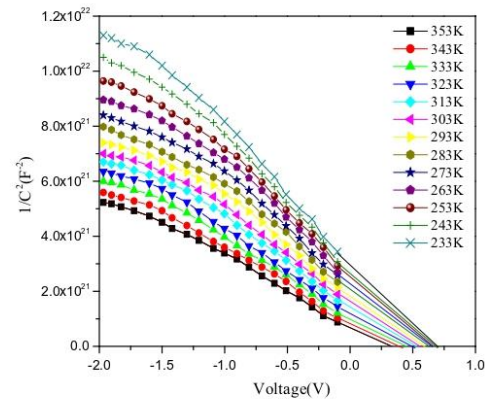
$$\phi_{CV} = \phi_{CV}(T = 0K)\alpha T \tag{16}$$

Fig. 7 Reverse bias C^{-2}–V characteristics of Al/p-CuInAlSe$_2$ SBD in the temperature range of 233–353 K
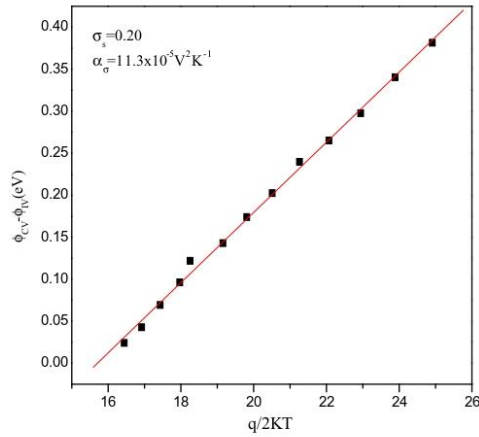
60

Fig. 8 Barrier height difference between values as derived from conventional evaluation of I–V and C–V data as a function of inverse temperature

where ϕ_{CV} ($T = 0$ K) is the BH extrapolated to zero temperature and α is the temperature coefficient of the BH. The linear fit of Eq. (16) to the experimental data in Fig. 2 yields ϕ_{CV} ($T = 0$ K) = 1.1 eV and $\alpha = -1.4 \times 10^{-3}$ eVK^{-1}.

Furthermore, it can be seen that the apparent BH from the experimental forward bias I–V plot is also related to the mean BH $\bar{\phi}_{IV} = \bar{\phi}_{CV}$ from the experimental reverse bias C^{-2}–V plot [8, 28]. The capacitance depends only on the mean band bending and is insensitive to the standard deviation (σ_s) of the barrier distribution [8, 28]. The relationship between ϕ_{IV} and ϕ_{CV} is given by [8, 28],

$$\phi_{CV} - \phi_{IV} = -\frac{q\sigma_s^2(T=0)}{2kT} + \frac{q\alpha_\sigma}{2k} \tag{17}$$

where α_σ is attributed to the temperature dependence of σ_s.

Figure 8 shows the experimental (ϕ_{CV}–ϕ_{IV}) versus $q/2kT$ plot according to Eq. (17). The plot should give a straight line with the slope providing the value of $\sigma_s = 0.20$ and y-axis intercept giving the value of $\alpha\sigma = 11.3 \times 10^{-5}$ V^{2}K^{-1}. The value of σ_s so obtained has been found in close agreement with the value of $\sigma_s = 0.15$ obtained from the plot of ϕ_{ap} versus $q/2kT$ shown in Fig. 4. This value of σ_s, however, is not small when compared with the mean BH value of 1.01 eV obtained from Fig. 4. Therefore, this may cause significantly large potential fluctuations particularly to the low temperature I–V data and could be responsible for the curved behavior of the conventional Richardson plot as shown in Fig. 3.

4 Conclusions

The effect of temperature on Al/p-CuInAlSe₂ Schottky diodes was investigated, wherein the nonideal I–V behavior of the Schottky diodes as displayed from its experimental data has been attributed to change in BH due to interface states defects, dislocations, surface states, series resistance, etc. The deviations from the experimental data have been explained on the basis of 'barrier height inhomogeneities' at the interface whose contribution when added confirmed the existence of TE phenomenon. The undertaken diodes were found to possess inhomogeneous BH character with a standard deviation of 15 % to the mean BH and were found to vary as per the GD function. The Richardson plot after inclusion of the current component generated on the basis of barrier inhomogeneities provided modified A^{**} and ϕ_{bo} values which are in close agreement with the reported ones. Existence of inhomogeneities has also been substantiated by the C–V analysis.

References

1. W.N. Shafarman, R. Klenk, B.E. McCandless, J. Appl. Phys. **79**, 7324 (1996)
2. T. Markvart, *Solar Electricity* (Wiley, England, 2000)
3. S.M. Sze, *Physics of Semiconductor Devices* (Wiley, New Jersey, 2007)
4. E.H. Rhoderick, R.H. Williams, *Metal–Semiconductor Contacts* (Clarendon Press, Oxford, 1978)
5. R.T. Tung, Mater. Sci. Eng.: R **35**, 131 (2001)
6. Z.J. Horvath, J. Mater. Sci. B **28**, 429 (1994)
7. Z.J. Horvath, Solid-State Electron. **39**, 176 (1996)
8. J.H. Werner, H.H. Güttler, J. Appl. Phys. **69**, 1522 (1991)
9. Y.P. Song, R.L. Van Meirhaeghe, W.F. Laflere, F. Cardon, Solid-State Electron. **29**, 633 (1986)
10. R.F. Schmitsdorf, T.U. Kampen, W. Möonch, Surf. Sci. **324**, 249 (1995)
11. J.P. Sullivan, R.T. Tung, M.R. Pinto, W.R. Graham, J. Appl. Phys. **70**, 7403 (1991)
12. R.T. Tung, Appl. Phys. Lett. **58**, 2821 (1991)
13. S. Chand, J. Kumar, J. Appl. Phys. **80**, 288 (1996)
14. W. Möonch, J. Vac. Sci. Technol., B **17**, 1867 (1999)
15. S.Y. Zhu, R.L. Van Meirhaeghe, Solid-State Electron. **44**, 663 (2000)
16. S. Chand, J. Kumar, Semicond. Sci. Technol. **10**, 1680 (1995)
17. U. Parihar et al., Mater. Chem. Phys. **139**, 270 (2013)
18. S. Chand, J. Kumar, J. Appl. Phys. **82**, 10 (1997)
19. S.K. Cheung, N.W. Cheung, Appl. Phys. Lett. **49**, 85 (1986)
20. Y.G. Chen, M. Ogura, H. Okushi, Appl. Phys. Lett. **82**, 4367 (2003)
21. M.B. Reddy, A.A. Kumar, Curr. Appl. Phys. **9**, 972 (2009)
22. F.A. Padovani, R. Stratton, Solid-State Electron. **9**, 695 (1996)
23. F.E. Cimili, M. Saglam, H. Efeoglu, A. Turut, Phys. B **404**, 344 (2009)
24. M. Soylu, B. Abay, Microelectron. Eng. **86**, 88 (2009)
25. S. Chand, J. Kumar, J. Appl. Phys. A **63**, 171 (1996)
26. N. Newman, M.V. Schilfgaarde, Phys. Rev. B **33**, 1146 (1986)
27. H. Norde, J. Appl. Phys. **50**, 5052 (1979)
28. H.H. Guttler, J.H. Werner, Appl. Phys. Lett. **56**, 1113 (1990)

61

Publication 2nd

Effect of CuIn$_{1-x}$Al$_x$Se$_2$ (CIAS) thin film thickness and diode annealing temperature on Al/p-CIAS Schottky diode

USHA PARIHAR[1], JAYMIN RAY[2,]*, C J PANCHAL[3] and NARESH PADHA[1]

[1] Department of Physics and Electronics, University of Jammu, Jammu 180006, India
[2] Department of Physics, Uka Tarsadia University, Bardoli 394601, India
[3] Applied Physics Department, MS University of Baroda, Vadodara 390001, India
*Author for correspondence (jayminray@gmail.com)

Abstract. Al/p-CIAS Schottky diodes were fabricated by depositing aluminium (Al) on different flash evaporated copper–indium–aluminium–diselenide (CIAS) films of varying thickness. Further, all diodes were annealed at 573 K for an hour. The influence of p-CIAS film thickness and the thermal annealing of Al/p-CIAS Schottky diode were investigated by observing current–voltage (*I–V*) and capacitance–voltage (*C–V*) characteristics at room temperature. Various diode parameters, such as ideality factor (η), barrier height (ϕ_{bo}) and series resistance (R_s) were calculated using Cheung's and Norde methods. ϕ_{bo} found to increase with annealing as well as with increase in the film thickness. However, the value of η and R_s decreases with annealing and CIAS thickness. The effective density of states (N_v), acceptor density of states (N_A) and barrier height have been calculated from *C–V* measurements. Values obtained from CV analysis were well matched with *I–V* results. The value of N_v decreases and the value of N_A increases with the increase in the film thickness. Using *I–V* and *C–V* parameters, energy band gap for the prepared Al/p-CIAS diodes has been reconstructed.

Keywords. Thin film Schottky diode; current–voltage (*I–V*) measurement; capacitance–voltage (*C–V*) measurement; energy band diagram.

1. Introduction

In the recent years, many optoelectronic devices which have properties of barrier height enhancement and good thermal stability are getting more attention. Such devices are organic field effect transistors, photovoltaic cells, Schottky diodes, negative-resistance devices, switching and memory systems, thermistors, etc. [1–4]. In the category of photovoltaic cell and Schottky solar cell, CuIn$_{1-x}$Al$_x$Se$_2$ (CIAS) is a promising p-type direct band gap absorber layer, because the band gap of it can vary from 1.0 to 2.7 eV simply by varying Al/In ratio [5]. These affect electrical properties too. Many researchers focus on one or both properties of CIAS thin films.

In 1990, Gebicki *et al* [5] produced bulk semiconductor CIAS with *x* in the range between 0 and 1. The pure elements were supplied using a chemical transport method in which iodine was the transport agent [5]. The variations in lattice constants *a* and *c* with the composition were recorded. They were found to obey Vegard's law in both cases. In 1998, Itoh *et al* [6] reported the preparation of CIAS by depositing a stack of In(Al)/Cu/Se/Cu/Al(In) using vacuum evaporation and then heating the whole stack in vacuum. The results show that the resistivity and energy band gap of the CIAS thin films were found to increase with Al content.

In addition, non-linear changes in lattice constants *a* and *c* were reported with increased Al content. US researchers from the IEC at Delaware, produced single phase CIAS thin films using multisource elemental evaporation in which the elements Cu, In, Al and Se were co-evaporated onto soda-lime glass (SLG) or Mo-coated SLG substrate [7]. They reported that energy band gap was varied over the range of 1.0–1.74 eV with an increase in Al content. In addition to that for the first time, they have reported that the solar devices produced using CIAS absorber films; an efficiency of 11% was obtained for *x* = 0.26. Two years later, same group reported a device efficiency of 16.9% for a CIAS solar cell with absorber of thickness 2.0–2.5 μm and a band gap of 1.16 eV [8]. The increase in device performance was achieved due to significant improvements in the device fabrication process, such as the addition of thin Ga layer (5 μm) by sputtering onto the Mo-coated SLG substrate, which improvises the adhesion of the absorber film to the Mo back contact for temperatures >500°C. Reddy and Raja [9] reported the production of CuIn$_{1-x}$Al$_x$Se$_2$ thin films (with *x* = 0.7) by a four-source co-evaporation method with an aim of using such layers in tandem solar cell structure. Those films were single phase, stoichiometric and p-type in conductivity (ρ = 140 Ω cm). Takao Hayashi *et al* [10] deposited CIAS thin films by molecular beam epitaxy on a

Mo/SLG substrates by the three source evaporation process. Recently Kim *et al* [11] reported RF-sputtered 3-layer structure of CIAS thin film; they observed a low resistivity of the order of 10^{-2} Ω cm was obtained in the $CuIn_{1-x}Al_xSe_2$ thin films with $x = 0.74$.

Very few reports on Schottky devices based on quaternary semiconductor thin films have been reported. The metal semiconductor (MS) interface plays a major role in the functioning of any electronic and optoelectronic devices. Hence, major focus is on the electronic transport through the Schottky barrier height (SBH). New heterojunction thin film-based solar material is known for the low-cost high efficient devices, having a better control in the grain and the charge distribution. This envisioned the utilization of CIAS thin films for preparing and for feasibility study of Schottky diode. Considering the relevant and recent report i.e., Touati *et al* [12] reported Schottky device having 400-nm thick thermally evaporated CZTS thin film. They observed that the Schottky barrier height was 0.807 eV. The other Schottky parameters, such as series resistance and ideality factor were estimated by Cheung and Cheung method [13]. In the present work, we followed the same method for estimating the Schottky parameters. In addition, we have estimated the barrier height inhomogeneity at interface by Norde method [14]. Our earlier study focussed on the barrier height inhomogeneity of MS interface at different device temperatures [15] and the present study focusses on the influence of film thickness and the annealing temperature on the Al/CIAS Schottky devices. The structural, optical, morphological and electrical properties of CIAS were already reported in the previous work [16].

2. Experimental

Al/p-CIAS Schottky diodes were made by depositing $CuIn_{1-x}Al_xSe_2$ ($x = 0.19$) thin film on to the 500 nm thick silver (Ag), ohmic contact, coated glass substrate using flash evaporation method. The preparation method for $CuIn_{1-x}Al_xSe_2$ ($x = 0.19$) compound, used for evaporation, was well described in our earlier work [16]. In addition, we had deposited and optimized CIAS thin film according to the optimized deposition and annealing parameters as per the previous work done [16], viz. deposition temperature was 273 K, deposition rate was 0.3–0.4 nm s^{-1}, annealing temperature was 573 K, time duration of annealing was 1 h and the base pressure for annealing was 10^{-3} mbar. The thickness of the film was measured using quartz crystal thickness monitor (Hindhivac make). The Schottky contact, i.e., aluminium (Al) was deposited onto the glass/Ag (+ve ohmic contact)/CIAS structure using a stainless steel mask (diameter of 0.1 mm), at room temperature by thermal evaporation (technique) having a deposition rate of 0.5–0.6 nm s^{-1}. The thickness of CIAS and Al thin films was measured by quartz crystal thickness monitor. All evaporation processes were carried out in a vacuum coating unit

at about 10^{-6} mbar. In this work, we had prepared Schottky diodes by varying the thickness of the CIAS films viz. 200, 500 and 700 nm, and examined the influence of CIAS thin films thickness and thermal annealing on the Schottky diode parameters. The schematic diagram of CIAS Schottky diode and its measurement setup is shown in figure 1.

The fabricated CIAS Schottky diodes (glass/Ag/CIAS/Al) were tested by current–voltage (*I–V*) as well as capacitance–voltage (*C–V*) behaviours using computer interfaced *I–V/C–V* setup comprising of a programmable source meter (Keithley make, model 2400), precision programmable LCR meter (Agilent make, model 4284A), cryogenic setup (Janis make, model Cryodyne 22CP CTI) equipped with compressor (model 8200 CTI) and temperature controller (Lake Shore make, model 321). The interfacing of these instruments was established by using LabVIEW software by National Instruments, USA.

3. Results and discussion

3.1 *Current–voltage (I–V) characterization*

The semi-logarithmic current–voltage (*I–V*) characteristics, both forward and reverse biases of Al/CIAS Schottky diodes having a different thicknesses of CIAS thin film as well as annealed are shown in figure 2. *I–V* characteristics revealed that the diode current increases as the thickness is increased in forward bias. However, the same has been found to decrease with increase in thickness under reverse bias condition.

Improvement in the diode current for thicker and annealed Schottky diodes can be explained by the increase in grain size, reducing the grain boundaries and better enforcement of crystal growth [17]. To find the diode parameters from the *I–V* plot, one can notice from the non-linear region of the semi-logarithmic forward *I–V* curves caused by the presence of the effect of R_s, apart from that a complex facet arises due to a number of non-interacting parallel diodes with grain boundaries of barrier heights act simultaneously. This causes misplay in the extraction of diode parameters [18].

Similarly, semi-logarithmic reverse characteristics of the diode demonstrate non-saturating response can be explained on the basis of the spatial inhomogeneity of barrier heights [13], majorly due to the current flow through the low barrier heights patches. Again, there is a possibility to acquire faulty diode parameters. With the objective of accurately determining the ideality factor, barrier height and series resistance of the Al/CIAS Schottky contacts, Cheung's [13] method was employed. According to Cheung's functions, the relation between applied voltage and current can be written as:

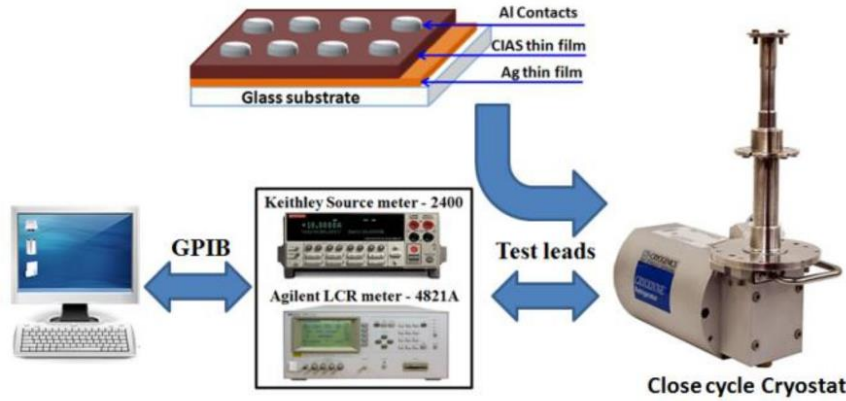$$\frac{d(V)}{d(\ln I)} = R_s I + \left(\frac{\eta kT}{q}\right). \tag{1}$$

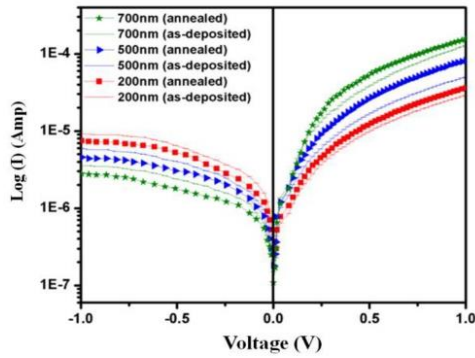**Figure 1.** Schematic of CIAS Schottky diodes and its measurement setup.

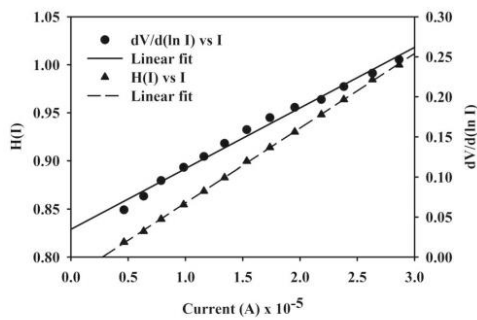**Figure 2.** Log (*I*)–*V* characteristics of as-deposited and annealed Al/p-CIAS Schottky diodes.

Figure 3. *d*(*V*)/*d*(ln *I*) and *H*(*I*) variations with respect to observed Schottky diode current.

Thus, a plot of *d(V)/d*(ln *I*) *vs. I* (shown in figure 3) will give the value of R_s and η. To evaluate ϕ_{bo}, we can define a function $H(I)$ given as:

$$H(I) = V - \left(\frac{\eta kT}{q}\right) \ln\left(\frac{I}{AA^{**}T^2}\right). \tag{2}$$

For equation (2), we can deduce:

$$H(I) = R_s I + \eta \phi_{bo}. \tag{3}$$

From the plot of $H(I)$ *vs. I* (shown in figure 3), we can determine the value ϕ_{bo} and R_s, which can be used to check the consistency in the values calculated from equation (1).

Thus, the calculated values of R_s, ϕ_{bo} and η of Al/CIAS diodes having different thicknesses, as deposited and annealed, are tabulated in table 1, and the variation is shown graphically in figure 4.

Looking at the ideality factor values of the diodes from table 1, one can reveal that there is an obvious improvement observed as the thickness of CIAS increases and on annealing. The best observed value of diode factor is 1.62 for 573 K annealed and 700 nm thick CIAS Schottky diode. Similarly, for the same fabrication condition of Schottky diode, we observed the minimum series resistance viz. 6.8 kΩ. Very negligible overall improvement in the barrier height, i.e., 0.57–60 eV can be observed.

According to equation (3), we can say that the high values of series resistance hinder precise evolution of barrier height. Norde [14] employed a method that evaluates barrier height from the standard *I–V* plot. The modified Norde function can be defined as:

$$F(V) = \frac{V}{\gamma} - \frac{kT}{q}\left(\frac{I(V)}{AA^{**}T^2}\right), \tag{4}$$

where γ is the first integer $>\eta$. Here, γ has been taken as 2, *A* the diode area = 9×10^{-2} mm^2, A^{**} effective Richardson

Table 1. Experimental values of barrier height (ϕ_{bo}) and ideality factor (η) are calculated using Cheung's function for Al/p-CIAS Schottky diodes with and without annealing.

CIAS thickness (nm)	Annealing temperature, T_a (K)	Barrier height, ϕ_{bo} (eV)	Ideality factor, η	Series resistance, R_s (kΩ)
200	Unannealed	0.57	2.06	13.7
	573	0.58	2.01	11.9
500	Unannealed	0.58	1.90	10.6
	573	0.59	1.83	9.3
700	Unannealed	0.59	1.76	8.1
	573	0.60	1.62	6.8
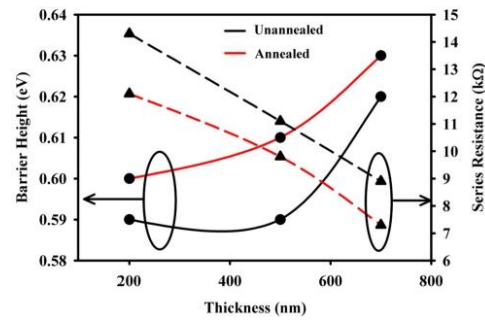
Figure 4. Variations in barrier height and series resistance as a function of CIAS film thickness, calculated using Cheung's function.

Figure 5. Norde's $F(V)$ variation with respect to applied voltage (V) for the Schottky diodes.

constant = 30 A cm^{-2} K^{-2} and the barrier height of device can be obtained by using:

$$\phi_{bo} = F(V_0) + \frac{V_0}{\gamma} - \frac{kT}{q}, \tag{5}$$

where $F(V_0)$ is the minimum value of $F(V)$ *vs.* V graph (shown in figure 5) and V_0 is the corresponding voltage.

The series resistance using Norde's method has been calculated through the relation:

$$R_s = \frac{kT(\gamma - \eta)}{qI}. \tag{6}$$

The values of barrier height and series resistance are tabulated in table 2. Very minute changes in the values of barrier height and series resistance were observed in comparison with Cheung's method (table 1). The ideality factor improves (decreases) and barrier height increases as thickness as well as annealing temperature increase. Improvement in the ideality factor implies that the current flows through the grains and its boundaries rather to the patches, that ultimately responsible to obtain the increasing behaviour of the barrier height with thickness and that of annealing temperature. Biber *et al* [19] also observed linear relationship between experimental effective barrier heights and ideality factors of Schottky contacts.

3.2 *Capacitance–voltage (C–V) characterization*

The basic C–V relationship for MS Schottky barriers was discussed in the earlier work [15,20]. $1/C^2$–V characteristics for as-deposited as well as annealed Al/p-CuIn$_{0.81}$Al$_{0.19}$Se$_2$ Schottky diodes have been presented in figure 6 (range is 0 to -2 V). The annealed samples provided lower value of capacitance as compared to corresponding as-deposited diodes, which caused increase in their barrier height values, since the lower capacitance values suggest a higher built-in voltage and consequently, a higher barrier height. The Schottky diode parameters extracted from $1/C^2$–V measurements have been illustrated in table 3.

The value of acceptor density of states (N_A) as calculated from the slope of reverse bias C^{-2}–V characteristics is found to be in the order of 10^{19} cm^{-3} and is in close agreement with that obtained from electrical analysis [15]. We have taken the dielectric constant of the film as 13.6 and the effective mass of hole is 0.71 for the calculation of C–V parameters. Table 3 suggests that as the thickness and annealing temperature increase, the values of N_A increase. The conclusions drawn from these parameters suggest that annealing the diodes leads to an increase in the barrier height and an improvement (decrease) in the ideality factor.

Table 2. Experimental values of barrier height (ϕ_{bo}) and series resistance (R_s) are calculated using the Norde's method for Al/p-CIAS Schottky diodes with and without annealing.

CIAS thickness (nm)	Annealing temperature, T_a (K)	Barrier height, ϕ_{bo} (eV)	Series resistance, R_s (kΩ)
200	Unannealed	0.59	14.3
	573	0.60	12.1
500	Unannealed	0.59	11.1
	573	0.61	9.8
700	Unannealed	0.62	8.9
	573	0.63	7.3

Table 3. Various electrical parameters deduced by the $1/C^2$–V measurement.

CIAS thickness (nm)	Annealing temperature, T_a (K)	Effective donor density of states $\times 10^{18}$ N_v (cm^{-3})	Effective acceptor density of states $\times 10^{19}$ N_A (cm^{-3})	Barrier height ϕ_{cv} (eV) (± 0.01)
200	Unannealed	1.15 ± 0.02	1.08 ± 0.02	0.74
	573	1.20 ± 0.03	1.12 ± 0.03	0.75
500	Unannealed	1.26 ± 0.03	1.11 ± 0.03	0.76
	573	1.31 ± 0.04	1.16 ± 0.01	0.77
700	Unannealed	1.38 ± 0.03	1.15 ± 0.02	0.77
	573	1.44 ± 0.02	1.21 ± 0.03	0.78
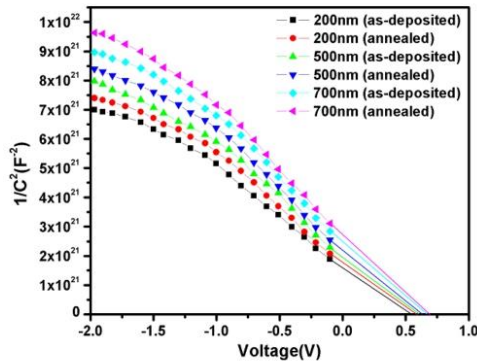
Figure 6. $1/C^2$–V characteristics of as-deposited and annealed Al/p-CIAS Schottky diodes.

3.3 *Energy band diagram of Al/p-CIAS Schottky diode*

Interfacial layer between the metal/semiconductor and the interface states plays a vital role in the determination of the Schottky barrier parameters. For the determination of electron affinity (χ) of the semiconductor, it has relation with the barrier height (ϕ_{bo}) and work function of the metal (ϕ_m), as follows:

$$q\phi_{bo} = E_g - q(\phi_m - \chi), \tag{7}$$

where ϕ_{bo} is the barrier height of Al/p-CuIn$_{0.81}$Al$_{0.19}$Se$_2$ Schottky diodes (0.78 eV) and E_g the band gap of the p-type semiconductor i.e., E_g = 1.24 eV [16].

The electron affinity (χ) of CuIn$_{0.81}$Al$_{0.19}$Se$_2$ has been calculated as 3.82 V. Further, the work function semiconductor (ϕ_s) has a relation with work function of the metal (ϕ_m) and built in potential (V_{bi}) as:

$$q\phi_s = q(\phi_m + V_{bi}). \tag{8}$$

The value of work function for p-CuIn$_{0.81}$Al$_{0.19}$Se$_2$ is equal to 4.98 eV. Using the above values of various parameters, equilibrium energy band diagram for the p-CuIn$_{0.81}$Al$_{0.19}$Se$_2$/Al Schottky diode has been plotted and presented in figure 7.

In the present case, the value of the metal work function is low compared to that of semiconductor (i.e., $\phi_m < \phi_s$), electrons will move from metal to semiconductor. Each electron flowing into the semiconductor removes a hole from the valence band, leaving neutralized charge of ionized acceptor in the semiconductor and thus, forming a potential barrier at the metal–semiconductor interface region [21]. Since the current in a p-type semiconductor is carried mainly by holes, the contact behaviour seems to be a Schottky with a barrier height of ∼0.78eV.

Alike with CIAS Schottky diode, rectifying characteristics of Pt/Al$_{0.08}$In$_{0.08}$Ga$_{0.84}$N Schottky diode show the barrier height and ideality factor as 0.76 eV and 1.03, respectively, by optimizing annealing temperature of the device [22]. Atasoy *et al* [23] reported the fabrication of
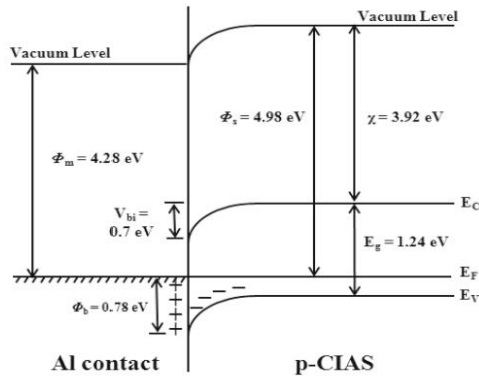
Figure 7. Energy band diagram of Al/p-CIAS Schottky diode.

Schottky diode based on Cu_2ZnSnS_4 (CZTS) films. They adopted the device structure as Mo/CZTS/Al, and observed the values of n and ϕ_{bo} as 4.5 and 0.84 eV, respectively. Similarly, Touati *et al* [12] prepared the same structure (Mo/CZTS/Al), but they have observed better ideality factor i.e., 1.4 compared to Atasoy *et al* [23] work and the barrier height was about 0.807.

4. Conclusion

Al/p-$CuIn_{0.81}Al_{0.19}Se_2$ Schottky diodes were fabricated and the effect of semiconductor layer thickness and annealing over the characteristics of Al/p-$CuIn_{0.81}Al_{0.19}Se_2$ Schottky diode has been analysed on the basis of current–voltage (I–V) as well as capacitance–voltage (C–V) measurements. The results showed obtrusive influence of thermal annealing on Al/p-$CuIn_{0.81}Al_{0.19}Se_2$ Schottky diode, which improved their quality by reducing the values of series resistance, ideality factor as well as reverse leakage current and increasing the barrier height. Thus, depicting reasonably good quality Schottky diodes formed with 700 nm annealed CIAS layer.

References

[1] Lloyd G, Raja M, Sellers I, Sedghi N, Di Lucrezia R, Higgins S *et al* 2001 *Microelectron. Eng.* **59** 323
[2] Zhu M, Cui T H and Varahramyan K 2004 *Microelectron. Eng.* **75** 269
[3] Moiz S A, Ahmed M M and Karimov K S 2005 *ETRI J.* **27** 319
[4] Aydin M E and Turut A 2007 *Microelectron. Eng.* **84** 2875
[5] Gebicki W, Igalson M, Zajac W and Trykozko R 1990 *J. Phys. D: Appl. Phys.* **23** 964
[6] Itoh F, Saitoh O, Kita M, Nagamori H and Oike H 1998 *Sol. Energy Mater. Sol. Cells* **50** 119
[7] Paulson P D, Haimbodi M W, Marsillac S, Birkmire R W and Shafarman W N 2002 *J. Appl. Phys.* **91** 10153
[8] Shafarman W N 2002 *Proc. 28th IEEE Photovoltaic Specialists Conference, USA*, p 519
[9] Reddy Y B K and Raja V S 2006 *Sol. Energy Mater. Sol. Cells* **90** 1656
[10] Takao Hayashi, Takashi Minemoto, Guillaume Zoppi, Ian Forbes, Kiyoteru Tanaka, Satoshi Yamada *et al* 2009 *Sol. Energy Mater. Sol. Cells* **93** 922
[11] Kim N-H, Jun Y-K and Lee W-S 2016 *J. Nanosci. Nanotechnol.* **16** 1583
[12] Touati R, Trabelsi I, Rabeh M B and Kanzari M 2017 *J. Mater. Sci.: Mater. Electron.* **28** 5315
[13] Cheung S K and Cheung W N 1986 *Appl. Phys. Lett.* **49** 85
[14] Norde H 1979 *J. Appl. Phys.* **50** 5052
[15] Parihar U, Ray J R, Panchal C J and Padha N 2016 *Appl. Phys. A* **122** 568
[16] Parihar U, Sreenivas K, Ray J R, Panchal C J, Padha N and Rehani B 2013 *Mater. Chem. Phys.* **139** 270
[17] Cova P and Singh A 1990 *Solid State Electron.* **33** 11
[18] Rau U, Taretto K and Siebentritt S 2009 *Appl. Phys. A* **96** 221
[19] Biber M, Gullu O, Forment S, Van Meirhaeghe R L and Turut A 2006 *Semicond. Sci. Technol.* **21** 1
[20] Kaufmann E N 2012 *Characterization of materials*, 2nd edn (New York: John Wiley & Sons)
[21] Sze S M 1981 *Physics of semiconductor devices* 2nd edn (New York: Wiley)
[22] Abd-Shukor R, Awang R, Deraman M, Kamisah M M and Shamsudin R 2012 *Adv. Mater. Res.* **501** 226
[23] Atasoy Y, Olgar M A and Bacaksiz E 2019 *J. Mater. Sci.: Mater. Electron.* **30** 10435

Development of CuInSe$_2$ thin films by SELD method for photovoltaic absorber layer application

Rajesh Niranjan, Arun Banotra & Naresh Padha

Springer

Springer

Development of CuInSe$_2$ thin films by SELD method for photovoltaic absorber layer application

Rajesh Niranjan[1] · Arun Banotra[1] · Naresh Padha[1]

Abstract

CuInSe$_2$ (CIS) films were obtained on annealing of 280 nm and 775 nm thick Cu/In/Se stacks deposited on corning glass substrate. The stacked elemental layer deposition (SELD) technique was used for the deposition of the films of Se, In and Cu layers. The as-deposited and annealed samples were found to possess polycrystalline structures. The films provided dominating CIS phase along with secondary phases of Cu$_{11}$In$_9$, CuSe and Se. The secondary phases present in the films vary with change in annealing temperatures. Moreover, single CuInSe$_2$ phase is observed in the 280 nm films at 523 K. The scanning electron microscopic images of the samples show nano-rod type structures of CIS grains. The elemental composition of Cu:In:Se approaches 1:1:2 in 280 nm thick samples. The ratio, however, deviates in the 775 nm thick films. The Raman spectra of these samples give A_1 mode at 173 cm^{-1} and confirm the presence of CIS phase. The films exhibit slow increase in the band gap (E_g) values from 1.09 to 1.22 eV for 775 films. However, comparatively higher band gap (E_g) values from 1.25 to 1.90 eV are observed for 280 nm films with high absorption co-efficient ($\alpha \sim 10^5$ cm^{-1}) values. The films present more useful electrical parameters for 280 nm thick samples as compared to 775 nm samples due to dominated CIS phase. Thus, obtained CIS thin films of 280 nm thickness provide viable alternative as an absorber layer in solar cell structure.

1 Introduction

CuInSe$_2$ chalcopyrite material (CIS) has attracted considerable interest on account of its applications in photovoltaic and optoelectronic devices viz. diodes, originators of laser beams, light detectors and solar cells, etc. [1, 2]. It has been widely used as an absorber layer in the solar cells structure due to its direct band gap ($E_g \sim 1.04$ eV), high absorption co-efficient value ($\alpha \sim 10^5$ cm^{-1}), radiation-resistant behaviour and large minority carrier diffusion length [3, 4]. Since CuInSe$_2$ films can be prepared as both n and p-type semiconductors, they exhibit more potential for formation of its homo and heterojunctions [5]. Moreover, CIS is environmentally benign, stable over a wide range of stoichiometries, possesses good long-term stability and demonstrate stable device performance [6]. The recent results of CIS absorber layer-based solar cells have achieved an efficiency value $\sim 22.8\%$ through improvement in the CIS absorber layer and junction formation process. This value of the solar cell efficiency is comparable and even superior to multi-crystalline Si cells [7, 8]. In order to further increase the photovoltaic efficiency of these solar cells, there is a need for the high structural perfections, phase purity, absence of native oxides and a suitable synthetic method [4]. Moreover, improvements in the conversion efficiency and reliability of CIS absorbers fabricated by different techniques require optimization of the parameters viz. stacking order, Se layer thickness, reaction time of the precursors during annealing and different temperature ramp rate [9]. Moreover, in order to achieve commercial success in CuInSe$_2$ based solar cells, it is necessary that their mass production should be carried out with low cost, eco-friendly and easily scalable processes [6]. Keeping this in mind, the researchers over the globe are working on the synthesis of CIS films by using various physical as well as chemical methods [4]. A variety of fabrication techniques have been used to obtain high-quality CIS films. These fabrication methods include flash evaporation [10], co-evaporation of precursors [11], DC or RF magnetron sputtering [12], spray pyrolysis [13], molecular beam epitaxy (MBE) [14], metal–organic chemical vapour deposition (MOCVD) [15], electro-deposition [16], ion beam sputtering deposition (IBSD) [17] and pulsed laser deposition (PLD) [18], etc. In these techniques, thin film deposition processes

✉ Naresh Padha
nareshpadha@gmail.com

1 Department of Physics, University of Jammu, Jammu, J&K 180006, India

need sophisticated instrumentations and, thus, impose higher cost. The stacked elemental layer deposition (SELD) technique is an alternate method, which is most productive and appropriate for large area production of solar cells [19]. In this, Cu, In and Se layers are deposited sequentially to obtain Cu/In/Se stack. The advantage of SELD technique is its ability to adjust and control the elemental fluxes throughout the film deposition process [19]. Most of the papers report that as-deposited $CuInSe_2$ film by using SELD method is either amorphous or has weak reflection of chalcopyrite $CuInSe_2$, otherwise containing secondary phases of Cu_2Se, In_2Se_3, etc. [20]. One of the major problems encountered is wide difference in the deposition parameters of Cu, In and Se, which result in a non-uniform composition and also show some secondary phases. Several attempts made by many researchers to get rid of the unwanted phases in CIS thin films comprise post-selenization of Cu–In precursor layers at different temperatures under Ar, Se and H_2Se environment in a specially designed vacuum chamber [4, 17]. The use of excessive selenium, highly toxic H_2Se vapours and contamination of another chamber is an issue in this process [17]. In the present research, the toxic H_2Se gas and excess Se consumption involved in the previously reported research have been avoided during the annealing [4, 17]. The Cu/In/Se sequences deposited in vacuum coating unit using SELD method were annealed in tubular furnace in vacuum at different annealing temperatures, the changes in phase evolution of CIS were carefully observed. A single CIS phase has been obtained at lower thickness films at comparatively lower annealing temperatures.

2 Experimental

Copper (Cu), Indium (In) and Selenium (Se) having purity of 99.999%, 99.995% and 99.99%, respectively, were deposited on corning glass substrates at room temperature, as layers in a sequential fashion using a vacuum coating unit (VCU) (Model: 12A4DM; Make: HHV Bangalore, India) at vacuum 2×10^{-6} mbar. The glass substrates used for film deposition were cleaned by dipping into hydrogen peroxide (H_2O_2) solution for 10 min, followed by treatment using trichloroethylene, acetone and methanol (TAM) in a hot ultrasonic bath. The layers of Cu, In and Se were obtained at evaporation rate 1–2 Å/s, 2–3 Å/s and 3–5 Å/s, respectively, during the deposition. The substrate holder was given rotation with the help of rotary motor for the homogeneous deposition of the films. The thicknesses of the films of Cu (12%), In (27%) and Se (61%) were fixed to a value required to meet their atomic ratio of 1:1:2, respectively, and maintaining the stoichiometry for two different thicknesses, (i.e. 775 nm

and 280 nm) by using sequential elemental layer deposition (SELD) technique. The post-deposition annealing of obtained Cu/In/Se stack was carried out in a tubular furnace under vacuum of $\sim 1 \times 10^{-3}$ mbar, respectively, for 1 h at each temperature. The films were annealed at temperatures of 473 K, 523 K, 573 K, 623 K and 673 K. The thickness of as-deposited Cu, In and Se films was established from digital thickness monitor (DTM) attached to VCU (Make: HHV, Bangalore, India; model: DTM 101) using 6 MHz quartz crystal sensor. The post-annealing thicknesses of thin film samples were also measured using Profilometry (Make: Veeco, Model: DekTak 150). The X-ray diffraction (XRD) data of the samples were collected in a line scan mode in 2θ ranges of 10° to 70° with a scan speed of 0.03°/s using filtered $CuK_{\alpha1}$ radiations ($\lambda = 1.5406$ Å) in X-ray diffractometer equipped with HD Bragg Brentano incident geometry (Make: PANalytical; Model: X'pert[3]). The surface morphology was determined from scanning electronic microscope (SEM) (Make: Zeiss, Model SUPRA-55) on acceleration voltage at 20 kV and composition was determined by using an energy-dispersive X-ray analysis (EDAX) attachment (Make: Oxford, Model: 7426) using the K-emission line of copper and L-emission line of selenium and indium, fitted with SEM. The optical data of the samples were obtained using UV–Vis–NIR spectrophotometer (make: Shimadzu, model UV-3600) with a source slit width of 2 nm in the transmission mode, the transmission percentage was measured in the wavelength range of 300 nm to 1800 nm at room temperature. The Raman studies were performed using LabRam Evolution Raman spectrometer (Make: JOBIN YVON Technology, Model: HORIBA Scientific) with laser excitation source of 532 nm in the wavenumber range of 100–300 cm^{-1}. The electrical conductivity of the samples were measured by Vander Pauw method using a Hall measurement setup (Make: BioRad; Model: HL 5200) at room temperature by applying 3.2 kg magnetic field strength and supplying 100 µA current. All analyses of the experimental data were performed by using MicroCal origin software (Make: MicroCal, Model: origin Ver. 8.5).

3 Results and discussion

3.1 Structural characterization

It has been observed from the literature that post-deposition thermal treatment strongly affects the properties of the materials especially for their use in electronic device fabrication. In the present case, Cu/In/Se stacks of two thicknesses viz. 280 nm (sample A) and 775 nm (sample B) having same elemental compositions were obtained by using SELD

71

Fig. 1 a The images of the schematic diagram of Cu/In/Se stack layers taken in thickness proportion and CIS compound formation on annealing at different temperatures and b images of as-deposited Cu/In/Se stack and annealed samples of CIS materials
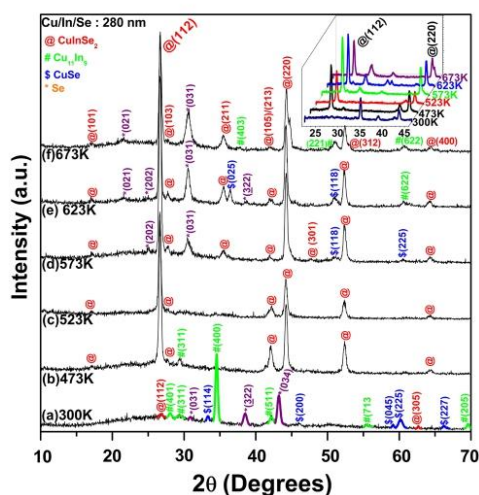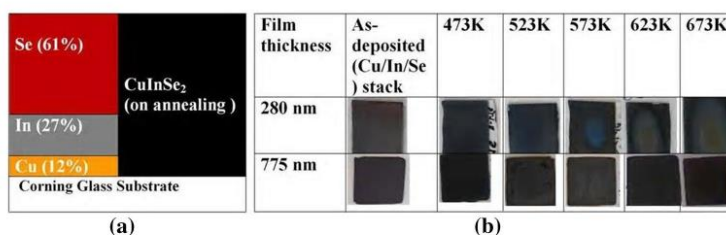

(a)

(b)

Fig. 2 The XRD plot of CuInSe$_2$ thin films for (a) as-deposited Cu/In/Se stacks at 300 K and annealed at (b) 473 K, (c) 523 K, (d) 573 K, (e) 623 K and (f) 673 K.; the magnified 3D views of peaks from 22° to 46° are presented as inset figure

22]. The binary phases of 'Cu$_{11}$In$_9$' and 'CuSe' materials along with low-intensity CIS ternary peak along (112) orientations are observed in the as-deposited stack. The selenium (Se) deposited at the top diffuses through indium layer in the middle and react with copper and form 'CuSe'. Moreover, the 'Cu$_{11}$In$_9$' formation takes place when 'In' layer atoms react with adjoining 'Cu' layer and 'Cu$_{11}$In$_9$' subsequently, transforms to chalcopyrite CuInSe$_2$ on its reaction with 'Se'. The CIS phase of the as-deposited films is observed along (112) oriented planes. The monoclinic 'Cu$_{11}$In$_9$' phase existing in the as-deposited films occupies space group [$C2/m(12)$] as determined on the basis of (401) and (400) planes having most preferred peak along (400) orientations (JCPDS Card No. 41-0883). Moreover, several low-intensity 'CuSe' peaks having orthorhombic crystal system with space group [$Cmcm$ (63)] are also observed at higher '2θ' values corresponding to (200), (045), (225) and (227) oriented planes (JCPDS Card No. 86-1239). Some unreacted 'Se' peaks have also been observed in the as-deposited Cu/In/Se stack (Fig. 2 plot (a)). The diffusion of various constituent materials and their reactions are explained on the basis of a well-recognized thermochemical phenomenon observed in this material as reported by Bhattacharyya et al. [23].

3.2 Effect of annealing temperature

Out of the samples of two different thicknesses obtained on annealing at 473 K, the XRD peaks of 280 nm thick films (sample A) showed better results in terms of their response regarding CIS phases and intensity values of the peaks whereas the 775 nm thick films (sample B) showed four types of phases at all annealing temperatures. However, the variations in the phases of the annealed samples are seen with change in annealing temperature (Fig. 2; Table 2). The 280 nm films were considered for post-deposition thermal treatment at higher temperatures. A strong chalcopyrite

technique. Figure 1a shows the schematic diagram of Cu/In/Se stack and CIS compound formation, the images of the as-deposited stacks and samples obtained at different annealing temperature have been shown in Fig. 1b. The mixed phases were obtained on annealing of the deposited stack at temperatures varying from 473 to 673 K under vacuum $\sim 1 \times 10^{-3}$ mbar. Figure 2 presents the X-ray diffraction patterns of as-deposited Cu/In/Se stack as well as the samples obtained at various annealing temperatures.

The as-deposited stacks and annealed samples were found to possess polycrystalline structure. The results are similar to the already reported work by several authors [21,

CuInSe$_2$ phase emerges at 473 K when 'Se' reacts with 'Cu$_{11}$In$_9$' and 'In' reacts with 'CuSe' due to re-crystallization at this temperature. A single low-intensity 'Cu$_{11}$In$_9$' peak was also observed as secondary phase at 473 K. Further, an increase in the annealing temperature to 523 K provides single CIS phase without any secondary peak. However, re-occurrence of 'Se' peaks is observed at higher annealing temperatures of 573 K and above. Further, the crystallinity of CIS planes increases with increase in annealing temperature due to optimum supply of thermal energy for the samples obtained at re-crystallization temperatures of 573 K and 623 K.

The 'average' grain size (D) of the as-deposited and annealed samples of the films having thicknesses of 280 nm was determined by using Debye–Scherrer relation as per relation given in Eq. 1 as under [17]:

$$D = \frac{0.9\lambda}{\beta \cos\theta} \tag{1}$$

where λ is the wavelength of the X-rays used, β; the full width at half maximum (FWHM) in radians and θ; the Bragg's angle. The 'crystallite size' corresponding to the (112) most preferred peak (MSP) of CuInSe$_2$ increases from 11.41 to 29.34 nm with the increase in annealing temperature from 473 to 623 K; however, reduction in the grain size of the MSP of CIS peak from 29.34 to 23.34 is observed at 673 K (Table 1). The re-occurrence of secondary phases of 'Cu$_{11}$In$_9$', 'CuSe' and 'Se' has been observed at 673 K. The reduction in grain sizes occurring at higher annealing temperature of 673 K is attributed to re-occurrence of secondary phases. The decomposition of CIS phase at higher annealing temperatures may be the reason for these variations. This type of response on annealing of CIS films at higher temperatures has already been reported by several authors [24-27].

The degree of preferred orientation of the samples is determined by the value of R_I defined as the ratio of intensity of MSP to sum of the intensities of all peaks in the XRD pattern represented as under [28].

$$R_I = \frac{I_{(112)}}{\sum_{\text{All peaks}} I_{(hkl)}} \tag{2}$$

where $I_{(hkl)}$ is the intensity of (hkl) peak.

The R_I for (112) set of planes increases from 0.020(2) to 0.588 (1) for 280 nm samples from 473 to 523 K; however, a reduction in the R_I value from 0.523 (1) to 0.432 (1) occured at the annealing temperatures from 573 to 673 K (Table 1). This indicates that the degree of preferred orientation of (112) planes first increases and subsequently decreases with change in the annealing temperature. The results are similar to already reported work on CIS thin films [28-32]. This variation in the degree of preferred orientation in the CIS phase at 573–673 K is attributed to occurrence of various secondary phases as well as variations in CIS planes at higher annealing temperatures.

3.3 Effect of change in layer thickness

The increase in thickness of the Cu/In/Se stack from 280 nm (sample A) to 775 nm (sample B) keeping the ratio of the constituent elements fixed also provides a change in the behaviour of CIS films. The various structural parameters of the as-deposited and annealed samples of 280 nm thick films viz. FWHM (β), grain size (D), degree of preferred orientations (R_I), microstrain (ε), dislocation density (ρ), tetragonal distortion (c/2a) and lattice parameters, etc., have been presented in Table 1. The single chalcopyrite phase CIS is observed at 523 K in 280 nm thick films; however, re-occurrence of secondary phases of 'CuSe' and 'Se' at 573 K and 'Cu$_{11}$In$_9$', 'CuSe' and 'Se' at 623 K and 673 K is observed. The XRD of 280 nm and 775 nm thick samples annealed at 523 K has been presented in Fig. 3. The intensity values in counts per second (cps) as well as grain sizes are higher in 280 nm films than 775 nm samples. The phases present at different annealing temperatures are shown in Table 2; the trend of variations of intensities of samples A and B for (112) planes of CIS are shown in Fig. 4. The reason for this behaviour in 775 nm films may be due to the slow reaction among the constituents and high vapour pressure of 'Se' in higher thickness samples. Moreover, the degree of preferred orientation values of 280 nm films (sample A) were found higher to 775 nm thick films (sample B) at each annealing temperature. The results indicate that better structural response is observed in the films of lower thickness value of 280 nm obtained by using SELD method.

Table 1 The position, FWHM of most preferred orientations and grain sizes of CIS thin film samples having thicknesses 280 nm

Temperature (K)	d spacing (Å)	2θ (°)	Intensity (cps)	(hkl)	FWHM β (°)	Crystallite size D (nm)	RI (112) plane	Microstrain (ε) ($\times 10^{-3}$)	Dislocation density (ρ)$\times 10^{15}$ (lines/m)^2	Tetragonal distortion (C/2a)	Lattice parameters of CIS (Å)
300	3.326(3)[a]	26.78(5)	22	(112)	0.630(5)	14.116(4)	0.020(2)	2.455(5)	90.380(6)	–	–
	2.594(7)[b]	34.54(2)	485	(400)	0.377(3)	25.566(1)		1.355(8)	148.534(4)		
	1.536(4)[c]	60.18(1)	59	(225)	0.645(6)	24.750(0)		1.400(5)	423.622(5)		
	2.092(0)[d]	43.21(1)	204	(034)	0.468(9)	23.249(7)		1.490(9)	228.486(8)		
473	3.342(2)[a]	26.65(2)	950	(112)	0.367(3)	24.204(3)	0.519(1)	1.432(1)	89.521(0)	1.000(3)	a, b=5.787(8), c=11.579(8)
	3.037(5)[b]	29.38(2)	45	(311)	0.416(3)	21.903(8)		1.582(5)	108.378(0)		
523	3.345(9)[a]	26.62(2)	673	(112)	0.314(6)	28.251(5)	0.588(1)	1.226(9)	89.323(3)	1.001(1)	a, b=5.792(7), c=11.598(4)
573	3.342(2)[a]	26.65(1)	1275	(112)	0.306(9)	28.967(9)	0.523(1)	1.196(6)	89.521(0)	1.000(4)	a, b=5.787(8), c=11.580(8)
	2.925(7)[d]	30.53(6)	94	(031)	0.627(1)	14.710(0)		2.356(4)	116.823(0)		
623	3.343(4)[a]	26.64(7)	1135	(112)	0.303(0)	29.338(2)	0.433(1)	1.181(5)	89.455(1)	0.998(7)	a, b=5.791(9), c=11.569(7)
	2.923(8)[d]	30.55(6)	210	(031)	0.483(9)	19.067(0)		1.817(9)	116.972(4)		
673	3.338(5)[a]	26.68(4)	756	(112)	0.380(9)	23.346(2)	0.432(1)	1.484(7)	89.719(1)	1.002(2)	a, b=5.785(0), c=11.595(8)
	1.787(9)[b]	51.04(5)	50	(221)	0.718(2)	17.595(2)		1.970(0)	312.812(6)		
	4.125(9)[d]	21.52(4)	20	(021)	0.778(4)	10.972(7)		3.159(0)	58.741(8)		

[a]CuInSe2
[b]Cu11In9
[c]CuSe
[d]Se

74
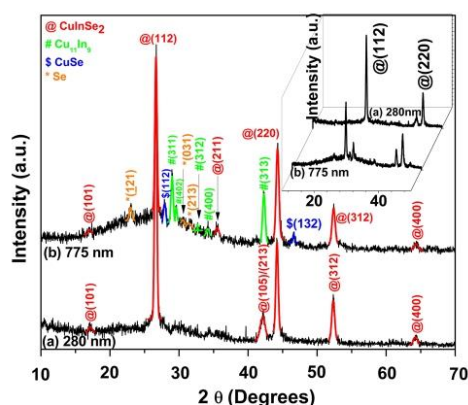
Fig. 3 The XRD plot of CuInSe$_2$ thin film samples A (280 nm) and B (775 nm) obtained at annealing temperatures of 523 K; the magnified 3D views of peaks from 10° to 50° are presented as inset figure
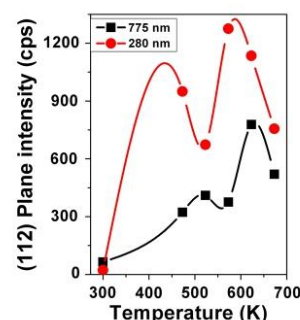

Fig. 4 The intensity variation of MSP of CIS (112) peak at different annealing temperatures for 280-nm and 775-nm-thick films

3.4 Raman study

The Raman spectra measured at 532 nm excitation wavelength for the as-deposited and annealed samples having thicknesses of 280 nm (sample A) and 775 nm (sample B) have been shown in Fig. 5a, b. The samples show A$_1$ mode approximately at 253 cm^{-1} and 252 cm^{-1}, respectively, corresponding to monoclinic crystal (m-Se) with Se$_8$ monomer rings due presence of selenium at top layer in the as-deposited Cu/In/Se stacks at 300 K [33]. The main peak at 173 cm^{-1} obtained at annealing temperature of 473 K in the samples A & B corresponds to A$_1$ mode in CuInSe$_2$ chalcopyrite phase [34]. Moreover, weak peaks at 183 cm^{-1},

213 cm^{-1} and 230 cm^{-1} detected in the spectra of 473 K annealed samples of CuInSe$_2$, are also in good agreement with the single-phase mode of chalcopyrite structures of CIS [35]. The annealed films also exhibit weak peaks at 114 cm^{-1} at 573 K in 280 nm thick samples due to presence of m-Se which may assist in the formation of binary phase with available copper (Cu), so mixed phase chalcopyrite structures of CIS is possible with 'CuSe' and 'Se' phases at higher annealing temperatures. The strong peak at 173 cm^{-1} was found along with an additional broad shoulder peak at 183 cm^{-1} at 473 K and 523 K. This shoulder peak at 183 cm^{-1} indicates the formation of poor crystal quality of CuInSe$_2$ at lower annealing temperatures of 473 K and 523 K. The increase in annealing temperature to 573 K, 623 K and 673 K leads to elimination of the broad shoulder attached with 173 cm^{-1} peak and enhances the crystalline ordering that correlates with the already reported results of

Table 2 The variation in phases present in the samples with change in the annealing temperatures

Temperature (K)	Film thickness (280 nm)	Film thickness (775 nm)
As-deposited @ 300 K	CuInSe$_2$, Cu$_{11}$In$_9$, CuSe, Se	CuInSe$_2$, Cu$_{11}$In$_9$, CuSe, Se
CIS@473 K	CuInSe$_2$, Cu$_{11}$In$_9$	CuInSe$_2$, Cu$_{11}$In$_9$, CuSe, Se
CIS@523 K	CuInSe$_2$	CuInSe$_2$, Cu$_{11}$In$_9$, CuSe, Se
CIS@573 K	CuInSe$_2$, CuSe, Se	CuInSe$_2$, Cu$_{11}$In$_9$, CuSe, Se
CIS@623 K	CuInSe$_2$, Cu$_{11}$In$_9$, CuSe, Se	CuInSe$_2$, Cu$_{11}$In$_9$, CuSe, Se
CIS@673 K	CuInSe$_2$, Cu$_{11}$In$_9$, CuSe, Se	CuInSe$_2$, Cu$_{11}$In$_9$, CuSe, Se
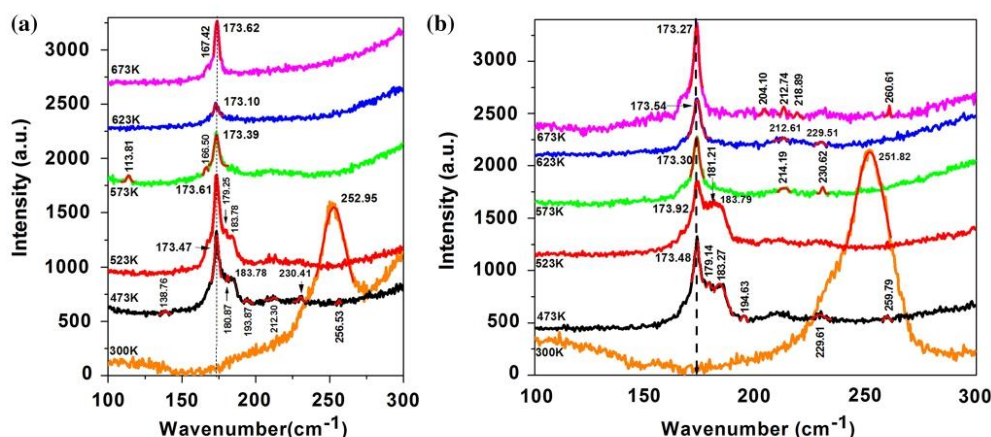
Fig. 5 The typical Raman spectra of as-deposited and annealed samples of CuInSe$_2$ having thicknesses **a** 280 nm and **b** 775 nm

XRD measurements [36]. Moreover, high intensity values of Raman peaks in the 280 nm and 775 nm samples indicate good surface morphology and phase composition of the CIS films. The Raman spectra of CIS films obtained at annealing temperatures from 473 to 673 K also show negligible shift in A$_1$ values which indicate low stress level in the CIS films. The higher thickness films (775 nm) indicate the existence of some low-intensity secondary peaks at 673 K along with main A$_1$ mode peak. The changes are attributed to the re-occurrence of some secondary phases.

3.5 Morphological and compositional analysis

The surface morphology of chalcopyrite CuInSe$_2$ thin films has been determined by scanning electron microscopy (SEM). Figure 6a–d shows 2D scanning electron microscopic images of as-deposited Cu/In/Se stack as well as the films obtained on annealing at 523 K, 573 K and 623 K, respectively, each having thickness of 280 nm and (e)–(h) represent corresponding images of 775 nm thick films. The 280 nm thick as-deposited samples are seen to represent mixture of different sized grains of spherical shapes. However, the 775 nm thick films represent clusters of identical spheres. Both type of films show voids, the magnitude of the voids is higher in 280 nm films. In contrast to this, the 523 K annealed samples show uniformly distributed nano-rod shaped structures of CIS crystallites in the 280 nm (sample A) films. These are well-defined grains which are uniformly distributed over the entire surface whereas 775 nm (sample B) films possess seed-like shapes along with some irregular lumps. The 280 nm films transform to thicker nano-rods along with bulky and irregular-shaped grains at 573 K. Similar composition is also seen at this annealing temperature in 775 nm thick films. Moreover, the decomposition of the CIS grains is clearly seen in 280 nm thick films at 623 K which causes re-occurrence of some secondary phases. Similar response is also observed in the 775 nm samples at 623 K.

The atomic percentage of elements present in the samples was calculated from energy dispersive X-ray analysis (EDAX) data for annealed samples of CIS having thickness ~280 nm and 775 nm. The EDAX spectra of 523 K annealed samples of both thicknesses have been shown in Fig. 7a, b.
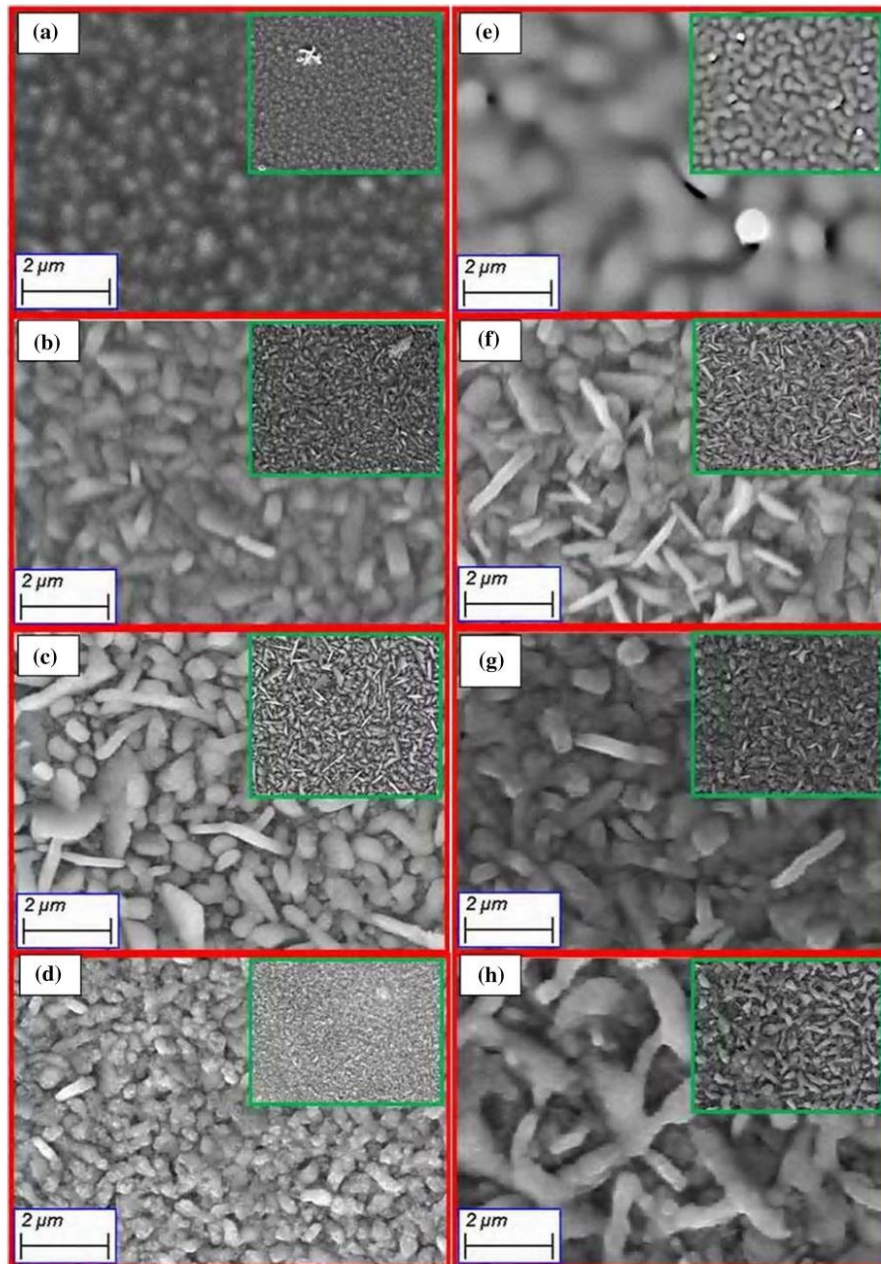
Fig. 6 **a–d** Shows 2D scanning electron images of annealed CIS thin film of 280 nm and **e–h** 775 nm thicknesses, obtained at 300 K, 523 K, 573 K and 623 K, respectively.

77
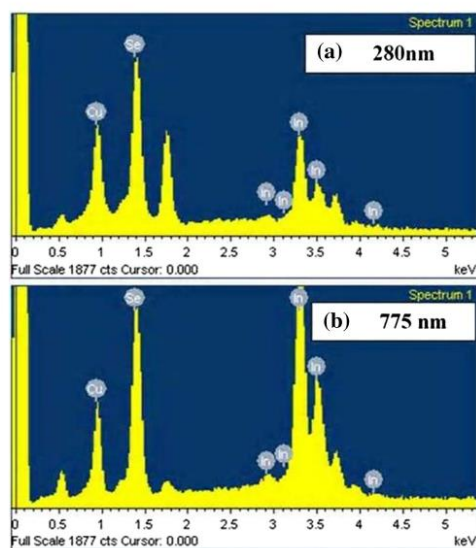
Fig. 7 a, **b** Shows EDAX spectra at 523 K annealed CIS samples having thicknesses of 280 nm and 775 nm

The corresponding values are mentioned in the Table 3. It is observed from the table that the elemental composition of Cu:In:Se elements tends to meet their stoichiometric ratios

of 1:1:2 at 523 K. Nevertheless, both samples are seen to get deviated with further increase in the annealing temperature. Moreover, 775 nm thin films are seen more deviated from the stoichiometric values in comparison with 280 nm thick samples.

3.6 Optical studies

The electronic transition in the material can be monitored by studying energy band transition which can be possible through transmission and absorption spectroscopy [19]. The absorption co-efficient values were calculated from the transmission spectra by using the relation as given below [37].

$$\alpha = \frac{1}{t} \ln\left(\frac{100}{T\%}\right) \tag{3}$$

where α is the absorption co-efficient; $T\%$; the optical transmission percentage and t; the thickness of the films. The optical band gap values were established by using Tauc's relation given in equation [37].

$$\alpha h\nu = A(h\nu - E_g)^n \tag{4}$$

where A is a constant, ν; the photon frequency and h; the plank constant and the optical energy band gap (E_g) and n; number. The value of $n = 1/2$ is used for allowed direct transition, and $n = 2$ is used for allowed indirect transition for band gap materials [37]. Figure 8a, b shows the $(\alpha h\nu)^2$ versus energy ($h\nu$) plots of the samples of CIS obtained at annealing temperatures of 473 K to 673 K. The insets of Fig. 8a, b

Table 3 The EDAX analysis of CIS thin films of 280 nm and 775 nm annealed at different temperature

Thicknesses	Temperature (K)	Atomic %			Cu/In	Cu/Se	(Cu+In)/Se	Material composition
		Cu	Se	In				
280 nm	300	16.70	68.10	15.19	1.099(4)	0.245(2)	0.468(2)	$CuIn_{0.91}Se_{4.08}$
	523	29.26	46.04	24.71	1.184(1)	0.635(5)	1.172(2)	$CuIn_{0.84}Se_{1.57}$
	573	30.09	44.03	25.88	1.162(6)	0.683(3)	1.271(1)	$CuIn_{0.86}Se_{1.46}$
	623	31.95	47.42	20.63	1.548(7)	0.673(7)	1.108(8)	$CuIn_{0.65}Se_{1.48}$
775 nm	300	03.26	90.02	06.71	0.485(8)	0.036(2)	0.110(7)	$CuIn_{2.06}Se_{27.61}$
	523	25.61	39.93	37.28	0.686(9)	0.641(3)	1.575(0)	$CuIn_{1.46}Se_{1.56}$
	573	29.54	33.19	37.28	0.792(3)	0.890(0)	2.013(2)	$CuIn_{1.26}Se_{1.12}$
	623	29.93	38.72	31.36	0.954(4)	0.772(9)	1.582(9)	$CuIn_{1.05}Se_{1.29}$

78

Fig. 8 a, b Shows the $(\alpha h\nu)^2$ versus $(h\nu)$ plot of annealed CuInSe$_2$ samples of thin films
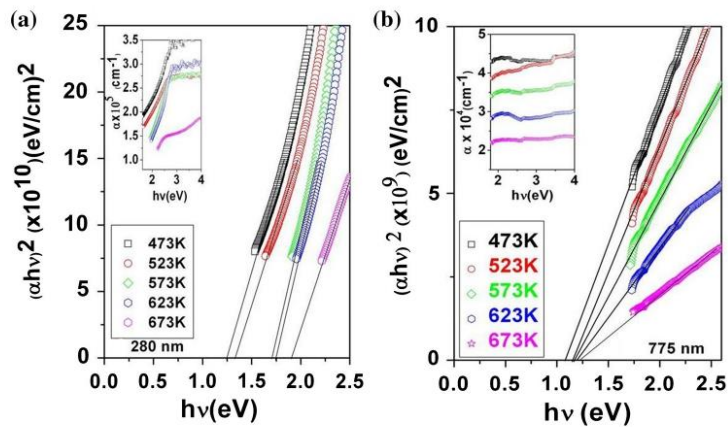
Table 4 The band gap (E_g), absorption co-efficient (α) and critical wavelength (λ_C) values of CuInSe$_2$ thin films having thickness of (a) 280 nm and (b) 775 nm

Film thickness	Temperature (K)	Band gap (E_g) (eV)	Critical wavelength (λ_C) (nm)	Absorption co-efficient (α) ($\times 10^5$) (cm^{-1})
(a) 280 nm	473	1.25	992	2.00
	523	1.33	932	1.75
	573	1.71	725	1.40
	623	1.75	708	1.40
	673	1.90	652	1.20
(b) 775 nm	473	1.09	1138	0.40
	523	1.15	1078	0.36
	573	1.16	1068	0.30
	623	1.20	1033	0.25
	673	1.22	1016	0.22

show the absorption co-efficient (α) versus energy ($h\nu$) plots corresponding to samples A and B. The calculated values of optical band gap (E_g), absorption co-efficient (α), and critical wavelength (λ_C) of the annealed samples of 280 nm and 775 nm thick films have been presented in the Table 4. The absorption co-efficient (α) values for 280 nm thick samples are found higher than the 775 nm thick samples by one order at each annealing temperature. The values of α are much higher than the multi-crystalline Si films of several μm thickness [7, 8]. The linear nature of the plots through the absorption edge indicates CuInSe$_2$ material to possess direct band gap (E_g). The band gap values of CIS thin films were found to vary from 1.09 to 1.22 eV in case of 775 nm thick films whereas the band gap varied from 1.25 to 1.90 eV for 280 nm thick films. It is observed that direct band gap (E_g) values for 280 nm thick films are higher than the reported E_g value of CIS films [17]; moreover, the E_g value increases with the increase in annealing temperature from 473 to 673 K in both samples. The higher values of absorption co-efficient (α; 1 x 10^5 to 3.5 x 10^5 cm^{-1}) are obtained for annealed films of 280 nm. The critical wavelength (λ_C) value observed for direct transition varies from 992 nm to
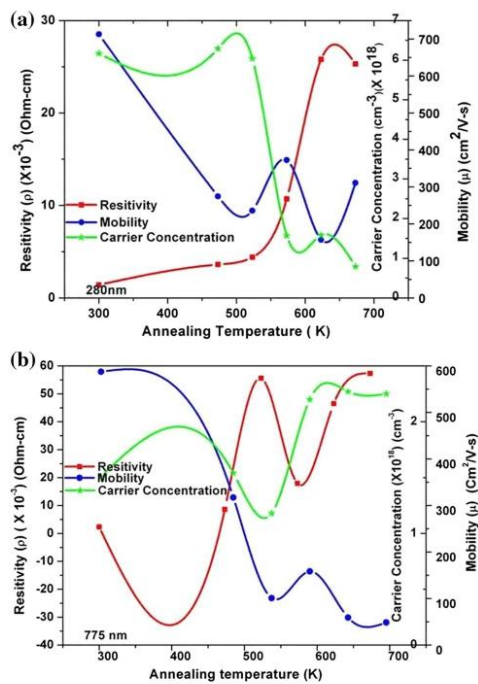
Fig. 9 a, b Shows the trends of variations of resistivity (ρ), mobility (μ) and carrier concentration (N_A) values of the CIS films at different temperatures

652 nm for the annealed CIS samples of 280 nm thickness. Thus, obtained CIS thin films of 280 nm are more suitable as absorber layers in solar cell fabrication which can absorb the photons from visible to NIR region of e.m. spectrum.

3.7 Electrical characterization

The electrical properties of 280 nm and 775 nm thick CIS samples obtained on annealing temperatures varying from 473 to 673 K were studied by van der Pauw method using a Hall measurement setup (Make: BioRad; Model: HL 5200) [38]. The plots for the variations of resistivity (ρ), mobility (μ) and carrier concentration (N_A) values with annealing temperatures have been shown in Fig. 9a, b. The correlation between the composition and conductivity type of the thin films of CIS have been reported by several authors which provides that Se > 50% and Cu/In > 1 shows p-type behaviour [39]. Moreover, the *p*-type behaviour is attributed to 'Cu' on 'In' sites and/or 'In' vacancies along with interstitial 'Se' [39]. The undertaken annealed samples of both thicknesses indicate *p*-type conductivity. The resistivity for 523 K annealed 280 nm thick samples show 4.39×10^{-3} Ω cm value whereas this value increases to 5.56×10^{-2} Ω cm for 775 nm thick films at this annealing temperature due to presence of secondary phases. Further, the resistivity values increase with further increase in the annealing temperatures in both samples. The mobility (μ) and carrier concentration (N_A) values over the undertaken annealing temperature range are higher in 280 nm films as compared to 775 nm films (Table 5). The resistivity values are low and mobility values are high in the 523 K

Table 5 The resistivity (ρ), mobility (μ) and carrier concentration (N_A) values for 280-nm and 775-nm-thick films obtained at different annealing temperatures

Film thickness	280 nm			775 nm		
Temperature (K)	Resistivity (ρ) (Ω cm)	Mobility (μ) (cm^2/Vs)	Carrier concentration (N_A)(cm^{-3})	Resistivity (ρ) (Ω cm)	Mobility (μ) (cm^2/Vs)	Carrier concentration (N_A) (cm^{-3})
473	3.61×10^{-3}	274.6	6.29×10^{18}	8.6×10^{-3}	317.4	1.54×10^{18}
523	4.39×10^{-3}	235.6	6.04×10^{18}	5.56×10^{-2}	100.9	1.18×10^{18}
573	1.07×10^{-2}	372.4	1.57×10^{18}	1.79×10^{-2}	158.3	2.20×10^{18}
623	2.58×10^{-2}	157.2	1.58×10^{18}	4.65×10^{-2}	59.2	2.27×10^{18}
673	2.53×10^{-2}	310.9	7.9×10^{17}	5.73×10^{-2}	48.5	2.25×10^{18}

and 573 K annealed samples (280 nm thick). These parameters of CuInSe$_2$ thin films are sensitive to the change in the thickness as well as the composition variation of Cu/In in the CIS films.

4 Conclusion

In the undertaken research, CIS films have been successfully obtained by a low-cost sequential elemental layer deposition (SELD) technique. The use of highly toxic H$_2$Se vapours, consumption of additional selenium (Se) as well as the contamination due to the use of another vacuum chamber during the annealing process has been avoided. Moreover, single-phase CIS was achieved in lower thickness films at comparatively lower annealing temperature. The films showed high absorption co-efficient (α) and suitable band gaps (E_g) corresponding to visible to NIR region of e.m. spectrum. The electrical investigations of the 280 nm films show low electrical resistivity (ρ), high mobility (μ) and high carrier concentration (N_A). Thus, high-quality CIS material films have been achieved which are found a more suitable alternate for photovoltaic absorber layer application.

References

1. K. Puech, S. Zott, K. Leo, M. Ruckh, H.W. Schock, Appl. Phys. Lett. **69**, 3375 (1996)
2. E. Tzvetkova, N. Stratieva, M. Ganchev, I. Tomov, K. Ivanova, K. Kochev, Thin Solid Films **311**, 101 (1997)
3. L. Kaupmees, M. Altosaar, O. Volubujeva, E. Mellikov, Thin Solid Films **515**, 5891 (2007)
4. T.P. Gujar, V.R. Shinde, P.J. Won, L.H. Kyung, J.K. Deog, J.O. Shim, J. Electrochem. Soc. **156**, E8 (2009)
5. K.L. Chopra, S.R. Das, *Thin Film Solar Cells* (Plenum Press, New York, 1983)
6. H. Abdullah, S. Habibi, Int. J. Photoenergy **2013**, 568904 (2013)
7. J. Gifford, Solar frontier hits 22.3% on CIGS Cell. Ind Suppliers Mark Trends 2015.
8. R. Kamada, T. Yagioka, S. Adachi, A. Handa, K.F. Tai, T. Kato, and H. Sugimoto, in IEEE Xplore Digital Library (2016)
9. J. Koo, S. Kim, T. Cheon, S.H. Kim, W.K. Kim, Sci. Rep. **8**, 3905 (2018)
10. A.A.S. Akl, A. Ashour, A.A. Ramadan, K. Abd El-Hady, Vacuum **61**, 75 (2001)
11. O. Volobujeva, M. Altosaar, J. Raudoja, E. Mellikov, M. Grossberg, L. Kaupmees, P. Barvinschi, Sol. Energy Mater. Sol. Cells **93**, 11 (2009)
12. A. Ihlal, K. Bouabid, D. Soubane, M. Nya, O. Ait-Taleb-Ali, Y. Amira, A. Outzourhit, G. Nouet, Thin Solid Films **515**, 5852 (2007)
13. B.J. Egaas, B.S. Velumani, J. Mater. Sci. Mater. Electron. **29**, 15369 (2018)
14. F.R. Whitem, A.H. Clark, M.C. Graf, J. Appl. Phys. **50**, 544 (1979)
15. S.H. Yoon, K.W. Seo, S.S. Lee, W. Shim, Thin Solid Films **515**, 1544 (2006)
16. M.E. Calixto, P.J. Sebastian, R.N. Bhattacharya, R. Noufi, Sol. Energy Mater. Sol. Cells **59**, 75 (1999)
17. P. Fan, G.X. Liang, Z.H. Zheng, X.M. Cai, D.P. Zhang, J. Mater. Sci. Mater. El. **21**, 897 (2010)
18. P.F. Luo, C.F. Zhu, G.S. Jiang, Solid State Commun. **146**, 57 (2008)
19. M.C. Sharma, B. Tripathi, S. Kumar, S. Srivastava, Y.K. Vijay, Mater. Chem. Phys. **131**, 600 (2012)
20. V. Sachan, J.D. Meakin, Sol. Energy Mater. Sol. Cells **30**, 147–160 (1993)
21. A. Bouraiou, M.S. Aida, E. Tomasella, N. Attaf, J. Mater. Sci. **44**, 1241 (2009)
22. S. Vankatachalam, D. Mangalaraj, S.K. Narayandass, K. Kim, Phys. B **358**, 27 (2005)
23. D. Bhattacharyya, I. Forbes, F.D. Adurodija, M.J. Carter, J. Mater. Sci. **32**, 1889 (1997)
24. S. Verma, N. Orbey, R.W. Birkmire, T.W.F. Russell, Progr. Photovoltaics **4**, 341 (1996)
25. A. Gupta, S. Isomura, Sol. Energy Mater. Sol. Cells **53**, 385 (1998)
26. M.E. Calixto, P.J. Sebastian, J. Mater. Sci. **33**, 339 (1998)
27. C. Guillen, J. Herrero, Sol. Energy Mater. Sol. Cells **73**, 143 (2002)
28. J. Müller, J. Nowoczin, H. Schmitt, Thin Solid Films **496**, 364 (2006)
29. A. Bouraiou, M.S. Aida, E. Tomasella, N. Attaf, J. Mater. Sci. Mater. Electron. **44**(5), 1241 (2009)
30. A. Ashour, J. Mater. Sci. Mater. Electron. **17**, 625 (2006)
31. S.P. Nehra, D. Sharma, M. Singh, Y.K. Vijay, J. Alloys Compd. **502**, 220 (2010)
32. A. Bouraiou, M.S. Aida, A. Mosbah, N. Attaf, Braz. J. Phys. **39**(3), 543 (2009)
33. A.H. Goldan, C. Li, S.J. Pennycook, J. Schneider, A. Blom, W. Zhao, J. Appl. Phys. **120**, 135101 (2016)
34. A.M. Xu, X.L. Xu, J. Xu, X.J. Yang, J. Zuo, N. Kong, W.H. Huang, H.T. Liu, Semicond. Sci. Technol. **19**, 1201 (2004)
35. A. Rincon, F.J. Ramirez, J. Appl. Phys. **72**(9), 4321–4324 (1992)
36. E.P. Zaretskaya, V.F. Gremenok, V. Riede, W. Schmit, K. Bente, V.B. Zalesski, O.V. Ermakov, J. Phys. Chem. Solids **64**, 1989–1983 (2003)
37. J. Tauc, R. Grigorovici, A. Vancu, Phys. Status Solidi B **15**, 627 (1966)
38. K.A. Borup, E.S. Toberer, L.D. Zoltan, G. Nakatsukasa, M. Errico, J.-P. Fleurial, B.B. Iversen, G. Snyder, Rev. Sci. Instrum. **83**, 122 (2012)
39. T. Yamaguchi, J. Matsufusa, A. Yoshida, Sol. Energy Mater. Sol. Cell **27**, 27 (1992)

Publication 4th

Contents lists available at ScienceDirect

Materials Chemistry and Physics

journal homepage: www.elsevier.com/locate/matchemphys
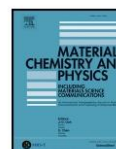
Growth of γ- In$_2$Se$_3$ monolayer from multifaceted In$_x$Se$_y$ thin films via annealing and study of its physical properties

Rajesh Niranjan , Naresh Padha [*]

Department of Physics, University of Jammu, Jammu, 180006, J&K, India

- Thin films of γ-In$_2$Se$_3$ were grown on annealing of SELD grown In/Se stacks.
- A low cost and less toxic processing of γ-In$_2$Se$_3$ buffer layers for PV solar cells.
- Study of the dynamics of changing phases of In$_x$Se$_y$ films on annealing.
- Growth of In$_2$Se$_3$ thin films as a candidate to replace CdS in solar cells.

GRAPHICAL ABSTRACT
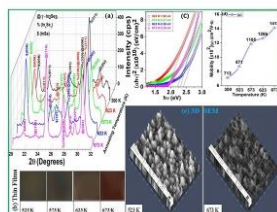
ABSTRACT

The dynamics of changing phases of In$_x$Se$_y$ thin film alloy grown on annealing of the SELD films were analyzed. The thin film samples provide mixed phases of γ-In$_2$Se$_3$, In$_4$Se$_3$, and InSe at the annealing temperatures of 523 K to 623 K and attain a single phase at 673 K. The presence of strong γ-In$_2$Se$_3$ phase at 673 K was supported by the vibrational spectra. The films are homogeneous throughout, without cracks well cover the entire glass substrate. The crystallites are densely packed, irregular shaped, and complex structured. The bandgap (E$_g$) varies from 1.92 eV to 2.39 eV; refractive index (n) from 2.75 to 2.55 while the absorption coefficient (α) values limit within 2 × 10^4 to 1.5 × 10^5 cm^{-1}. This mobility (μ) of the films increases from 871 to 1413 cm^2/V-s with changing temperature, the change is attributed to the growth of γ-In$_2$Se$_3$ crystallites. The bandgap tuning, high absorption coefficient, and mobility values exhibited by the films make these suitable for use as buffer layers in the solar cell structure. The undertaken In$_2$Se$_3$ semiconductor, among many other applications, is a candidate to replace CdS in solar cells.

1. Introduction

Indium selenide (In$_2$Se$_3$) is a compound semiconductor material that belongs to the A$_2^{III}$B$_3^{VI}$ family. It crystallizes as double layers of Se–In–Se–In–Se atoms stacked through the Se along the c-axis [1]. The material possesses a direct bandgap and shows enormous potential in

photovoltaic and optoelectronic devices [2,3]. The In$_2$Se$_3$ films have been studied as a precursor to CuInSe$_2$ for solar cells [4,5], as an optical recording medium [6,7], sensors of linearly polarized radiation [8], broadband converters of optical radiation [9] and in some nano-electronic devices viz. Schottky diodes, photo-detectors, phase change memory devices, and photoelectrochemical cells [10–13]. The
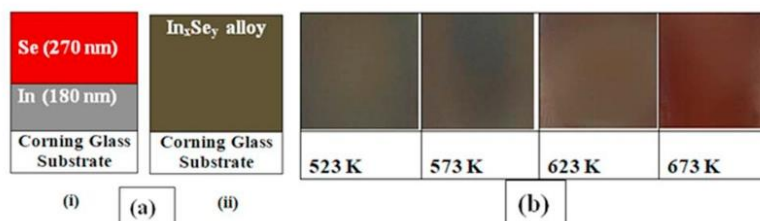
Fig. 1. a-b show the schematic diagram of In/Se stack and images of the In_xSe_y thin films obtained at different annealing temperatures.

films are also useful in lithium current sources and for the production of photodetectors operating in the visible region of E.M. Spectrum with negative photoconductivity [14,15]. The phase diagram for III-VI binary compounds is complex and the sizes of their unit cells are large. The complexity of the phase diagram originates as there are many energetic ways in which the trivalent and divalent atoms combine to satisfy the bonding requirements. In indium selenide thin films, a variety of In–Se phases may be formed depending upon the deposition method and growth parameters [16,17]. The In_2Se_3 is one of the most extensively studied binary chalcogenide alloy that crystallizes in a well-known hexagonal layered structure (α -phase), rhombohedral structure (β -phase), defect wurtzite structures (γ, δ -phase), and anisotropic structure (κ-phase) [2,3,18–24]. The multiphase existence of this compound affects its use in photovoltaic devices since each phase has specific physical and chemical properties [15,16]. Therefore, there is a need for structural perfection, phase purity, and the absence of native oxides to improve the photovoltaic activity of the grown films. The γ-In_2Se_3 material and thin films have attracted the attention of the world community due to applications in electronic devices [2,10,17,20,25]. The γ- In_2Se_3 presents a bandgap of 1.8 eV [26] which is suitable for the buffer layer in CIS solar cells [27,28]. This buffer layer is preferred to CdS because it offers the possibility of continuous deposition of the ZnO/In_2Se_3/CIS solar cell structure without breaking vacuum, thus, reducing contamination [29]. The γ- In_2Se_3/p-Si heterojunction as a visible spectra photodetector have been reported with remarkable responsivity and detectivity over a wide range of wavelengths in this region [30]. Several methods have been employed for the preparation of In_2Se_3 thin films which include thermal evaporation [14,31], co-evaporation [5,19,20, 32], spray pyrolysis [13,33], sol-gel techniques [34], chemical bath deposition (CBD) [35], metal-organic chemical vapor deposition (MOCVD) [36], van der Waals epitaxy [37], radio frequency (rf) magnetron sputtering [4,29,[38]], molecular beam epitaxy (MBE) [39], chemical vapor transport (CVT) [2,3,40], potential pulse atomic layer deposition (PP-ALD) [41], flash evaporation [42] and pulsed laser deposition (PLD) [31]. An attempt has also been made to obtain γ- In_2Se_3 layers by solid-state reaction of the constituent elements on annealing under the selenium atmosphere [26]. An alternate method has been evoked for the preparation of γ- In_2Se_3 thin films through annealing of the deposited In/Se stack. The stacks used for the annealing were obtained by thermally deposited indium followed by the deposition of selenium by chemical bath deposition (CBD) [43]. Moreover, several types of research have reported on polycrystalline In_xSe_y thin-film alloys intending to have mass production of these materials at low cost by using eco-friendly methods [44–47]. The stacked elemental layer deposition (SELD) is the most appropriate method for the large area production of In_2Se_3 thin films due to low cost and easy processing. Moreover, SELD imparts better crystallinity and provide a smoother surface to the deposited films [47]. This technique provides solar cell structures with high efficiency and better stability [48]. The main advantage of the SELD technique is its ability to adjust and control the elemental fluxes throughout the film deposition process [49].

In the undertaken research, the SELD technique was used for the

growth of In/Se stacks. The obtained stacks were used for the development of In_xSe_y films via annealing under vacuum. An effort has been made to obtain single-phase γ-In_2Se_3 thin films from multi-faceted In_xSe_y alloy. The use of additional selenium and highly toxic H_2Se gases environment was avoided in the present method. The dynamics of changing phases of In_xSe_y thin films with annealing have been analyzed. We also report the structural, morphological, compositional, optical, and electrical characteristics of the In_xSe_y thin films as obtained at different annealing temperatures.

2. Experimental

γ-In_2Se_3 was prepared by the two-stage process. Stage one involved deposition of elemental indium (In; 99.995% pure) and selenium (Se; 99.99% pure) in a sequential fashion on the corning glass substrate at room temperature. It was followed by annealing of In/Se stacked layers at a temperature varying from 523 K to 673 K. The deposition was performed by thermal evaporation method in a vacuum coating unit (Make: HHV, India; Model: 12A4DM) at vacuum ~ 2 × 10^{-6} mbar whereas annealing of In/Se stacks was performed in an indigenous tubular furnace at vacuum ~ 1 × 10^{-3} mbar. Corning glass slides were used as a substrate for the film deposition and were cleaned by dipping into hydrogen peroxide (H_2O_2) solution for 10 min followed by their treatment in trichloroethylene, acetone, and methanol (TAM treatment) in an ultrasonic bath. The thermal evaporation rates of In and Se to the values of 2–3 Å/s and 3–5 Å/s, respectively were maintained, and corresponding film thicknesses of 180 nm and 270 nm were obtained to achieve the In/Se atomic ratio ~0.66. The annealing of In/Se stacks at the temperatures of 523 K, 573 K, 623 K, and 673 K was performed for 1 hour at each temperature. The substrate holder was rotated with uniform speed during depositions to achieve a homogeneous thickness of the deposited films. The in-situ film thickness during deposition was measured by using the quartz crystal sensor of 6 MHz frequency (Make: HHV, India; Model: DTM-101). The thickness of the as-deposited and annealed samples was also measured by surface profiler (Make: Veeco; Model: DekTak-150). The as-grown stack and films obtained on annealing at different temperatures were undertaken for different characterizations. The structural analysis was performed by X-ray diffraction (XRD) data obtained inline mode using Ni filtered CuKα$_1$ (λ = 1.5406 Å) radiations at 40 kV and 45 mA (Make: PANalytical; Model: X'pert^3). The XRD patterns were recorded in the '2θ 'range of $10°-60°$ with a scan speed of $0.03°$/s. The surface morphology of the as-deposited and annealed In_xSe_y thin films were analyzed by using a scanning electron microscope (Make: ZEISS; Model: SUPRA-55) operated with acceleration voltage up to 20 kV and magnification up to 20 000 X. Composition analysis was carried out by energy–dispersive X-ray analysis (EDAX) attachment of SEM (Make: Oxford; Model: 7426) using L-emission line of indium and selenium. Optical properties of the thin film samples were accomplished using transmission spectra recorded from UV–Vis–NIR spectrophotometer (Make: Shimadzu; Model UV-3600) with a 2 nm source slit. Vibrational spectra were recorded in a confocal Raman system (Make: JOBIN YVON, Model: HORIBA) with a
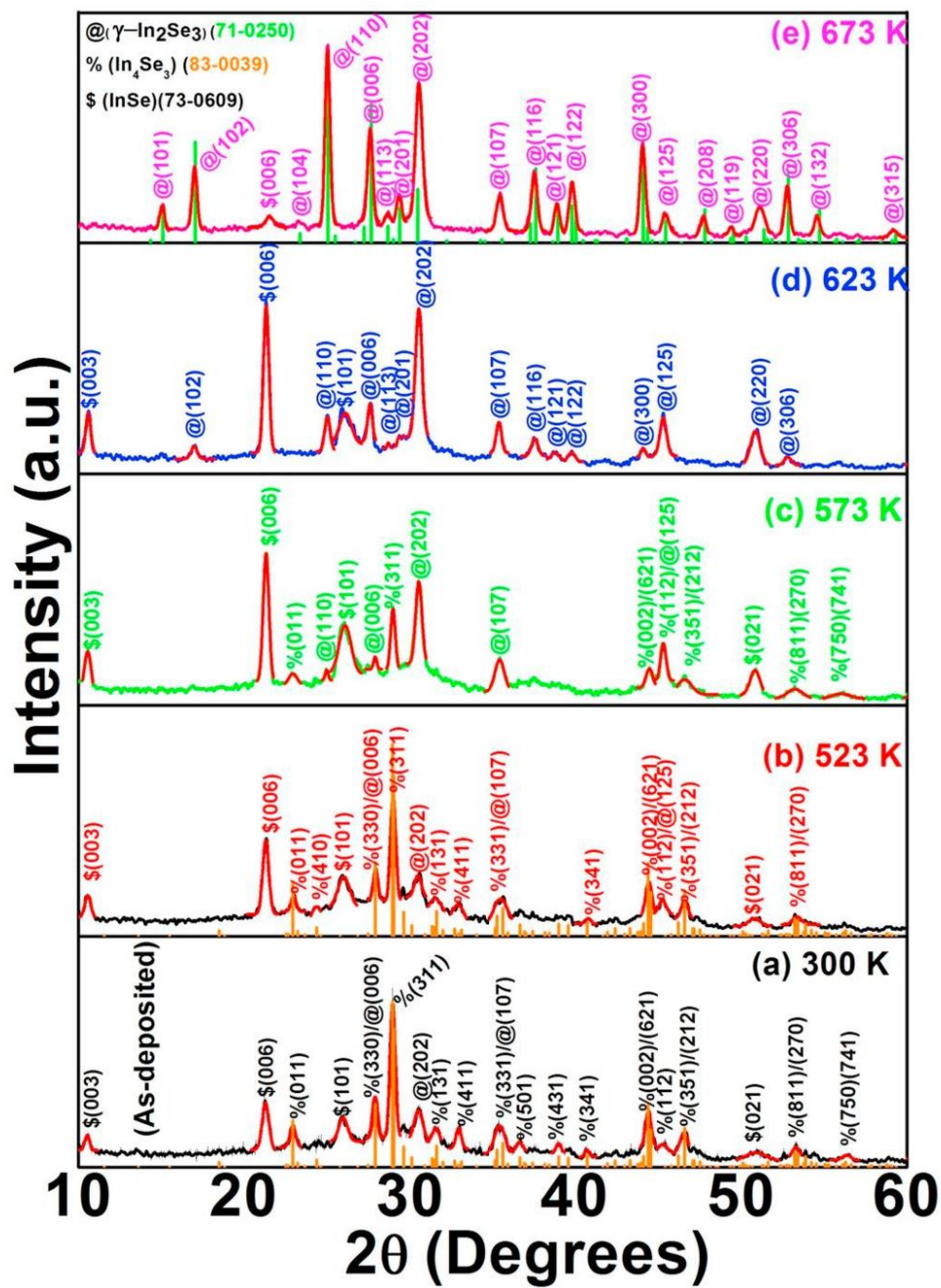
2

Fig. 2. a-e shows the X-ray diffraction (XRD) patterns of as-grown In/Se stack and thin films of In_xSe_y obtained at the annealing temperatures of 523 K, 573 K, 623 K, and 673 K.
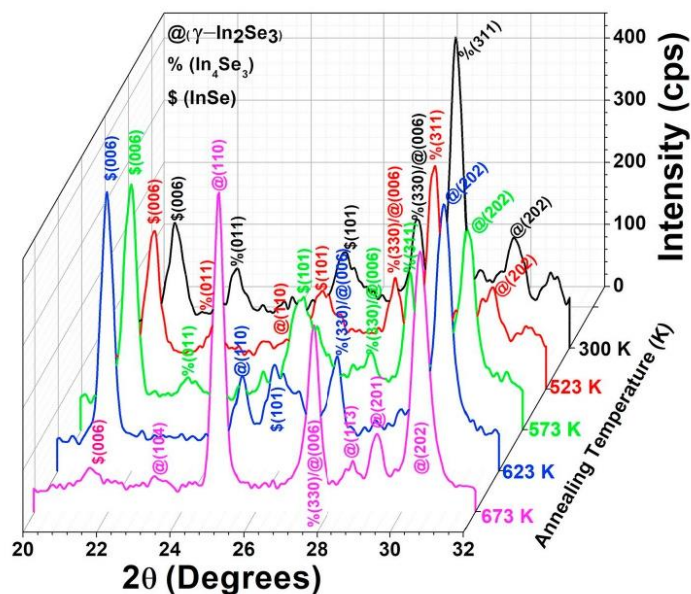
3

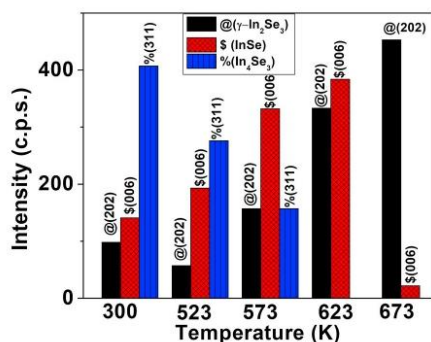**Fig. 3.** shows magnified views of 3D plots of the XRD data obtained in the '2θ' range from 20° to 32°

Fig. 4. shows bar chart representations of the phases present in the films and intensity variations of corresponding MSPs at different annealing temperatures.

532 nm laser. The data were recorded in the wavenumber range 100–300 cm^{-1}. Electrical parameters of the thin films were determined by the van der Pauw method using hall measurement setup (Make: BioRad; Model: HL-5200) at room temperature using 4-lead geometry in a 3.2 KG magnetic field strength at 10 μA supply current. The in-house program was developed using C++ for the bulk and sheet measurements of electrical parameters according to the relations developed by van der Pauw [75]. Findings of the curves, calculation of parameters of various characterization methods were performed by standard software (Make: MicroCal; Version: Origin 8.5).

3. Results and discussion

3.1. Structural characterization

Fig.1a shows the schematic diagram of In/Se stack, the images of In_xSe_y thin films obtained at different annealing temperatures have been displayed in Fig. 1b. Fig. 2a shows the X-ray diffraction (XRD) pattern of the as-deposited In/Se stack obtained at room temperature (300 K). The X-ray diffraction patterns of In_xSe_y thin films obtained on annealing at temperatures varying from 523 K to 673 K have been presented in Fig. 2b–e. The undertaken thin films show polycrystalline nature and provide mixed phases of InSe, In_4Se_3, and γ-In_2Se_3. The as-deposited In/Se stack show a dominating phase of orthorhombic In_4Se_3, few peaks of hexagonal (rhombo-centered) InSe and a single peak of hexagonal γ-In_2Se_3. The orthorhombic In_4Se_3 phase having space group *Pnnm* (58) was identified from its prominent peaks at '2θ' values of 27.87 (2)°, 28.93 (4)°, 40.72 (1)° which corresponded to (330), (311), (002) oriented planes (JCPDS card No. 83–0039) whereas the presence of InSe phase having space group *R3m* (160) was identified based on peaks at '2θ' values of 10.53 (2)°, 29.29 (1)°, 25.94 (3)° corresponding to (003), (006) and (101) oriented planes, respectively (JCPDS Card no. 73–0609). The γ- In_2Se_3 phase was observed through (202) peak at '2θ' values of 30.47 (8)° (JCPDS Card No. 71–0250). Thin films obtained at the annealing temperatures of 523 K and 573 K also exhibit mixed phases of In_4Se_3, InSe, and γ-In_2Se_3. The intensity values of InSe peaks increase while In_4Se_3 show reduction at 523 K and 573 K, moreover, the intensity of (202) peak of γ-In_2Se_3 increases significantly at 573 K. A phase transformation from In_4Se_3 to γ- In_2Se_3 was observed in the films at 623 K wherein the presence of γ- In_2Se_3 phase at 623 K was identified from the peaks at '2θ' values of 24.99 (7)°, 27.56 (3)°, and 30.50 (5)° corresponding to (110), (006) and (202) oriented planes (JCPDS Card No. 71–0250). Three peaks of InSe corresponding to (003), (006) and (101) oriented planes were also observed at 623 K. The γ- In_2Se_3 phase was further build-up at 673 K when more peaks emerged (Fig. 2e). Thus, the existence of a dominating phase of hexagonal γ- In_2Se_3 having space

Table 1
Presents the different parameters of the most significant peaks (MSPs) of different phases of In_xSe_y thin films.

Temperature (K)	d- spacing (Å)	2Θ (Degrees)	Intensity (cps)	FWHM (Degrees)	Crystallite size D (nm)	Microstrain(ϵ) ($\times 10^{-4}$)	Dislocation density (δ) ($\times 10^{-15}$ m^{-2})	Lattice parameters (a,b, c) (Å)	Cell Volume (V) (Å)^3
[a]Υ-In$_2$Se$_3$ Phase									
300*	2.930 (6)	30.47 (8)	98	0.656 (2)	14.67 (1)	7.8004 (6)	4.6458 (9)	–	–
523*	2.943 (1)	30.34 (5)	57	0.493 (8)	19.46 (8)	5.8435 (7)	1.8596 (5)	–	–
573*	2.927 (9)	30.50 (6)	213	0.449 (1)	21.44 (2)	5.3437 (4)	1.6883 (9)	–	–
623	2.928(1)*	30.50(5)	333 89	0.461(5)	20.86(7) 22.83	5.4909(7)	1.7349 (9)	[1]a = b = 7.093,	845.3109
	3.559(3)[#]	24.99(7)		0.400(9)	(1)	3.8782(1)	1.5856 (8)	[1]c = 19.401	(8)
673	2.926(6)*	30.52(1)	349 453	0.486(2)	19.80(8) 25.86	5.7881(8)	1.8276 (8)	[1]a = b = 7.089,	844.2506
	3.558(6)[#]	25.00(2)		0.353(9)	(5)	3.4242(3)	1.3997 (2)	[1]c = 19.3965	(5)
[c]InSe Phase									
300~	4.169 (8)	21.29 (1)	141	0.474 (6)	18.76 (1)	3.8931 (4)	1.9298 (2)	[3]a = b = 4.004, [3]c = 25.019	346.7405 (1)
523~	4.167 (1)	21.30 (5)	193	0.434 (5)	20.49 (3)	3.5666 (5)	1.7666 (2)	[3]a = b = 3.994, [3]c = 25.003	345.4560 (5)
573~	4.164 (1)	21.32 (1)	332	0.404 (1)	22.04 (5)	3.3184 (7)	1.6422 (6)	[3]a = b = 3.982, [3]c = 24.984	343.2222 (7)
623~	4.162 (8)	21.32 (7)	384	0.390 (1)	22.83 (5)	3.2047 (4)	1.5854 (5)	[3]c = 24.977	–
673~	4.123 (7)	21.54 (7)	26	0.578 (8)	15.41 (2)	4.8056 (1)	2.3490 (4)	[3]c = 24.725	–
[b]In$_4$Se$_3$ Phase									
300&	3.083 (3)	28.93 (4)	407	0.373 (4)	25.38 (5)	4.2043 (4)	1.4261 (6)	[2]a = 15.336, [2]b = 12.128, [2]c = 4.078	758.6069 (5)
523&	3.080 (6)	28.96 (1)	276	0.381 (6)	24.84 (5)	4.3008 (1)	1.4571 (5)	[2]a = 15.314, [2]b = 12.132, [2]c = 4.076	757.2756 (1)
573&	3.081 (5)	28.95 (2)	157	0.329 (9)	28.74 (3)	3.7162 (7)	1.2595 (6)	[2]a = 15.367, [2]b = 12.026, [2]c = 4.073	752.6811 (9)

[a] Υ-In$_2$Se$_3$: JCPDS (71–0250): (Sys: Hexagonal (primitive), S.G.: P6$_1$ (169), V: 846.69, Cell parameters: [1]a = [1]b = 7.110, [1]c = 19.34); Planes: (202)*, (110)[#]

[b] In$_4$Se$_3$: JCPDS (83–0039): (Sys: Orthorhombic (Primitive), S.G.: *Pnnm* (58), Vol: 768.23, Cell parameters:[2]a = 15.29, [2]b = 12.30, [2]c = 4.080); Plane:(311)&

[c] InSe:JCPDS (73–0609): (Sys: Hexagonal (rhomb-centered), S.G.: P6$_1$ (169), Vol: 346.01, Cell parameters: [3]a = b = 4.002, [3]c = 24.94); Plane: (006)~
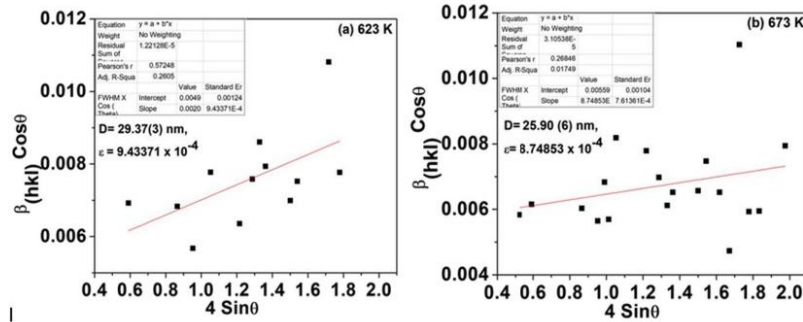

Fig. 5. a-b show the Williamson-Hall (W–H) plots of the XRD peaks of thin films of the γ- In$_2$Se$_3$ phase obtained at the annealing temperatures of 623 K and 673 K.

group P6$_1$ (169) was confirmed at 673 K. The films obtained at 673 K also show some effect of InSe phase (Fig. 4). Fig. 3 shows magnified views of 3D plots of the XRD data obtained in the '2θ' range from 20° to 32°, the patterns highlight intensity variations of prominent peaks of the phases observed at different annealing temperatures. The grain sizes of the crystallites present in the thin films calculated from the Scherrer formula using Eq (1).

$$D = \frac{0.94\lambda}{\beta \, Cos\theta} \tag{1}$$

where, λ is X-ray wavelength, β; the width at half maximum (FWHM) in radians and θ; the Bragg angle.

The Scherrer relation is highly recommended for the calculation of grain sizes using the X-ray diffraction data [50]. In the present case, the grain sizes were calculated from the Gaussian fit of the diffraction peaks, the values corresponding of most prominent peak (MSP) of each phase have been presented in Table 1. The grain sizes corresponding to MSP of hexagonal γ-In$_2$Se$_3$ phase vary from 14.67(1) nm to 25.86(5) nm with the increase in temperature from 300 K to 673 K; orthorhombic In$_4$Se$_3$ crystallites which show its presence from 300 K to 573 K, possess grains sizes from 24.85(5) nm to 28.74(3) nm whereas the grain size of hexagonal InSe increases from 18.76 (1) nm to 22.83(5) nm from 300 K to 623 K. This observed peak shows a low-intensity value of 26 cps at 673 K. On their comparison, it was observed that the crystallite size measured from SEM images (Fig. 9) is much larger than the same estimated from XRD data. Such variations in the grain sizes have been reported in several
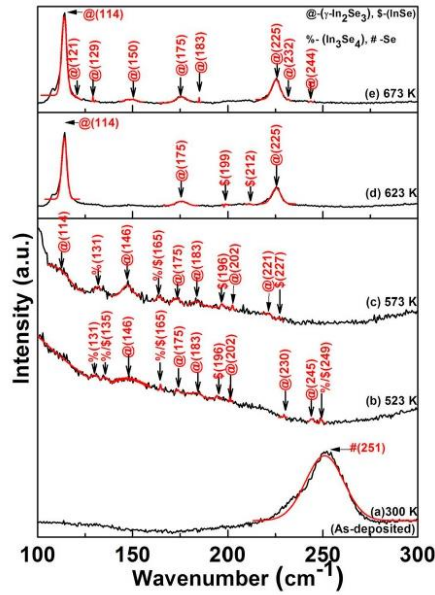
Fig. 6. a-e show typical Raman spectra of as-deposited and annealed samples of In$_x$Se$_y$ thin films.

research papers [51]. Getting bigger crystallite size from the surface morphology is ascribed to an agglomeration of smaller grains whereas the XRD provides information about the average crystallite size of coherently scattered units [52]. The number of phases present in the films and intensity variations of corresponding MSPs at different temperatures is indicated in the bar chart shown in Fig. 4. The microstrain (ϵ) and dislocation density (δ) are indications of the dislocation network in thin films [51]. The phenomena of microstrain and dislocation density developed during the deposition and post-annealing of the films are calculated from Eqs. (2) and (3), respectively [51].

$$\epsilon = \frac{\beta_{(hkl)} Cos\theta}{4} \tag{2}$$

$$\delta = \frac{1}{D^2} \tag{3}$$

where, $\beta_{(hkl)}$; the width at half maximum (FWHM) in radians and θ; the Bragg angle and D; crystallite size.

The ϵ & δ values of the films obtained at different temperatures are also shown in Table 1. It is observed from the table that the micro-strain and dislocation values of the γ- In$_2$Se$_3$ phase decrease while crystallite size increases with annealing temperature. The reduction of microstrain and dislocation density with temperature could be owing to the decreased lattice imperfections. Therefore, the formation of high-quality γ- In$_2$Se$_3$ film is observed in the present work. Similar growth of the γ-In$_2$Se$_3$ films have already been reported in the literature by several authors [51–53].

The grain size (D) and internal lattice strain (ϵ) induced due to crystal imperfection and distortion were also calculated from Williamson-Hall (W–H) analysis using Eq. (4) [52,53]:

$$\beta_{(hkl)} Cos\theta = \frac{K\lambda}{D} + 4\epsilon Sin\theta \tag{4}$$

The above-mentioned Williamson-Hall (W–H) equation was applied

to the γ- In$_2$Se$_3$ phase and the plots were drawn using '4sinθ' along the x-axis and 'β$_{(hkl)}$ cosθ' along y-axis [53]. The crystalline size (D) and internal lattice strain (ϵ) were estimated from the y-intercept and the slope of the linear fit, respectively. The W–H plots from the XRD peaks of γ-In$_2$Se$_3$ phase obtained at 623 K and 673 K samples have been shown in Fig. 5a-b. The films obtained at 673 K show lower strain values in comparison to the samples grown at 623 K. The decrease in strain values may be a result of the reduction of InSe in the grown samples at high temperatures. Further, the unit cell parameters for hexagonal γ-In$_2$Se$_3$; InSe and orthorhombic In$_4$Se$_3$ crystal systems were calculated by using Eq. (5) and Eq. (6), respectively [50].

$$\frac{1}{d^2} = \frac{4}{3}\left(\frac{h^2 + hk + k^2}{a^2}\right) + \frac{l^2}{c^2} \tag{5}$$

$$\frac{1}{d^2} = \frac{h^2}{a^2} + \frac{k^2}{b^2} + \frac{l^2}{c^2} \tag{6}$$

The cell parameter of the phases of γ- In$_2$Se$_3$, InSe, and In$_4$Se$_3$ are found close to the values of reported values of corresponding bulk materials as per JCPDS cards (refer Table 1).

3.2. Raman spectra analysis

The Raman spectroscopy is an important exploratory instrument used to identify the crystalline phase of material based on distinct vibrational modes [54,55]. The spectroscopic analysis of the vibrational spectra furnishes useful information regarding the nature of the chemical bond and order of the atomic arrangement [31]. In the present work, the Raman spectra were recorded with a laser excitation source at a wavelength of 532 nm and measured in the wavenumber range of 100–300 cm⁻¹. The results show some deviations from the standard values of wavenumber for some of the peaks.; Nevertheless, main peaks were observed at the reported wavenumber values for similar peaks in already published work. The vibrational spectra of the phases present in the In$_x$Se$_y$ films were measured at different annealing temperatures by using this method. The as-deposited In/Se stack shows a broad peak at 251 cm⁻¹ (Fig. 6a) corresponding to monoclinic crystal (m-Se) with Se$_8$ monomer rings of a-Se. The spectra, thus, confirm the presence of selenium on the top layer in the stack. Similar peaks for a-Se have already been reported by various authors [49,56]. No other vibrational spectra peak was observed in the as-grown samples. The 523 K and 573 K annealed samples (Fig. 6b-c) exhibit several broad peaks; the plots show complex spectra due to multiple phases of In$_x$Se$_y$. Whereas the films obtained at 623 K and 673 K (Fig. 6d-e) affirm the presence of γ-In$_2$Se$_3$ and InSe phases. The γ-In$_2$Se$_3$ phase has been identified by the Raman peaks at 108 cm⁻¹, 114 cm⁻¹, 121 cm⁻¹, 129 cm⁻¹, 150 cm⁻¹, 175 cm⁻¹, 183 cm⁻¹, 225 cm⁻¹, 232 cm⁻¹, and 244 cm⁻¹, these peaks match with the results of several authors [25,31,55,57]. The presence of the InSe phase at the annealing temperatures above 623 K was confirmed from the low-intensity peaks at 199 cm⁻¹ and 212 cm⁻¹ [58,59]. Thus, as per Raman spectra, the γ-In$_2$Se$_3$ is found to be a stable phase in the In$_x$Se$_y$ alloy, and In$_4$Se$_3$ and InSe phases do not show much impact, particularly at higher annealing temperatures.

3.3. Optical studies

The optical behavior of thin films is sensitive to the micro-structure and depends on its growth conditions [60]. The samples show a perpetual change in color to the naked eyes from grey to brown with an increase in the annealing temperature (Fig. 1b). The transmittance spectra of the In$_x$Se$_y$ thin films grown at 523 K–673 K are shown in Fig. 7a. The transmission percentage (TP) increases with annealing temperature. The TP of the films grown at 673 K shows a 60%, thus, indicates the presence of the γ-In$_2$Se$_3$ phase. A similar transmission percentage value for γ-In$_2$Se$_3$ thin-films has been reported in the literature [61]. The absorption edge lies near 950 nm in the 623 K samples.
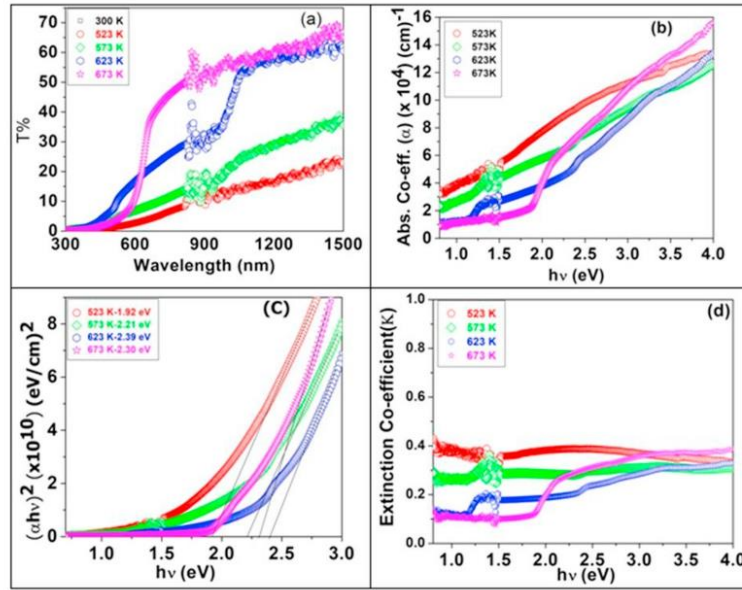
Fig. 7. shows plots of the (a) T % versus wavelength (λ); (b) the absorption co-efficient (α) versus photon energy (hν); (c) the (αhν)² versus (hν); and (d) extinction co-efficient (κ) versus photon energy (hν) of the In_xSe_y thin films obtained at different temperatures.
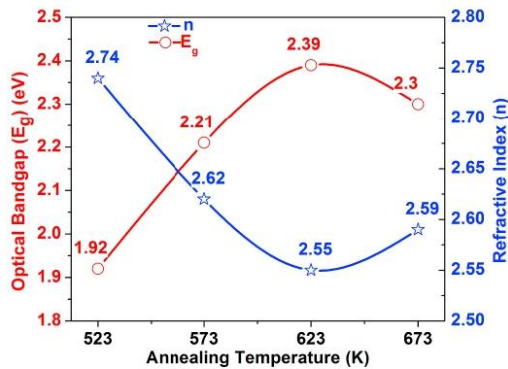

Fig. 8. represents variations of the optical bandgap (E_g) and refractive index (n) of In_xSe_y thin films with annealing temperature.

However, it undergoes a blue-shift in the samples obtained at 673 K. Furthermore, the absorption coefficient (α) values of thin films are calculated using Eq. (7) as under [62].

$$\alpha = \frac{1}{t}\ln\left(\frac{100}{T\%}\right) \qquad (7)$$

where α, T%, t represent absorption co-efficient, transmission percentage, and thickness, respectively. The variations of absorption co-efficient (α) with the photon energy (hν) of the annealed In_xSe_y thin films are shown in Fig. 7b. The α values vary from $2 \times 10^4 \, cm^{-1}$ to $1.6 \times 10^5 \, cm^{-1}$ with temperature. Moreover, a band to band transition occurs

in the high photon energy region (hν > 1.8 eV) in the 623 K and 673 K samples. The absorption corresponds to the electron excitation from the valence to the conduction band and is used to determine the value of optical bandgap (E_g) [62]. The Tauc relation corresponds to electron excitation is represented by Eq. (8) [62].

$$\alpha h\nu = A\left(h\nu - E_g\right)^n \qquad (8)$$

where A; a constant, ν; photon frequency, h; plank constant, E_g; optical bandgap, and α; absorption co-efficient. The exponent 'n' depends on the type of transition, n = 2, 1/2, 2/3, and 1/3 corresponding to allowed direct, allowed indirect, forbidden direct, and forbidden indirect, respectively [62]. The value of $n = 1/2$ is used for allowed direct transition and $n = 2$ for allowed indirect transition for the bandgap materials [62]. The linear fit of the curves of the Tauc plot of $(\alpha h\nu)^2$ versus $(h\nu)$ on the x-axis (Fig. 7c) was used to determine the allowed direct bandgap values of the films. The direct nature of the electronic transition between valence and conduction band was determined based on the linear nature of the plots at the higher photon energy region. The E_g values of the In_xSe_y thin films vary from 1.92 eV to 2.30 eV, these have been marked in the inset table of Fig. 7c. The $(\alpha h\nu)^{0.5}$ versus $(h\nu)$ plots did not show linearity in the curves, thus, the presence of indirect bandgaps in the films ignored. Further, the bandgaps increase with temperature; the change is attributed to the realignments in crystallite orientations and divulges strong interactions between the films and the substrate [63]. Moreover, the increase in the value of optical bandgap with annealing temperature may occur due to the formation of localized states in the high photon energy region. The results are in agreement with the already reported work [61,64–66]. As the bandgaps (E_g) correspond to the visible region of the E.M. spectrum, thus, the undertaken In_xSe_y thin films become useful in various photovoltaic applications viz. buffer layers in solar cell structure and photovoltaic sensors. These applications of In_xSe_y thin films have been reported earlier in several publications [1–3,5,11,16,32].
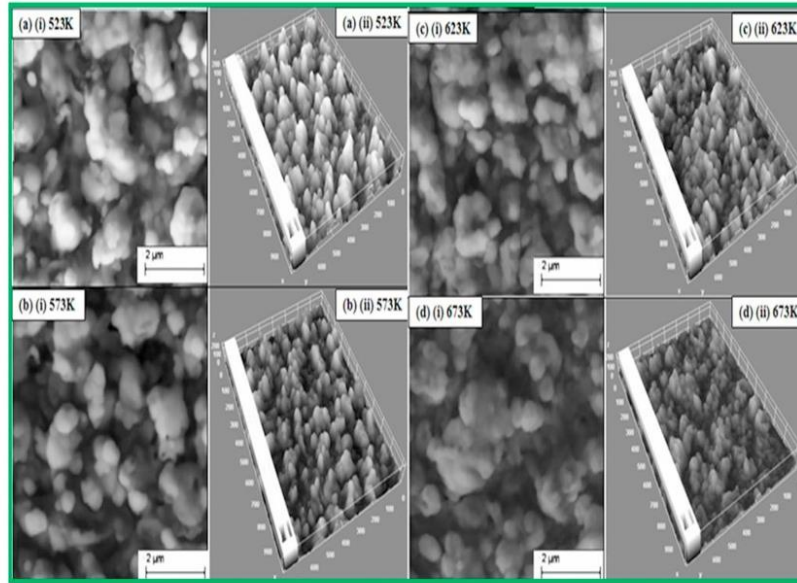
Fig. 9. a-d show 2D/3D scanning electron microscopic (SEM) images of the In$_x$Se$_y$ thin films obtained at 523 K, 573 K, 623 K, and 673 K.
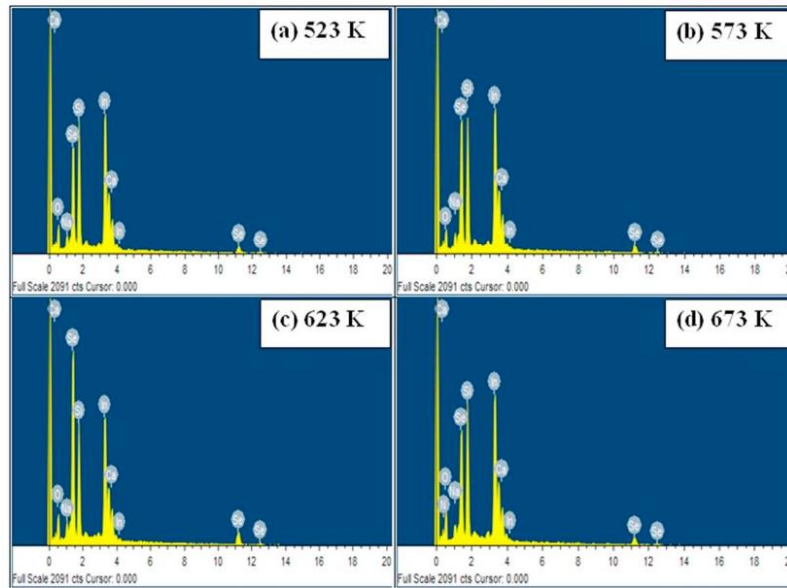

Fig. 10. a-d show the EDAX spectra of In$_x$Se$_y$ thin films obtained at the annealing temperatures 523 K, 573 K, 623 K, and 673 K.

The refractive index (n) of the annealed thin films of In$_x$Se$_y$ was calculated using Herve-Vandamme relation as per Eq. (9) given as under [67].

$$n^2 = 1 + \left[\frac{A}{(E_g + B)} \right]^2 \tag{9}$$

8

89

Table 2

Presents the atomic percentages, In/Se ratio and stoichiometry of the In_xSe_y thin films at different annealing temperatures.

Annealing Temperature (K)	Element Atomic %		Atomic ratio	Alloy stoichiometry
	In	Se	In/Se	
523	59.60	40.40	1.475 (2)	$In_2Se_{1.36}$
573	54.96	45.04	1.220 (2)	$In_2Se_{1.64}$
623	44.81	55.19	0.811 (9)	$In_2Se_{2.46}$
673	58.68	41.32	1.420 (1)	$In_2Se_{1.4}$

Here 'A' and 'B' are constants having values of 13.6 eV and 3.4 eV, respectively and E_g is the optical bandgap. The refractive index (n) of the films decreases from 2.74 to 2.55 with an increase in the annealing temperature. The variations of optical bandgap (E_g) and refractive index (n) with annealing temperature are presented in Fig. 8. The changes in the refractive index values may be due to the variations in the packing density and the polarizability of the local field [67].

The 'extinction coefficient (k)' has been used to determine the degree of surface uniformity by several authors [68,69]. It specifies how effectively light of a particular wavelength is absorbed in the material [70]. It also provides information about the smoothness of the surface of thin films. The value of 'k' has been calculated from the absorption coefficient (α) using the expression given in Eq. (10) [68–70].

$$\kappa = \frac{\alpha\lambda}{4\pi} \tag{10}$$

where α, λ represent the absorption coefficient and wavelength of incident radiation, respectively. The variations of extinction coefficient (k) with photon energy ($h\nu$) for the annealed In_xSe_y thin films have been shown in Fig. 7d. The low 'k' values of the films varying from 0.1 to 0.4 indicate a high degree of surface uniformity and smoothness. Thus, these films are highly useful in electronic device fabrication. The correlation between the low 'k' values and smoothness of the surface of the thin films has already been established in several research publications [68–70].

3.4. Morphological and compositional analysis

The scanning electron microscopy is a technique used to determine of surface morphology of materials. It scans the structure of the surface of materials at a microscopic scale with much higher resolution and greater depth of field [71]. It furnishes information about the shape and size of the grains of polycrystalline materials [72]. Two and three-dimensional scanning electron microscopic (SEM) images of the In_xSe_y films grown at different annealing temperatures are shown in Fig. 9a–d. The films are homogeneous throughout, without cracks well cover the entire glass substrate. The particles are densely packed and complex structured; no single particle is seen separately. The SEM images at 523 K and 573 K show a mixture of particles of different shapes, sizes, and shades. The small particles are agglomerated to form large grains; some voids are also seen in the grown samples. Furthermore, few modifications in shapes and orientations of the grains are seen at 623 K; the images exhibit irregularly shaped bigger particles. Similar patterns appear at 673 K, the density of particles, however, reduces at this
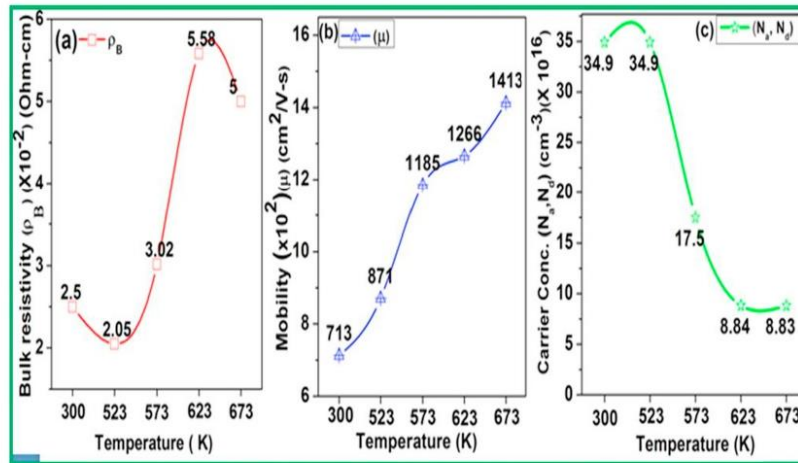

Fig. 11. a-c show variations of the resistivity (ρ), mobility (μ), and carrier concentrations (N_A, N_D) of the In_xSe_y thin films grown at different annealing temperatures.

Table 3

The bulk resistivity (ρ_B), sheet resistance (R_s), mobility (μ), carrier concentration (N_A, N_D), and conductivity type of In_xSe_y alloy films obtained at different annealing temperatures.

Annealing Temperature (K)	Film thickness (nm)	Bulk Resistivity (ρ_B) (Ω-cm)	Sheet Resistance (R_s) (Ω/square)	Mobility (μ) (cm²/V-s)	Carrier Concentration (N_A, N_D) (cm⁻³)	Conductivity type
300	551	2.50×10^{-2}	4.54×10^2	713.5	34.9×10^{16}	p- type
523	460	2.05×10^{-2}	4.45×10^2	871.1	34.9×10^{16}	n- type
573	433	3.02×10^{-2}	6.97×10^2	1184.9	17.5×10^{16}	n-type
623	428	5.58×10^{-2}	1.31×10^3	1266.0	8.84×10^{16}	n-type
673	395	5.00×10^{-2}	1.13×10^3	1412.6	8.83×10^{16}	n-type

9

Table 4
Comparison of the important parameters of different thin film materials for used as buffer in PV solar cells fabrication.

Buffer Material	Film growth process	Bandgap (eV)	Absorption Coefficient (cm^{-1})	Refractive Index(n)	Thickness (nm)	Mobility (cm^2/V.s)	Solar cell structure	Efficiency (%)	Challenges/Issues
CdS [83–86]	Thermal evaporation	2.50 [83] 2.42 [86]	2 × 10^4 [83] 10^5 [85]	2.54–2.30 [83] 2.22–3.47 [85]	263-282 [83] 87 [84] 500 [85]	332.9 [84] 1-110 [85] 50 [86]	CdS/CIGS [86]	11.7–16.1 [86]	Cadmium toxicity and its disposal
ZnO [87–91]	Electrodiposited [87] RF Magnetron sputtering [88] Spray Pryolysis [90] Sputtering [91]	1.59 [89] 3.15–3.24 [90]	~10^5 [91]	1.88–1.98 [91]	20-116 [88] 60 [89] 600-2350 [90] 75-200 [91]	9.19-21.40 [88]	ZnO/CdTe [87] SLG/Mo/CISe/CdS/i-ZnO/AZO/Ni/Al [89]	9.5 [87] 11.4 [89]	Poor efficiency but CdS alternate
ZnS [92–94]	CBD [92] Thermal evaporation [93]	3.40–3.49 [92] 3.52–3.48 [93] 3.46 [94]	10^4 [92]	2.33 [92]	30-90 [92] 400-1000 [93] 445 [94]	180 [94]	ZnS/CIGS [92]	7.7–9.4 [92]	Further improvements are under studies
In$_2$S$_3$ [95–100]	Sputtering [95] CBD [96] Thermal evaporation [97–99] Spray pyrolysis [100]	1.144 [95] 2.84–3.04 [97] 1.99–2.49 [99] 2.33–2.65 [100]	10^4-10^5 [97]	2.293–2.367 [97] 2.50–2.71 [99] 1.58–1.82 [100]	85 [95] 70 [96] 150 [97] 500 [99]	39.7–71.6 [100]	In$_2$S$_3$/CIGS [95,96]	13.6 [95] 2.3 [96]	As an CdS alternate as well as cost effective
In$_2$Se$_3$ [28,101] γ-In$_2$Se$_3$ [32, 61]	Three stage Co-Evaporation [32,61]	1.7–2.6 [28] 2.2 [32] 1.45–2.15 [61]	10^4 [28,32]	2.50–2.72 [63] 3.1–2.80 [63]	80-100 [28] 100 [32] 95-1050 [61] 480 [101]	0.5–30 [101]	Mo/CIS/In$_2$Se$_3$/ZnO Mo/CIS/ZnO/CdS [28] Al/ITO/ZnO/In$_2$Se$_3$/CuIn$_3$Se$_5$/CuInSe$_2$/Mo [28]	8.3 [28] 9.2 [28]	As an CdS alternate as well as low cost processing
γ-In$_2$Se$_3$ (present work)	SELD	1.92–2.39	2 × 10^4– 1.5 × 10^5	2.75–2.55	551–395	871–1413	–	–	As an CdS alternate and easily scalable

temperature. These patterns look sharp and possess high crystallinity.

The atomic percentage of the elements present in the In_xSe_y thin films at different annealing temperatures has been calculated from the energy dispersive X-ray analysis (EDAX). The EDAX spectra of the samples grown at different annealing temperatures have been shown in Fig. 10a–d; the corresponding atomic percentages are mentioned in Table 2. The In/Se value of 1.475 (2) at 523 K facilitates the formation of the In_4Se_3 phase; the value reduces to 1.220 (2) at 573 K as more Se gets attached to In and causes the formation of InSe. Moreover, the In/Se value of 0.811 (9) at 623 K advances towards the stoichiometry of $γ-In_2Se_3$. The results of the EDAX, X-ray diffraction data, and Raman spectra suggest the transformation from orthorhombic In_4Se_3 to the hexagonal $γ-In_2Se_3$ phase at 623 K. A reverse trend of the In/Se is seen at 673 K wherein the value increases to 1.420 (1). This change is attributed to the re-evaporation of Se from the films due to its excessive vapor pressure at higher annealing temperatures [57]. The re-evaporation of Se also causes a reduction in the InSe phase and induces re-organization in the $γ-In_2Se_3$ peaks. There are some emission peaks other than In and Se exist in the EDAX plots which pertains to the materials of the corning glass substrate. These emission peaks of the corning glass substrate have also been reported earlier by several authors [73].

3.5. Hall measurement

Hall measurement is one of the most convincing methods to determine carrier concentration and mobility of conductive materials [74]. Its wide-spread use as a simple and fast routine measurement technique is based on the simplicity of the van der Pauw formulation which does not require precise micro-structuring during sample preparation [75]. The trends of variations of resistivity (ρ), mobility (μ), and carrier concentration (N_d) of the films, grown at different annealing temperatures as measured using this method, are shown in Fig. 11a–c. The p-type conductivity of the as-grown In/Se stack is attributed to the Se layer at the top. The presence of a-Se top layer in the as-grown In/Se stack has also been noticed in the Raman spectra. The p-type conductivity of the Se films has already been reported by several authors [76]. On the reverse, the films obtained at 523 K–673 K exhibit n-type conductivity. The n-type conductivity of In_xSe_y films has also been observed by several researchers [77–79]. The films possess a multi-faceted structure in which the grain sizes of the crystallites change with an increase in annealing temperature. Further, the flow of charge carriers is affected by the grain boundaries of different phases. The samples obtained at 573 K show an improved $γ- In_2Se_3$ phase, however, InSe and In_4Se_3 also exist in these films. These variations in the phases cause changes in the electrical parameters of the grown thin film samples. Upon changing the annealing temperature from 523 K to 573 K, the mobility increases from 871 to 1185 cm^2/V-s. This change is attributed to the improvement in the $γ-In_2Se_3$ phase [78,79]. At 623 K, the In_4Se_3 transforms to the $γ-In_2Se_3$ phase, this causes the formation of a strong $γ-In_2Se_3$ and contributes to the further increase in the mobility to 1266 cm^2/V-s. The mobility value advances to 1413 cm^2/V-s at 673 K amidst a change in In/Se ratio from 0.811(9) to 1.420(1). This advancement in the mobility value associates with the presence of excess indium (In) in the samples. Besides, the increased sizes of the $γ-In_2Se_3$ crystallites also play a role in the reduction of the inter-crystalline barriers and contribute to high carrier mobility [25,80–82]. While in the entire annealing temperature range, the bulk resistivity (ρ_B), and carrier concentration (N_D) indicate a small change (Table 3). The values of various electrical parameters obtained at different annealing temperatures have been mentioned in Table 3. The increase in mobility and changes of other parameters of $γ-In_2Se_3$ are ascribed to the phase transformations and changes in the composition values. A comparison of the important parameters of indium selenide thin films to those of similar materials has been drawn in Table 4 [83–101].

4. Conclusion

Thin films of the $γ-In_2Se_3$ phase were obtained on annealing of the In/Se stack obtained from the SELD method. The films provide good adhesion to the corning glass substrate and exhibit n-type conductivity. The particles are uniformly distributed, irregular shaped, and complex structured. Moreover, the surface of the films provides a high degree of smoothness. The films exhibit changing phases on thermal annealing. The direct bandgap of the films falls within the visible region of the E.M. spectrum. The films exhibit high transmission (60%) and show bandgap tuning, the absorption co-efficient values $\sim 10^5$ cm^{-1}. The changes in mobility increase and other parameters of $γ-In_2Se_3$ with annealing temperature are attributed to the phase transformations, compositional change, and growth of the crystallites. These properties of the $γ-In_2Se_3$ thin films make it a suitable choice for buffer layers in the solar structure.

CRediT authorship contribution statement

Rajesh Niranjan: Software, Validation, Investigation, Writing - original draft, Formal analysis, Resources, Data curation, Methodology. **Naresh Padha:** Conceptualization, Visualization, Supervision, Writing - review & editing.

Declaration of competing interest

The authors declare that they have no known competing financial interests or personal relationships that could have appeared to influence the work reported in this paper.

Acknowledgments

References

[1] T. Zhai, X. Fang, M. Liao, X. Xu, L. Li, B. Liu, Y. Koide, Y. Ma, J. Yao, Y. Bando, D. Golberg, Fabrication of high-quality In_2Se_3 nanowire arrays toward high-performance visible-light photodetectors, ACS Nano 4 (3) (2010) 1596–1602, https://doi.org/10.1021/nn9012466.

[2] C.H. Ho, Y.C. Chen, Thickness-tunable band gap modulation in $γ-In_2Se_3$, RSC Adv. 3 (2013) 24896–24899, https://doi.org/10.1039/c3ra44624g.

[3] J. Zhou, Q. Zeng, D. Lv, L. Sun, L. Niu, W. Fu, F. Liu, Z. Shen, C. Jin, Z. Liu, Controlled synthesis of high-quality monolayered $α-In_2Se_3$ via physical vapor deposition, Nano Lett. 15 (10) (2015) 6400–6405, https://doi.org/10.1021/acs.nanolett.5b01590.

[4] M.A. Contreras, A.M. Gabor, A.L. Tennant, S. Asher, J. Tuttle, R. Noufi, 16.4% total-area conversion efficiency thin-film polycrystalline MgF_2/ZnO/CdS/Cu(Zn, Ga)Se,/Mo solar cell, Prog. Photovoltaics 2 (4) (1994) 287–292, https://doi.org/10.1002/pip.4670020404.

[5] S.H. Know, B.T. Ahn, S.K. Kim, K.H. Yoon, J. Song, Growth of $CuIn_3Se_5$ layer on $CuInSe_2$ films and its effect on the photovoltaic properties of In_2Se_3/$CuInSe_2$ solar cells, Thin Solid Films 323 (1998) 265–269, https://doi.org/10.1016/S0040-6090(97)00928-0.

[6] T. Nishida, M. Terao, Y. Miyauchi, S. Horigome, T. Kaku, N. Ohta, Single-beam overwrite experiment using InSe based phase-change optical media, Appl. Phys. Lett. 50 (11) (1987) 667–669, https://doi.org/10.1063/1.98060.

[7] D. Kang, T. Rim, C.K. Baek, M. Meyyappan, J.S. Lee, Investigation of electromigration in In_2Se_3 nanowire for phase change memory devices, Appl. Phys. Lett. 103 (23) (2013) 233504, https://doi.org/10.1063/1.4838755.

[8] J. Ye, T. Yoshida, Y. Nakamura, O. Nittono, Optical activity in the vacancy ordered III_2VI_3 compound semiconductor $(Ga_{0.3}In_{0.7})_2Se_3$, Appl. Phys. Lett. 67 (21) (1995) 3066–3088, https://doi.org/10.1063/1.114866.

11

[9] S.R. Tamalampudi, Y.Y. Lu, R. Kumar U, R. Sankar, C.D. Liao, K. Moorthy B, C. H. Cheng, F.C. Chou, Y.T. Chen, High performance and bendable few-layered InSe photodetectors with a broad spectral response, Nano Lett. 14 (5) (2014) 2800–2806, https://doi.org/10.1021/nl500817g.

[10] I.V. Bodnar, G.A. Ilchuk, R.Yu Petrus, V.Yu Rud, Yu V. Rud, M. Serginov, Electrical Properties of In₂Se₃ single crystals and photosensitivity of Al/In₂Se₃ Schottky barriers, Semiconductors 43 (9) (2009) 1138–1141, https://doi.org/10.1134/S1063782609090061.

[11] Q.L. Li, Y. Li, J. Gao, S.D. Wang, X.H. Sun, High performance single In₂Se₃ nanowire photodetector, Appl. Phys. Lett. 99 (24) (2011) 243105, https://doi.org/10.1063/1.3669513.

[12] X. Tao, Y. Gu, Crystalline–crystalline phase transformation in two-dimensional In₂Se₃ thin layers, Nano Lett. 13 (8) (2013) 3501–3505, https://doi.org/10.1021/nl400888p.

[13] A.A. Yadav, S.D. Salunke, Photoelectrochemical properties of In₂Se₃ thin films: effect of substrate temperature, J. Alloys Compd. 640 (2015) 534–539, https://doi.org/10.1016/j.jallcom.2015.04.041.

[14] C. Julien, A. Khelfa, N. Benramdane, J.P. Guesdon, P. Dzwonkowski, I. Samaras, M. Balkanski, Lithium insertion in indium selenide films: application to microbatteries, Mater. Sci. Eng. B 23 (2) (1994) 105–115, https://doi.org/10.1016/0921-5107(94)90342-5.

[15] R. Sreekumar, R. Jayakrishnan, C. Sudha Kartha, K.P. Vijayakumar, Anomalous photoconductivity in gamma In₂Se₃, J. Appl. Phys. 100 (3) (2006) 033707, https://doi.org/10.1063/1.2219002.

[16] G. Almeida, S. Dogan, G. Bertoni, C. Giannini, R. Gaspari, S. Perissinotto, R. Krahne, S. Ghosh, L. Manna, Colloidal monolayer β-In₂Se₃ nanosheets with high photoresponsivity, J. Am. Chem. Soc. 139 (8) (2017) 3005–3011, https://doi.org/10.1021/jacs.6b11255.

[17] C.H. de Groot, J.S. Moodera, Growth and characterization of a novel In₂Se₃ structure, J. Appl. Phys. 89 (8) (2001) 4336–4340, https://doi.org/10.1063/1.1355287.

[18] C. Amory, J.C. Bernede, S. Marsillac, Study of a growth instability of γ-In₂Se₃, J. Appl. Phys. 94 (10) (2003) 6945–6948, https://doi.org/10.1063/1.1622117.

[19] J. Jasinski, W. Swider, J. Washburn, Z. Liliental-Weber, A. Chaiken, K. Nauka, G. A. Gibson, C.C. Yang, Crystal structure of κ- In₂Se₃, Appl. Phys. Lett. 81 (23) (2002) 4356–4358, https://doi.org/10.1063/1.1526925.

[20] S. Popovic, A. Tonejc, B. Grzeta-Plenkovic, B. Celustka, R. Trojko, Revised and new crystal data for indium selenides, J. Appl. Crystallogr. 12 (1979) 416–420, https://doi.org/10.1107/S0021889879012863.

[21] C. Manolikas, New results on the phase transformations of In₂Se₃, J. Solid State Chem. 74 (2) (1988) 319–328, https://doi.org/10.1016/0022-4596(88)90361-1.

[22] J. Ye, S. Soeda, Y. Nakamura, O. Nittono, Crystal structures and phase Transformation in In₂Se₃ compound semiconductor, Jpn. J. Appl. Phys. 37 (8) (1998) 4264–4271, https://doi.org/10.1143/JJAP.37.4264.

[23] N. Balakrishnan, E.D. Steer, E.F. Smith, Z.R. Kudrynskyi, Z.D. Kovalyuk, L. Eaves, A. Patane, P.H. Beton, Epitaxial growth of γ-InSe and α, β, and γ-In₂Se₃ on ε-GaSe, 2D Mater. 5 (3) (2018), 035026, https://doi.org/10.1088/2053-1583/aac479.

[24] G. Han, Z.G. Chen, J. Drennan, J. Zou, Indium selenides: structural characteristics, synthesis and their thermoelectric performances, Small 10 (14) (2014) 2747–2765, https://doi.org/10.1002/smll.201400104.

[25] S. Marsillac, J.C. Bernede, M. Emziane, J. Wery, E. Faulques, P. Le Ray, Properties of photoconductive in Se thin films, crystallized by post-deposition heat treatment in a nitrogen atmosphere, Appl. Surf. Sci. 151 (3–4) (1999) 171–179, https://doi.org/10.1016/S0169-4332(99)00300-1.

[26] S. Marsillac, A.M. Combot-Marie, J.C. Bernede, A. Conan, Experimental evidence of the low-temperature formation of γ-In₂Se₃ thin films obtained by a solid-state reaction, Thin Solid Films 288 (1–2) (1996) 14–20, https://doi.org/10.1016/S0040-6090(96)08799-8.

[27] D. Hariskos, S. Spiering, M. Powalla, Buffer layers in Cu (In, Ga)Se₂ solar cells and modules, Thin Solid Films 480–481 (2005) 99–109, https://doi.org/10.1016/j.tsf.2004.11.118.

[28] G. Gordillo, C. Calderon, CIS thin-film solar cells with evaporated InSe buffer layers, Sol. Energy Mater. Sol. Cells 77 (2) (2003) 163–173, https://doi.org/10.1016/S0927-0248(02)00319-7.

[29] S. Li, Y. Yan, Y. Zhang, Y. Ou, Y. Ji, L. Liu, C. Yan, Y. Zhao, Z. Yu, Monophase γ-In₂Se₃ thin film deposited by magnetron radio-frequency sputtering, Vacuum 99 (2014) 228–232, https://doi.org/10.1016/j.vacuum.2013.06.007.

[30] Y.X. Fang, H. Zhang, F. Azad, S.P. Wang, F.C.C. Ling, S.C. Su, Band offset and an ultra-fast response UV-VIS photodetector based on α-In₂Se₃/p-Si heterojunction heterostructures, RSC Adv. 8 (2018) 29555–29561, https://doi.org/10.1039/c8ra05677c.

[31] R. Panda, R. Naik, N.C. Mishra, Low-temperature growth of γ phase in thermally deposited In₂Se₃ thin films, Phase Transitions 91 (8) (2018) 862–871, https://doi.org/10.1080/01411594.2018.1508680.

[32] S.H. Know, B.T. Ahn, S.T. Kim, F. Adurodija, K.H. Kang, K.H. Yoon, J. Song, Characterization of CuInSe₂ thin films by co-evaporation method, J. Kor. Phys. Soc. 31 (5) (1997) 796–801.

[33] H. Bouzouita, N. Bouguila, S. Duchemin, S. Fiechter, A. Dhouib, Preparation and characterization of In₂Se₃ thin films, Renew. Energy 25 (1) (2002) 131–138, https://doi.org/10.1016/S0960-1481(00)00193-2.

[34] I.H. Mutlu, M.Z. Zarbaliyev, F. Aslan, Indium selenide thin film preparation by sol-gel technique, J. Sol. Gel Sci. Technol. 43 (2007) 223–226, https://doi.org/10.1007/s10971-007-1573-3.

[35] P.P. Hankare, M.R. Asabe, P.A. Chate, K.C. Rathod, Structural, optical and microscopic properties of chemically deposited In₂Se₃ thin films, J. Mater. Sci.

[36] Y.C. Huang, Z.Y. Li, W.Y. Uen, S.M. Lan, K.J. Chang, Z.J. Xie, J.Y. Chang, S. C. Wang, J.L. Shen, Growth of γ-In₂Se₃ films on Si substrates by metal-organic chemical vapor deposition with different temperatures, J. Cryst. Growth 310 (7–9) (2008) 1679–1685, https://doi.org/10.1016/j.jcrysgro.2007.11.174.

[37] M. Lin, D. Wu, Y. Zhou, W. Huang, W. Jiang, W. Zheng, S. Zhao, C. Jin, Y. Guo, H. Peng, Z. Liu, Controlled growth of atomically thin In₂Se₃ flakes by van der Waals epitaxy, J. Am. Chem. Soc. 135 (36) (2013) 13274–13277, https://doi.org/10.1021/ja406351u.

[38] Y. Yan, S. Li, Y. Ou, Y. Ji, Z. Yu, L. Liu, C. Yan, Y. Zhang, Y. Zhao, Effects of pressure and deposition time on the characteristics of In₂Se₃ films grown by magnetron sputtering, Electron, Mater. Lett. 10 (6) (2014) 1093–1101, https://doi.org/10.1007/s13391-014-4081-y.

[39] T. Okamoto, A. Yamada, M. Konagai, Growth and characterization of In₂Se₃ epitaxial films by molecular beam epitaxy, J. Cryst. Growth 175–176 (2) (1997) 1045–1050, https://doi.org/10.1016/S0022-0248(96)00984-0.

[40] C.H. Ho, M.H. Lin, C.C. Pan, Optical-memory switching and oxygen detection based on the CVT grown γ - and α -phase In₂Se₃, Sensor. Actuator. B Chem. 209 (2015) 811–819, https://doi.org/10.1016/j.snb.2014.12.036.

[41] J.M. Czerniawski, J.L. Stickney, Electrodeposition of In₂Se₃ using potential pulse atomic layer deposition, J. Phys. Chem. C 120 (29) (2016) 16162–16167, https://doi.org/10.1021/acs.jpcc.6b00320.

[42] V.D. Botcha, Y. Hong, Z. Huang, Z. Li, Q. Liu, J. Wu, Y. Lu, X. Liu, Growth and thermal properties of various In₂Se₃ nanostructures prepared by single-step PVD technique, J. Alloys Compd. 773 (2019) 698–705, https://doi.org/10.1016/j.jallcom.2018.09.335.

[43] K. Bindu, C. Sudha Kartha, T. Abe, Y. Kashiwaba, Structural, optical and electrical properties of In₂Se₃ thin films formed by annealing chemically deposited Se and vacuum evaporated in stack layers, Appl. Surf. Sci. 191 (1–4) (2002) 138–147, https://doi.org/10.1016/S0169-4332(02)00172-1.

[44] H.J. Gysling, A.A. Wernberg, Molecular design of single-source precursors for 3-6 semiconductor films: control of phase and stoichiometry in In₂Se_y films deposited by a spray MOCVD process using single-source reagents, Chem. Mater. 4 (4) (1992) 900–905, https://doi.org/10.1021/cm00022a028.

[45] J.Y. Emery, L. Brahim-Otsmane, M. Jouanne, C. Julien, M. Balkanski, Growth conditions of In_xSe_y films by molecular beam deposition, Mater. Sci. Eng. B 3 (1–2) (1989) 13–17, https://doi.org/10.1016/0921-5107(89)90172-4.

[46] G. Gordillo, L.M. Caicedo, G. Cediel, F. Landazabal, J.W. Sandino, Preparation and characterization of In_xSe_y thin films deposited by co-evaporation, Phys. Status Solidi 220 (1) (2000) 269–273, https://doi.org/10.1002/1521-3951(200007)220:1<269::AID-PSSB269>3.0.CO;2-9.

[47] M.C. Sharma, B. Tripathi, S. Kumar, S. Srivastava, Y.K. Vijay, Low cost CuInSe₂ thin films production by stacked elemental layers process for large area fabrication of solar cell application, Mater. Chem. Phys. 131 (3) (2012) 600–604, https://doi.org/10.1016/j.matchemphys.2011.10.023.

[48] R.W. Miles, M.T. Bhatti, K.M. Hynes, A.E. Baumann, R. Hill, Thin films of CdTe produced using stacked elemental layer processing for use in CdTe/CdS solar cells, Mater. Sci. Eng. B 16 (1–3) (1993) 250–256, https://doi.org/10.1016/0921-5107(93)90055-R.

[49] R. Niranjan, A. Banotra, N. Padha, Development of CuInSe₂ thin films by SELD method for photovoltaic absorber layer application, J. Mater. Sci. Mater. Electron. 31 (4) (2020) 3172–3183, https://doi.org/10.1007/s10854-020-02865-2.

[50] B.D. Cullity, S.R. Stock, Elements of X-Ray Diffraction, third ed., Prentice-Hall, Upper Saddle River, NJ, 2001.

[51] A.A. Abuelwafa, A. El-Denglawey, M. Dongol, M.M. El-Nahass, T. Soga, Influence of annealing temperature on structural and optical properties of nanocrystalline Platinum octaethylporphyrin (PtOEP) thin films, Opt. Mater. 49 (2015) 271–278, https://doi.org/10.1016/j.optmat.2015.09.032.

[52] F.A. Akgul, G. Akgul, N. Yildirim, H.E. Unalan, R. Turan, Influence of thermal annealing on microstructural, morphological, optical properties and surface electronic structure of copper oxide thin films, Mater. Chem. Phys. 147 (3) (2014) 987–995, https://doi.org/10.1016/j.matchemphys.2014.06.047.

[53] V.D. Mote, Y. Purushotham, B.N. Dole, Williamson-Hall analysis in estimation of lattice strain in nanometer-sized ZnO particles, J. Theor. Appl. Phys. 6 (6) (2012) 2–9, https://doi.org/10.1186/2251-7235-6-6.

[54] F. Ke, C. Liu, Y. Gao, J. Zhang, D. Tan, Y. Han, Y. Ma, J. Shu, W. Yang, B. Chen, H. K. Mao, X.J. Chen, C. Gao, Interlayer-glide-driven isosymmetric phase transition in compressed In₂Se₃, Appl. Phys. Lett. 104 (21) (2014) 212102, https://doi.org/10.1063/1.4879832.

[55] J. Weszka, Ph Daniel, A. Burian, A.M. Burian, A.T. Nguyen, Raman scattering in In₂Se₃ and InSe₂ amorphous films, J. Non-Cryst. Solids 265 (1–2) (2000) 98–104, https://doi.org/10.1016/S0022-3093(99)00710-3.

[56] A.H. Goldan, C. Li, S.J. Pennycook, J. Schneider, A. Blom, W. Zhao, Molecular structure of vapor-deposited amorphous selenium, J. Appl. Phys. 120 (13) (2016) 135101, https://doi.org/10.1063/1.4962315.

[57] M. Emziane, S. Marsillac, J. Ouerfelli, J.C. Bernede, R. Le Ny, γ-In₂Se₃, thin films obtained by annealing sequentially evaporated in and Se layers in flowing argon, Vacuum 48 (10) (1997) 871–878, https://doi.org/10.1016/S0042-207X(97)00094-8.

[58] C. Song, F. Fan, N. Xuan, S. Huang, C. Wang, G. Zhang, F. Wang, Q. Xing, Y. Lei, Z. Sun, H. Wu, H. Yan, Drastic enhancement of the Raman intensity in few-layer InSe by uniaxial strain, Phys. Rev. B 99 (19) (2019) 195414, https://doi.org/10.1103/PhysRevB.99.195414.

12

93

[59] S. Jandl, C. Carlone, Raman spectrum of crystalline InSe, Solid State Commun. 25 (1) (1978) 5–8, https://doi.org/10.1016/0038-1098(78)91157-2.

[60] O.S. Heavens, Optical properties of thin films, Rep. Prog. Phys. 23 (1960) 1–65, https://doi.org/10.1088/0034-4885/23/1/301.

[61] J. Clavijo, E. Romero, G. Gordillo, Effect of substrate temperature on the optical, structural and morphological properties of In_2Se_3 thin films grown by a two-step process, J. Phys. Conf. Ser. 167 (2009), 012016, https://doi.org/10.1088/1742-6596/167/1/012016.

[62] J. Tauc, R. Grigorovici, A. Vancu, Optical properties and electronic structure of amorphous germanium, Phys. Status Solidi 15 (1966) 627–637, https://doi.org/10.1002/pssb.19660150224.

[63] I.V. Bodnar, Optical properties of In_2Se_3 thin films, Semiconductors 50 (2016) 715–718, https://doi.org/10.1134/S1063782616060026.

[64] S.N. Sahu, Preparation, structure, composition, optical and photoelectrochemical properties of vacuum annealed In–Se thin films, Thin Solid Films 261 (1–2) (1995) 98–106, https://doi.org/10.1016/S0040-6090(95)06519-9.

[65] C. Jullien, A. Chery, D. Siapkas, Optical properties of In_2Se_3, phases, Phys. Status Solidi 118 (2) (1990) 553–559.

[66] J. Jalilian, M. Safari, Electronic and optical properties of α-InX (X = S, Se and Te) monolayer: under strain conditions, Phys. Lett. A 381 (15) (2017) 1313–1320, https://doi.org/10.1016/j.physleta.2017.01.024.

[67] P. Herve, L.K.J. Vandamme, General relation between refractive index and energy gap in semiconductors, Infrared Phys. Technol. 35 (4) (1994) 609–615, https://doi.org/10.1016/1350-4495(94)90026-4.

[68] D. Beena, K.J. Lethy, R. Vinodkumar, V.P. Mahadevan Pillai, V. Ganesan, D. M. Phase, S.K. Sudheer, Effect of substrate temperature on structural, optical and electrical properties of pulsed laser ablated nanostructured indium oxide films, Appl. Surf. Sci. 255 (20) (2009) 8334–8342, https://doi.org/10.1016/j.apsusc.2009.05.057.

[69] K. Assili, K. Alouani, X. Vilanova, Structural and optical properties of tin (II) sulfide thin films deposited using organophosphorus precursor (Ph3PS), Semicond. Sci. Technol. 32 (2) (2017), 025002, https://doi.org/10.1088/1361-6641/32/2/025002.

[70] S. Tripathi, B. Kumar, D.K. Dwivedi, Study on formation and characterization of kesterite CZTSSe thin films deposited by thermal evaporation technique for solar cell applications, J. Mater. Sci. Mater. Electron. 31 (4) (2020) 8308–8315, https://doi.org/10.1007/s10854-020-03366-y.

[71] Y. Leng, Materials Characterization: Introduction to Microscopic and Spectroscopic Methods, second ed., Wiley-VCH Verlag GmbH & Co., Germany, 2013, pp. 1–360.

[72] B.J. Inkson, Scanning electron microscopy (SEM) and transmission electron microscopy (TEM) for materials characterization, in: G. Hubschen, I. Altpeter, R. Tschuncky, H.G. Herrmann (Eds.), Materials Characterization Using Nondestructive Evaluation (NDE) Methods, first ed., Woodhead Publishing, United Kingdom, 2016, pp. 17–43.

[73] P.K. Kursula, Accuracy, precision and detection limits of SEM–WDS, SEM-EDS and PIXE in the multi-elemental analysis of medieval glass, X-Ray Spectrom. 29 (1) (2000) 111–118, https://doi.org/10.1002/(SICI)1097-4539(200001/02)29:1<111::AID-XRS430>3.0.CO;2-W.

[74] E.H. Putley, Hall Effect and Related Phenomena, first ed.s., Butterworths, London, 1960, pp. 1–263.

[75] L.J. van der Pauw, A method of measuring the resistivity and hall coefficient on lamellae of arbitrary shape, Philips Tech. Rev. 20 (1958) 220–224.

[76] S.O. Kasap, Photoreceptors: the chalcogenides, in: A.S. Diamond, D.S. Weiss (Eds.), The Handbook of Imaging Materials, second ed., Marcel Dekker, Inc., New York, 1998, pp. 329–368.

[77] D. Bidjin, S. Popovic, B. Celustka, Some Electrical and optical properties of In_2Se_3, Phys. Status Solidi 6 (1) (1971) 295–299, https://doi.org/10.1002/pssa.2210060133.

[78] M. Yudasaka, T. Matsuoka, K. Nakanishi, Indium selenide film formation by the double-source evaporation of indium and selenium, Thin Solid Films 146 (1) (1987) 65–73, https://doi.org/10.1016/0040-6090(87)90340-3.

[79] A. Chaiken, K. Nauka, G.A. Gibson, H. Lee, C.C. Yang, J. Wu, J.W. Ager, K.M. Yu, W. Walukiewicz, Structural and electronic properties of amorphous and polycrystalline In_2Se_3 films, J. Appl. Phys. 94 (4) (2003) 2390, https://doi.org/10.1063/1.1592631.

[80] S. Marsillac, J.C. Bernede, A. Conan, Change in the type of majority carriers in disordered $In_xSe_{100−x}$ thin-film alloys, J. Mater. Sci. 31 (1996) 581–587, https://doi.org/10.1007/BF00367872.

[81] J.W. Orton, M.J. Powell, The Hall effect in polycrystalline and powdered semiconductors, Rep. Prog. Phys. 43 (11) (1980) 1263–1307, https://doi.org/10.1088/0034-4885/43/11/001.

[82] J. Jerhot, V. Snejdar, Hall effect in polycrystalline semiconductors, Thin Solid Films 52 (3) (1978) 379–395, https://doi.org/10.1016/0040-6090(78)90181-5.

[83] Z.R. Khan, M. Zulfequar, M.S. Khan, Optical and structural properties of thermally evaporated cadmium sulphide thin films on silicon (1 0 0) wafers, Mater. Sci. Eng. B 174 (1–3) (2010) 145–149, https://doi.org/10.1016/j.mseb.2010.03.006.

[84] N. Memarian, S.M. Rozati, I. Concina, A. Vomiero, Deposition of nanostructured CdS thin films by thermal evaporation method: effect of substrate temperature, Materials 10 (7) (2017) 773, https://doi.org/10.3390/ma10070773.

[85] W. Mahmood, J. Ali, I. Zahid, A. Thomas, A. ul Haq, Optical and electrical studies of CdS thin films with thickness variation, Optik 158 (2018) 1558–1566, https://doi.org/10.1016/j.ijleo.2018.01.045.

[86] M. Ballabio, D.F. Marron, N. Barreau, M. Bonn, E. Canovas, Composition-dependent passivation efficiency at the CdS/$CuIn_{1−x}Ga_xSe_2$ interface, Adv. Mater. 32 (9) (2020) 1907763, https://doi.org/10.1002/adma.201907763.

[87] J.D. Major, R.T. Zaera, E. Azaceta, L. Bowen, K. Durose, Development of ZnO nanowire-based CdTe thin-film solar cells, Sol. Energy Mater. Sol. Cells 160 (2017) 107–115, https://doi.org/10.1016/j.solmat.2016.10.024.

[88] H. Cheng, H. Deng, Y. Wang, M. Wei, Influence of ZnO buffer layer on the electrical, optical and surface properties of Ga-doped ZnO films, J. Alloys Compd. 705 (2018) 598–601, https://doi.org/10.1016/j.jallcom.2017.01.172.

[89] Y.H. Jang, J.M. Lee, J.W. Seo, I. Kim, D.K. Lee, Monolithic tandem solar cells comprising electrodeposited $CuInSe_2$ and perovskite solar cells with a nanoparticulate ZnO buffer layer, J. Mater. Chem. A 5 (36) (2017) 19439–19446, https://doi.org/10.1039/c7ta06163c.

[90] T. Prasada Rao, M.C. Santhoshkumar, Effect of thickness on structural, optical and electrical properties of nanostructured ZnO thin films by spray pyrolysis, Appl. Surf. Sci. 255 (8) (2009) 4579–4584, https://doi.org/10.1016/j.apsusc.2008.11.079.

[91] G. Malik, S. Mourya, J. Jaiswal, R. Chandra, Effect of annealing parameters on optoelectronic properties of highly ordered ZnO thin films, Mater. Sci. Semicond. Process. 100 (2019) 200–213, https://doi.org/10.1016/j.mssp.2019.04.032.

[92] T. Nakada, M. Mizutani, 18% Efficiency Cd-Free Cu(In, Ga)Se_2 Thin-film solar cells fabricated using chemical bath deposition (CBD)–ZnS buffer layers, Jpn. J. Appl. Phys. 41 (2B) (2002) 165–167, https://doi.org/10.1143/JJAP.41.L165.

[93] K. Priya, G.K. Rao, V.K. Ashith, G. Sanjeev, V.P. Verma, V.C. Petwal, J. Dwivedi, The effect of 8 MeV electron beam irradiation on the structural, optical and photoluminescence properties of ZnS thin films, Ceram. Int. 45 (2A) (2019) 2576–2583, https://doi.org/10.1016/j.ceramint.2018.10.188.

[94] K. Chaitanya Kumar, S. Kaleemulla, Effect of Ni incorporation on structural, optical and magnetic properties of electron beam evaporated ZnS thin films, J. Phys. Chem. Solid. 135 (2019) 109028, https://doi.org/10.1016/j.jpcs.2019.05.025.

[95] P. Soni, M. Raghuwanshi, R. Wuerz, B. Berghoff, J. Knoch, D. Raabe, O. C. Miredin, Sputtering as a viable route for In_2S_3 buffer layer deposition in high-efficiency Cu(In, Ga)Se_2 solar cells, Energy Sci. Eng. 7 (2) (2019) 478–487, https://doi.org/10.1002/ese3.295.

[96] S. Campbell, Y. Qu, J. Gibbon, H.J. Edwards, V.R. Dhanak, D. Tiwari, V. Barrioz, N.S. Beattie, G. Zoppi, Defect limitations in $Cu_2ZnSn(S, Se)_4$ solar cells utilizing an In_2S_3 buffer layer, J. Appl. Phys. 127 (20) (2020) 205305, https://doi.org/10.1063/5.0002372.

[97] S.P. Nehra, S. Chander, A. Sharma, M.S. Dhaka, Effect of thermal annealing on physical properties of vacuum evaporated In_2S_3 buffer layer for eco-friendly photovoltaic applications, Mater. Sci. Semicond. Process. 40 (2015) 26–34, https://doi.org/10.1016/j.mssp.2015.06.049.

[98] S. Rasool, K. Saritha, K.T. Ramakrishna Reddy, M.S. Tivanov, A.V. Trofimova, S. E. Tikoto, L. Bychto, A. Patryn, M. Malinski, V.F. Gremenok, Effect of annealing on the physical properties of thermally evaporated In_2S_3 thin films, Curr. Appl. Phys. 19 (2) (2018) 108–113, https://doi.org/10.1016/j.cap.2018.11.016.

[99] S. Rasool, K. Saritha, K.T. Ramakrishna Reddy, L. Bychto, A. Patryn, M. Malinski, M.S. Tivanov, V.F. Gremenok, Optoelectronic properties of In_2S_3 thin films measured using surface photovoltage spectroscopy, Mater. Res. Express 6 (7) (2019), 076417, https://doi.org/10.1088/2053-1591/ab143b.

[100] N. Bouguila, M. Kraini, A. Timoumi, I. Halidou, C. Vazquez-Vazquez, M.A. Lopez-Quintela, S. Alaya, Substrate temperature effect on properties of sprayed In_2S_3 films, J. Mater. Sci. Mater. Electron. 26 (2015) 7639–7648, https://doi.org/10.1007/s10854-015-3403-7.

[101] C. Julien, M. Eddrief, K. Kambas, M. Balkanski, Electrical and optical properties of In_2Se_3 thin films, Thin Solid Films 137 (1) (1986) 27–37, https://doi.org/10.1016/0040-6090(86)90191-4.

94

Processing of nanocrystalline thin films of selenium and formation of FTO/p-Se/n-CdS/In heterojunctions for photovoltaic response

Rajesh Niranjan , Naresh Padha [*]

Department of Physics, University of Jammu, Jammu 180006, J&K, India

A B S T R A C T

Thin films of nanocrystalline selenium (Se) of different thicknesses were grown on annealing from 323 to 398 K. The crystallinity of the layers increased with annealing temperatures (T_A). The temperature thickness correlations were established. The layers exhibited spherical-shaped particles at higher annealing temperatures. The grown layers possess hexagonal crystal system with space group $P3_121(152)$; it shows prominent planes along the a-axis. The bandgap (E_g) decreases from 2.18 to 1.94 eV, 2.12 to 1.82 eV, and 2.13 to 1.84 eV with changes in T_A of 700, 270, and 150 nm thick layers, respectively. The high absorption coefficient (α) values $\sim 1 \times 10^5\,\mathrm{cm^{-1}}$ observed in all films makes it suitable as an absorber layer in a solar cell structure and an optical sensor. The FTO/p-Se/n-CdS/In heterojunction diodes provide zero-bias barrier height (ϕ_{bo}) of 0.788(7) eV. The open circuit voltage (V_{oc}) of FTO/p-Se (150 nm)/n-CdS(200 nm)/In a photovoltaic cell was observed to be 55 mV.

1. Introduction

Monochalcogenide selenium (Se) is considered the first semiconducting material that exhibited photoelectric conductivity in 1873 (Draper, 1873). The first technological use of Se was reported in a telegraph circuit as a small bar that acted as a photoelectric resistor (Smith, 1877). Due to its photo-conducting properties, the most important commercial application of grey, metallic Se, is seen in xerography (Kreel, 2012). Se-75 has been widely used in medical diagnostic procedures, biological tracing, and radio-nuclides detection due to its convenient gamma-ray counting. Its half-life is sufficient to detect complete chemical separation from other activities (Kreel, 2012). It has excellent optical and glass-forming properties. It is also used in chemical processing, agricultural, industrial, and pharmaceutical applications. Metallurgical grade selenium improves machinability, which helps to cast iron, copper, lead, and steel alloys. Its low melting point and high vapour pressure support low-cost commercial applications in photovoltaic and photoconductive device fabrications (Kreel, 2012; Ito et al., 1982). The first Se solar cell design was reported in 1954 with a power conversion efficiency (PCE) of 6 % by sandwiching the Se films between a metal and a thin gold foil (Hadar et al., 2019). Solar cells based on Se absorber layers could not compete with silicon counterparts. Se exhibits low photoconversion efficiency (PCE) than alternate absorber layers such as cadmium telluride (CdTe), copper indium diselenide (CIS),

copper indium gallium diselenide (CIGS), etc. However, Se offers various advantages over 'Si' and other materials in their growth. The Se provides better stability and protection to organic photovoltaic (OPV) and lead-halides perovskites from ambient humidity and oxygen (Stoumpos et al., 2013; Leijtens et al., 2015). The processing temperature for Se in the solar cell structure is below 473 K; moreover, it is much more easily grown than Si, CdTe, CIS, CIGS, and CZTSS materials (Stanbery, 2002; Jackson et al., 2011; Wang et al., 2014). Further, the Se in metal chalcogenide and chalcopyrite compounds has helped achieve a higher optical absorption coefficient (α) (Stanbery, 2002; Niranjan and Padha, 2021; Niranjan et al., 2020). Se in tandem organic photovoltaic (OPV) solar cells work as an ambient barrier and provide better charge carrier conduction, improving solar cell efficiency from 3.5 % to 6.5 % (Todorov et al., 2017). It has attracted the photovoltaic community because improvement in efficiency was possible with the optimisation of Se constituents in the materials during their processing (Niranjan and Padha, 2021). The growth of Se thin films has been reported using spin coating (Wang et al., 2014), chemical bath deposition (CBD) (Bindu et al., 2002), sputtering (Yuan et al., 1991), and physical vapour deposition (PVD) methods (Ito et al., 1982). The growth of Se thin layers is possible using thermal evaporation for low-cost, large-scale devices. Several researchers have started the development of Se thin films for structural optimisation to lead to a new dimension of their functional properties (Hadar et al., 2019; Chatterjee and Sen Gupta, 1986; Audiere
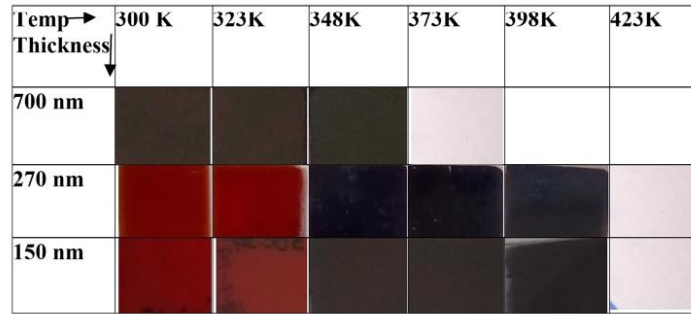
Fig. 1. The images of the nanocrystalline Se films having thicknesses 700, 270 and 150 nm as-deposited at 300 K and grown on annealing at different temperatures.

et al., 1979; Roy et al., 2006; Qasrawi et al., 2016). Se has been reported with a complex phase diagram of monoclinic Se_8 and trigonal Se_n and their mixture (Audiere et al., 1979; Fritts, 1897). However, trigonal selenium (t-Se) is the most suitable for solar cell applications (Hadar et al., 2019; Tutihasi and Chen, 1967). The morphological evolution during the crystallisation of Se films on thermal treatment was quite complicated (D'Almeida et al., 2000). Se's optical, electrical and current transport properties depend on the film preparation technique, deposition temperature, and post-deposition treatment (Legros et al., 1995). The use of amorphous selenium for photoconductivity has been reported by several authors (Draper, 1873; Hadar et al., 2019). However, efforts have been made by a few authors for the growth of polycrystalline Se thin layers for solar cell applications (Wang et al., 2014; Roy et al., 2006; Gates et al., 2002; Özenbaş, 1990). The thickness of the layers is kept below 1 μm due to the Se pill off tandency from the substrate. Some authors have used additional base adhesion layer like TiO_2 and Te, etc to overcome this short comings. Moreover, few authors have suggested the narrow temperature window optimisation for better crystallisation for future work (Hadar et al., 2019).

In the present work, an attempt has been made to grow nanocrystalline Se layers at room temperature. The 150, 270, and 700 nm layers were grown on the corning glass substrate. Further, the transformation of 'Se' from amorphous to polycrystalline form was carried out under a narrow temperature window for the layers deposited on corning and FTO-coated glass substrates. These layers were annealed up to 398 K; the temperature is lower than the previously reported processing temperature for polycrystalline Se layers. The optimised Se layers were used to fabricate FTO/p-Se/n-CdS/In heterojunction (HJ) diodes and photocells (PC), and their current–voltage characteristics of HJ and the photovoltaic response of PC were measured.

2. Experimental

The corning glass substrates used for film growth were cleaned using a hydrogen peroxide (H_2O_2) solution. These substrates were dipped for 10 min, followed by further treatment using trichloroethylene, acetone, and methanol (TAM) in a hot ultrasonic bath. The elemental Se having a purity of 99.99 % utilised for their thin layer growth on corning glass substrates using the thermal evaporation method at room temperature in a vacuum coating unit 12A4DM (HHV, India) at a vacuum pressure of $\sim 2 \times 10^{-6}$ mbar. The evaporation rate of Se during the growth was 4–6 Å/s. The in-situ substrate was given rotation with the help of a rotary motor attached to the substrate holder for the homogeneous growth of the films. Three different thicknesses of elemental Se, i.e., 700 nm, 270 nm, and 150 nm, were obtained. The post-deposition annealing of the layers was carried out in a tubular furnace under a vacuum of $\sim 1 \times 10^{-3}$ mbar at a temperature interval of 25 K from 323 K to 423 K for 1 hour (h) at each temperature. The complete evaporation of Se from the corning glass was observed at 373 K temperature for 700 nm. In comparison, the 270 and 150 nm films were evaporated at a higher temperature of 423 K
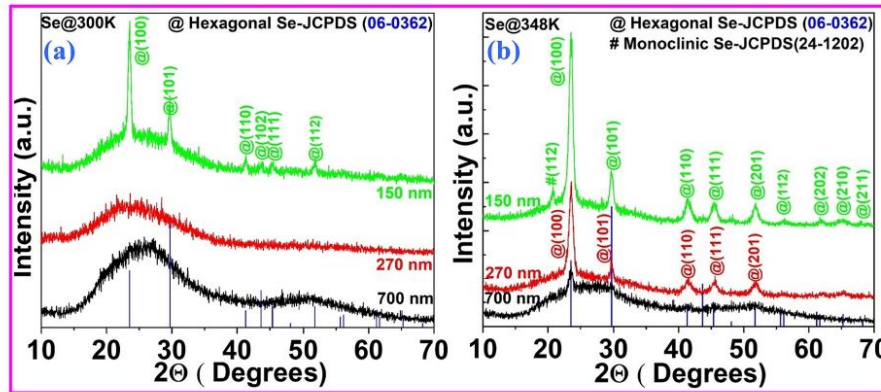

Fig. 2. a-b: The X-ray diffraction (XRD) patterns of nanocrystalline Se films having thicknesses of 700, 270 and 150 nm as-deposited at (a) 300 K and annealed at (b) 348 K.
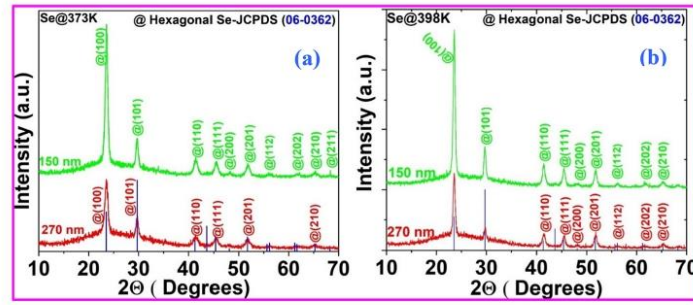
Fig. 3. a-b: The X-ray diffraction (XRD) patterns of nanocrystalline Se films having thicknesses of 270 and 150 nm annealed at (a) 373 K and (b) 398 K, respectively.

(Fig. 1). In the fabrication of the heterojunction diode, the 150 nm Se layer was deposited on FTO-coated glass, which was annealed at 398 K for one hour followed by the deposition of 200 nm thick CdS at room temperature. The thickness of as-deposited Se films was monitored with the help of a digital thickness monitor DTM-101 attached to VCU 12A4DM (HHV, India) using a 6 MHz quartz crystal sensor. The X-ray diffraction (XRD) data of the samples were recorded in a line scan mode in the '2θ' range of 10^0-70^0 with a scan rate of 0.03^0/s using filtered $CuK_{\alpha 1}$ radiations ($\lambda = 1.5406$ Å) in X'pert[3] (PANalytical) Powder X-ray diffractometer equipped with HD Bragg Brentano incident geometry. The optical data of the samples were recorded using UV–Vis-NIR spectrophotometer UV-3600 (Shimadzu) by keeping the source slit width at 2 nm in the transmission and absorbance mode. The transmission percentage was obtained in the 300–1800 nm wavelength range at room temperature. The surface morphology of 270 nm films was obtained using a scanning electron microscope (SEM) SUPRA-55 (Zeiss) on an acceleration voltage of 20 kV, and constituent elemental stoichiometric values were obtained by using an energy dispersive X-ray analysis (EDAX) attachment 7426 (Oxford) using L-emission line of selenium. Ohmic contacts were made on films using high-purity fine copper wires (99.999 %). Electrical measurements of the layers were performed by the two-probe method. The current–voltage (I-V) response of the

heterojunction diodes was measured using an automated setup consisting of a Keithley (2400) source meter fitted with a probe station (Miller Design Corp) using open-source I-V software developed by Michael D. Kelzenberg. The FTO/p-Se/n-CdS/In planar heterojunction diodes were tested in sunlight, and the open circuit voltage (V_{oc}) was recorded using a digital multimeter VC-203 (Victor). All experimental data analyses were accomplished using OriginLab 8.5 (MicroCal) software.

3. Results and discussion

3.1. Structural characterization

The physical appearance of the nanocrystalline Se layers having thickness values of 270 and 150 nm both change from red to brownish-black on annealing; the 700 nm layers appeared brown colour (Fig. 1). The X-ray diffraction (XRD) patterns of the nanocrystalline Se layers having thickness values of 700, 270, and 150 nm as deposited at 300 K are shown in Fig. 2a. The as grown layers of 150 nm show nanocrystalline behaviour. It exhibits the XRD peaks at '2θ' values of 23.50 (7), 29.65(4), 43.67(6) corresponding to (1 0 0), (1 0 1), and (1 1 0) planes as per JCPDS card no: 06–0362 whereas 270 and 700 nm films
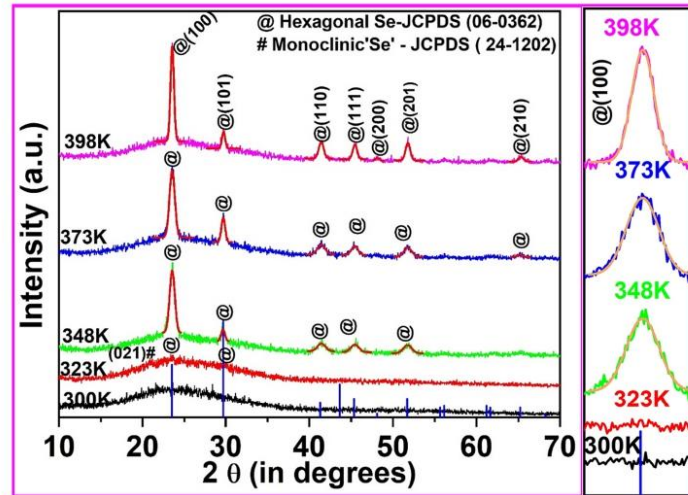

Fig. 4. The X-ray diffraction (XRD) patterns of as-deposited and annealed nanocrystalline Se films having thicknesses of 270 nm at 323, 348, 373 and 398 K.
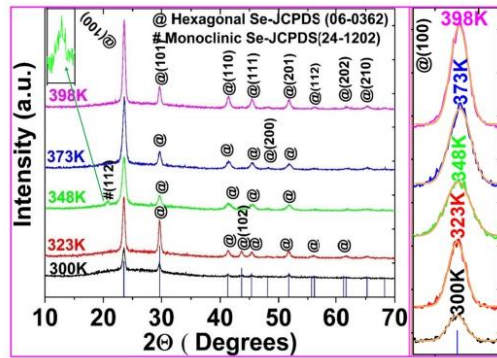
Fig. 5. The X-ray diffraction (XRD) patterns of as-deposited and annealed nanocrystalline Se films having thicknesses of 150 nm at 323, 348, 373 and 398 K.
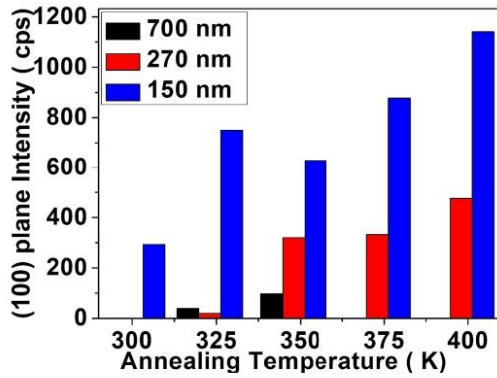

Fig. 6. The Intensity variations of the (1 0 0) planes with change in annealing temperature (T_a) of nanocrystalline Se layers.

show amorphous behaviour. The crystallinity of thin films is attained via nucleation, coalescence, and formation of channels. The present work achieves the polycrystalline form from thermal energy available at 300 K. In the case of films of 150 nm, energy available to the Se system is

more than the minimum requirement for nucleation and coalescence in the films. Further, the lowest energy required for the growth of the (1 0 0) peak is the reason for the higher intensity of this peak. However, the thermal energy available to the Se system of 270 and 700 nm films is insufficient for nucleation and coalescence; hence, these films are amorphous. The polycrystallinity in the 270 nm thick films emerges at 348 K. The 150 nm layers show comparatively higher crystallinity at this temperature. The 700 nm layer also showed crystallinity along (1 0 0) planes at 348 K (Fig. 2b), the film re-evaporates at 373 K (Fig. 1). Further, all prominent XRD peaks found matching with hexagonal Se (JCPDS card no. 06–0362), except, an additional (1 1 2) peak at 348 K of monoclinic Se (JCPDS card no. 24–1202). The phenomenon may be attributed to the recrystallization, which provides re-orientations of crystal growth on annealing at 348 K (Inset Fig. 5). Therefore, Se films appear as a mixed phase of hexagonal and monoclinic crystals. Moreover, the crystallinity of 150 and 270 nm layers increased significantly at 373 and 398 K (Fig. 3a-b). It is found that crystallinity exists in the nanosized layers of 150 and 270 nm; however, polycrystallinity is not observed in thicker (700 nm) layers at annealing temperatures of 373 and 398 K. The grown layers of Se possessed a hexagonal crystal system with space group P3$_1$21(152) as per JCPDS card no: 06–0362. The 150 nm Se layers even provided higher peak intensities than the 270 nm layers. Thus, the growth of polycrystalline Se layers occurs at higher annealing temperatures for thicker layers, i.e. the growth temperature of nanocrystalline layers increases with thickness. The best nanocrystalline Se layers were obtained at 398 K at a thickness value of 150 nm (Fig. 3b).

3.1.1. Effect of annealing temperature on the growth of nanocrystalline Se layer thickness

Figs. 4 and 5 show the X-ray diffraction patterns of 270 and 150 nm thick Se layers annealed from 323 to 398 K. The peak intensity of (1 0 0) most significant peak (MSP) increases with an increase in annealing temperature up to 398 K in both thickness values, thus providing dominant growth along the a-axis. Moreover, 150 nm layers are nanocrystalline at room temperature (300 K), providing a better response at each subsequent temperature up to 398 K.

The grain sizes of the (1 0 0) planes were calculated using the Scherrer formula in Eq. (1).

$$D = \frac{0.94\lambda}{\beta \cos\theta} \tag{1}$$

Where λ is the X-ray wavelength, β is the width at half maximum (FWHM) in radians, and θ; represents the Bragg angle. The unit cell parameters for hexagonal Se crystal systems were calculated using the relation in Eq. (2) (Cullity and Stock, 2014).

$$\frac{1}{d^2} = \frac{h^2}{a^2} + \frac{k^2}{b^2} + \frac{l^2}{c^2} \tag{2}$$

The microstrain (ε) and dislocation density (δ) present in the

Table 1

The position 2θ, full width at half maximum (FHWM), and crystallite sizes of the (1 0 0) nanocrystalline selenium layers having thicknesses of 700, 270, and 150 nm.

Film Thickness (nm)	Temperature (K)	2θ (^{0})	Intensity (cps)	FWHM (β) (^{0})	Crystallite size (D) (nm)
700	300			Amorphous	
	323	23.54(3)	29	0.5772(1)	15.68(1)
	348	23.56(4)	87	0.7578(5)	11.94(5)
270	300	Amorphous			
	323	Amorphous			
	348	23.55(3)	312	0.6955(1)	13.01(4)
	373	23.54(9)	333	0.6888(3)	13.14(1)
	398	23.55(5)	482	0.4764(3)	19.00(1)
150	300	23.50(7)	292	0.4853(1)	18.64(4)
	323	23.50(6)	742	0.4650(1)	19.46(1)
	348	23.53(4)	622	0.6680(2)	13.54(7)
	373	23.57(7)	867	0.5712(5)	15.84(7)
	398	23.55(9)	1139	0.4744(3)	19.07(9)

Se- (JCPDS No.:06-0362; Sys: Hexagonal; S.G.: P3$_1$21(152); Cell parameters: a = 4.366 Å, c = 4.953 Å; Vol-81.78 Å³.

4

Table 2
The microstrain (ε), dislocation density (δ), unit cell parameters (a, b, c), and cell volume (V) of 700, 270 and 150 nm thick nanocrystalline Se layers.

Film Thickness (nm)	Temperature (K)	Micro strain (ε) (x10^{-3})	Dislocation density (δ) (x10^{15})	Lattice Parameter (Å)		Cell Volume (V) (Å)^3
				a = b	c	
700	323	2.4655(2)	4.0669(5)	4.359(9)	4.8869(3)	80.500(0)
	348	3.2368(3)	7.0078(4)	4.356(1)	4.8288(1)	79.402(7)
270	348	2.9707(7)	5.9040(1)	4.358(2)	4.907(5)	80.778(1)
	373	2.9423(4)	5.7917(4)	4.357(5)	4.9180(9)	80.925(2)
	398	2.0347(5)	2.7695(9)	4.357(3)	4.936(6)	81.223(1)
150	300	2.0731(2)	2.8766(6)	4.366(5)	4.930(2)	81.458(7)
	323	1.9861(1)	2.6402(8)	4.366(7)	4.958(8)	81.938(8)
	348	2.8535(3)	5.4484(1)	4.361(1)	4.925(1)	81.189(1)
	373	2.4399(8)	3.9816(1)	4.353(7)	4.894(1)	80.389(5)
	398	2.0265(1)	2.7470(7)	4.357(1)	4.912(7)	80.817(1)

Se- (JCPDS No.:06–0362; Sys: Hexagonal; S.G.: P3$_1$21(152); Cell parameters: a = 4.366 Å, c = 4.953 Å; Vol-81.78 Å^3.
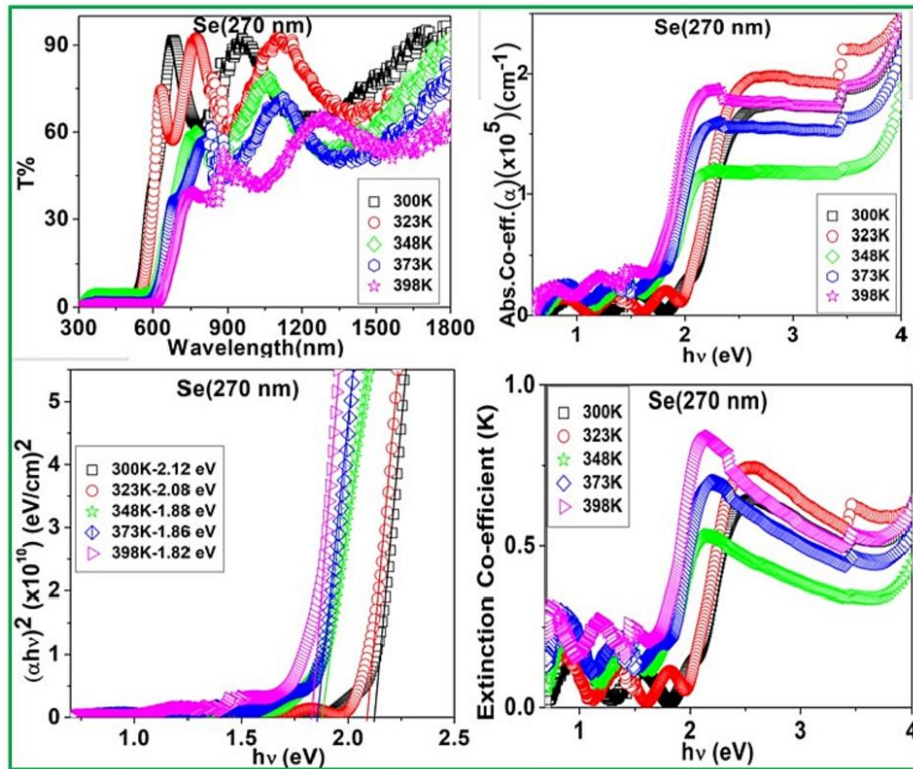
Fig. 7a. The transmission percentage (T%), absorption coefficient (α), optical absorption spectra [plots of (αhν)^2 versus photon energy *hν* (wavelength range 300–1800 nm)] and extinction coefficient (k) plot of as-deposited and annealed nanocrystalline Se films of 270 nm thickness.

nanocrystalline Se layers were calculated using the relation in Eqs. (3) and (4):

$$\varepsilon = \frac{\beta cos\theta}{4} \quad (3)$$

$$\delta = \frac{1}{D^2} \quad (4)$$

The trends in the variation of intensity of the (1 0 0) peak at different T$_A$ have been shown in bar chart form in Fig. 6. The variation in the grain size with a change in the annealing temperature is due to post-annealing nucleation on cooling from high to ambient temperature (Gates et al., 2002; Özenbaş, 1990). However, the grain size measured at different T$_A$ increases with a decrease in the Se layer thickness from 700 to 150 nm (Table 1). The parameters like cell volume, microstrain, and dislocation density have been given in Table 2; their values decrease with an increase in T$_A$ and layer thickness. Moreover, it is observed that the cell volume increases with a decrease in thickness at 348 K (Table 2).
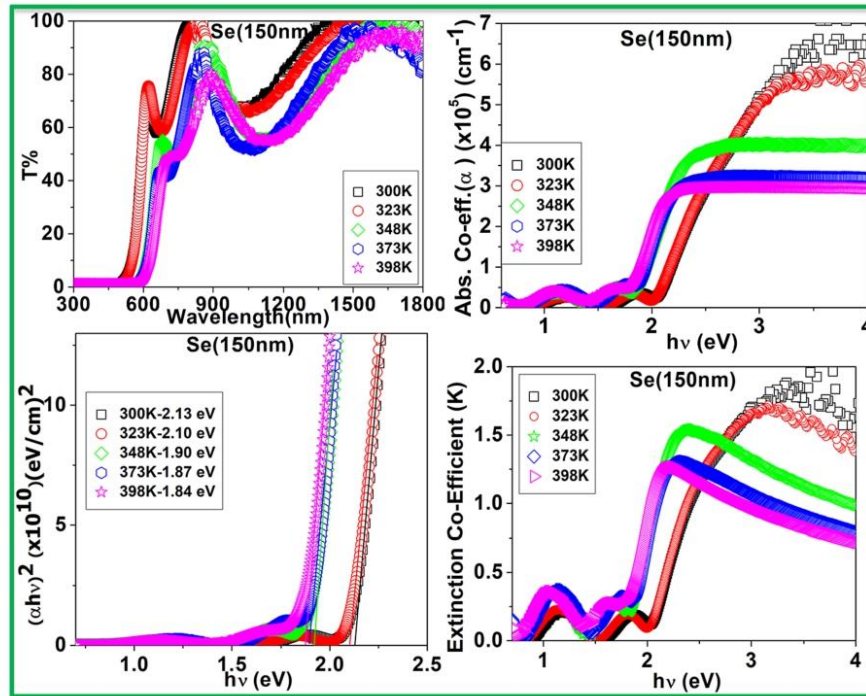
Fig. 7b. The transmission percentage (T%,) absorption coefficient (α), optical absorption spectra [plots of (αhυ)²versus photon energy *hυ* (wavelength range 300–1800 nm)] and extinction coefficient (k) plot of as-deposited and annealed nanocrystalline Se films of 150 nm thickness.

3.2. Optical studies

The fundamental absorption equivalent to an electron excitation from the valance band to the conduction band governs the value of the optical bandgap (E_g). The absorption coefficient (α) is calculated using the relation given in Eq. (5):

$$\alpha = \frac{1}{t} ln\left(\frac{100}{T\%}\right) \tag{5}$$

where t is the thickness of the layer on a substrate, and T% represents the transmission percentage of the incident photon. The optical bandgap (E_g) is calculated using the Tauc relation given in Eq. (6) (Tauc and Amorphous and Liquid Semiconductors, 1973).

$$\alpha h\upsilon = C\left(E_g - h\upsilon\right)^{1/2} \tag{6}$$

where α is the absorption coefficient, C; a constant, υ; the photon frequency and h; the Planck constant.

The optical bandgap (E_g) of the nanocrystalline layers is calculated by extrapolating the linear part of the curve of $(\alpha h\upsilon)^2 = f(h\upsilon)$ spectrum to the x-axis.

Figs. 7a-b show the transmission %, absorption co-efficient (α), optical absorption spectra [plots of $(\alpha h\upsilon)^2$ versus photon energy *hυ* (wavelength range 300–1800 nm)], and extinction coefficient (k) plot of as-deposited and annealed Se layers of 270 and 150 nm thickness, respectively. The optical bandgap of the as-deposited layers of polycrystalline Se having 150 nm thickness is 2.13 eV, which is higher than that of the amorphous Se (Bindu et al., 2002; Abdullaev et al., 1966). Some authors have reported that black Se bandgap values are 1.65 and

1.80 eV for monoclinic films (Hadar et al., 2019; Gates et al., 2002). The values of the bandgap of nanocrystalline layers of Se obtained at different annealing temperatures for different thicknesses have been presented in Table 3. The bandgap and absorption coefficient increase with a decrease in thickness in the layers; however, at a particular thickness, the bandgap decreases with an increase in the annealing temperature. The absorption coefficient at all annealing temperatures exhibits a value $> 1x10^5$ cm^{-1}. The maximum absorption at the optical transition edge was found in 270 nm thick films when the transmission was ~ 30 % for 398 K annealed samples. At the same time, the absorption coefficient (α) varied in the range 1-2x10^5 cm^{-1}, and the absorption coefficient (α) for 150 nm varied in the range 2.8-7 × 10^5 cm^{-1} with a slightly higher transmission percentage than 270 nm layers. The decrease in optical bandgap in the nanocrystalline Se causes low-energy photons to transit from the valence to the conduction band; this phenomenon may help the material to provide better efficiency in solar cell applications.

The extinction coefficient (k) determines the degree of surface uniformity and specifies how effectively light of a particular wavelength (λ) is absorbed in the material. It also resembles the information about surface smoothness. The extinction coefficient (k) values were calculated using the expression given in Eq. (7) (Niranjan and Padha, 2021; Banotra, 2017).

$$k = \frac{\alpha\lambda}{4\pi} \tag{7}$$

where α is the absorption coefficient, λ represents the wavelength of the incident photon.

The extinction coefficient (k) values variation was (0.54–0.42),
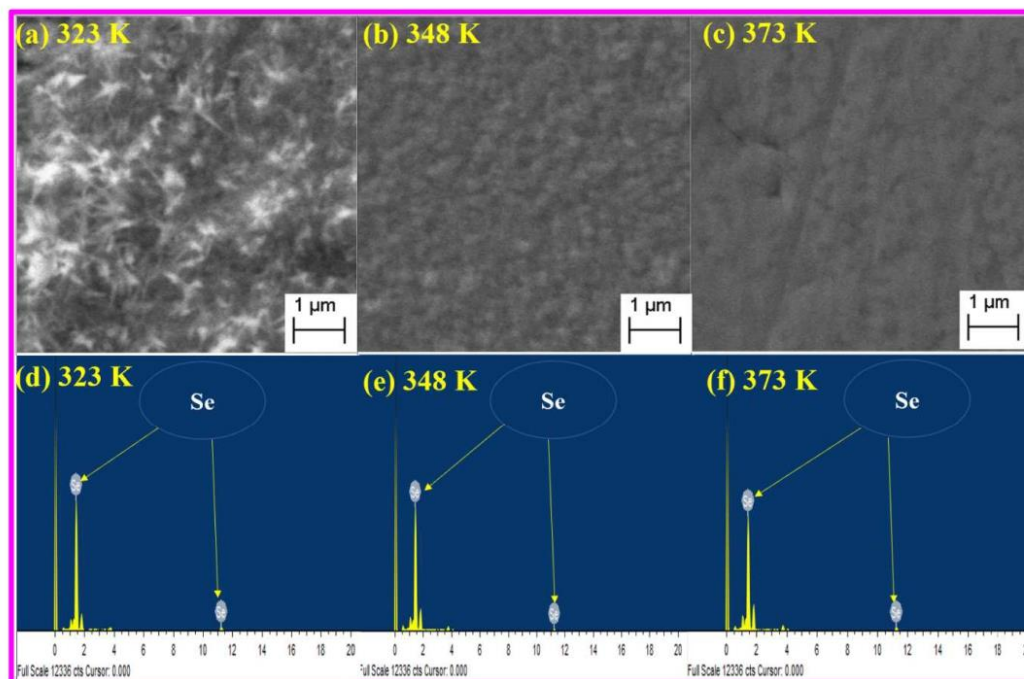
6

100

Fig. 8. The scanning electron microscopic (SEM) images of nanocrystalline Se films obtained at (a) 323 K, (b) 348 K and (c)373 K and the EDAX Spectra of Se at an annealing temperature of (d) 323 K, (e) 348 K and (f) 373 K.
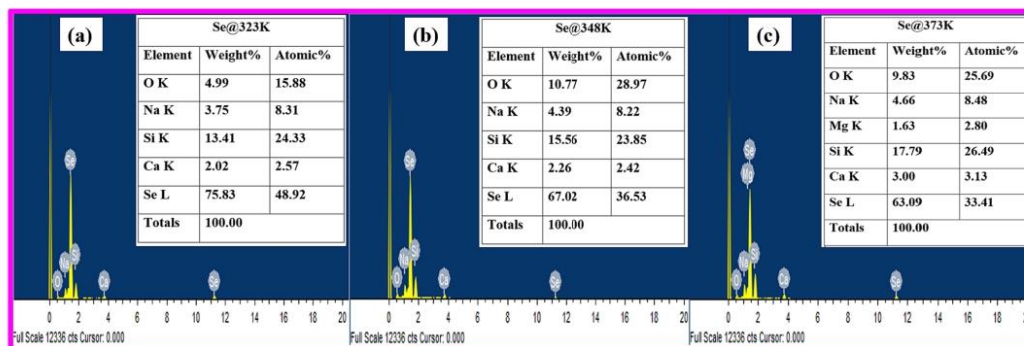

Fig. 9. The atomic and weight percentage values of energy dispersive X-ray analysis (EDAX) spectra of nanocrystalline Se films and the substrate constituents obtained at (a) 323 K, (b) 348 K and (c) 373 K.

(0.60–0.80), and (2.0–1.25) for 700, 270, and 150 nm Se obtained at different annealing temperatures (Table 3). The reduction in k values shows a smoother surface of the films. The higher value of k for 150 nm thin layers is due to the high absorption coefficient. This high absorption coefficient value of the 150 nm thick films is related to the texture of the surface of the layers. The obtained nanocrystalline Se exhibited an absorption coefficient (α) > 10^5 cm^{-1}, suitable for an optical sensor application and an absorber layer in a solar cell in the visible region.

3.3. Morphological and compositional analysis

Scanning electron microscopy (SEM) determined the surface morphology of the nanocrystalline Se layers of 270 nm. Fig. 8a-c show SEM images of the undertaken Se layers annealed at 323 to 373 K. At 323 K, the layers show bright images of irregularly shaped particles with voids that look like cotton flowers. The nucleation occurs between 348 and 373 K, and the crystallites can be seen possessing spherical-shaped grains. The density of voids decreases with an increase in the annealing
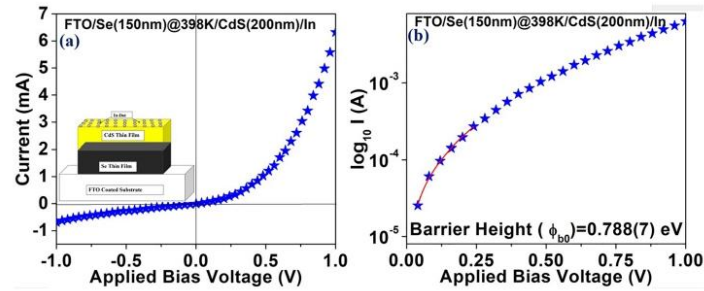
7

101

Fig. 10. (a) The simple and (b) semi log current–voltage (I-V) characteristics of FTO/p-Se/n-CdS/In heterojunction diode of 150 nm thick nanocrystalline Se layer grown at T_A of 398 K.
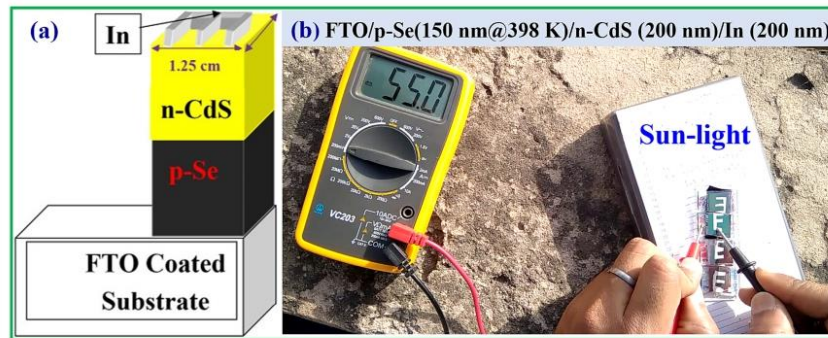

Fig. 11. (a) The 3D schematic diagram of FTO/p-Se/n-CdS/In heterojunction photovoltaic cell and (b) open circuit voltage (V_{oc}) in sunlight using a digital multimeter for 150 nm thick Se absorber layer (T_A at 398 K).

Table 3
The bandgap (E_g), critical wavelength (λ_c), absorption coefficient (α) and extinction coefficient (k) of nanocrystalline Se layers having thicknesses of 700, 270 and 150 nm.

Thickness	Temperature (K)	E_g (eV)	Critical wavelength (λc)	Abs. Co-eff. (α) (cm^{-1}) (x10^5)	Extinction coefficient (k)
700	300	2.08	596	1.0	0.54
	323	2.06	602	1.0	0.48
	348	1.94	639	1.1	0.42
270	300	2.12	585	1.5	0.60
	323	2.08	596	2.0	0.75
	348	1.88	660	1.0	0.55
	373	1.86	667	1.5	0.70
	398	1.82	681	1.8	0.80
150	300	2.13	582	7.0	2.0
	323	2.10	590	6.0	1.75
	348	1.90	653	4.0	1.60
	373	1.87	663	3.0	1.30
	398	1.84	674	2.8	1.25

temperature, exhibiting a smoother surface over the layers (Audiere et al., 1979). No significant variation in grain size was observed on increasing the temperature from 348 to 373 K; however, variation in the texture of the surface was observed with an increase in T_A. The Se has been reported as a liquid phase with a decreasing mean chain length of Se_8 with an increase in temperature from 217 to 653 K (Baker, 1968). A similar effect may cause a decrease in the density of voids and grain boundaries, which was prominently detected in surface morphology with the increase in annealing temperature.

Fig. 8d-f show the EDAX spectra of nanocrystalline Se layers of 270 nm obtained at 323–373 K. The energy dispersive X-ray analysis (EDAX) spectra confirm the availability of Se at each temperature. Fig. 9a-c show constituents' atomic percentage (at. %) and weight percentage (wt %) in the scanned portion. The qualitative results of EDAX spectra exhibit the presence of some other elements which constitute substrate (Kuisma-Kursula, 2000). Regarding EDAX, weight percentage (wt %) decreases with an increase in annealing temperature, indicating re-evaporation of Se. The 150 nm Se layers were expected to provide similar morphology and compositional analysis results. Therefore, their studies were not repeated while 700 nm layers were amorphous, almost in the entire T_A

range.

3.4. The current transport behaviour of FTO/p-Se/n-CdS/In heterojunction

The nanocrystalline Se layers of 150 nm were obtained on annealing over the FTO-coated glass substrate at 398 K. The CdS thin films of 200 nm were deposited on these layers, followed by In (indium) deposition of 200 nm using a physical mask. Fig. 10a-b show current–voltage characteristics of FTO/p-Se/n-CdS/In heterojunction diode, which exhibited rectifying behaviour with low barrier potential; It provides zero-bias barrier height (ϕ_{bo}) of 0.788(7) eV. The solar cell structure of the corresponding FTO/p-Se/n-CdS/In heterojunction is shown in Fig. 11a. The area of the pn-heterojunction was measured at ~ 1 cm^2. The FTO/p-Se/n-CdS/In solar cell having absorber layer thickness ~ 150 nm obtained at 398 K confirms the photoconductive process in the sunlight and provided open circuit voltage (V_{oc}) of 55 mV using a digital multimeter (Fig. 11b).

4. Conclusion

Nanocrystalline Se layers were grown by annealing the layers deposited by thermal deposition technique under a high vacuum at room temperature and higher temperatures. These layers exhibited bandgap tuning from 2.13 to 1.83 eV and absorption coefficient > 1x10^5 cm^{-1}. The crystallinity of the layers increases with increasing annealing temperature and decreasing thickness. The average grain size corresponding to the MSP (1 0 0) planes varies from 13.01(4) to 19.46(1) nm. The open-circuit voltage (V_{oc}) value of FTO/p-Se/n-CdS/In heterojunction solar cell structure was 55 mV for nanocrystalline Se layers of 150 nm grown at 398 K.

CRediT authorship contribution statement

Rajesh Niranjan: Conceptualization, Data curation, Formal analysis, Investigation, Software, Visualization, Methodology, Writing - original draft. **Naresh Padha:** Funding acquisition, Project administration, Resources, Supervision, Validation, Visualization, Writing - review & editing.

Declaration of Competing Interest

The authors declare that they have no known competing financial interests or personal relationships that could have appeared to influence the work reported in this paper.

Data availability

Data will be made available on request.

References

Abdullaev, G.B., Aliev, G.M., Mekhtieva, S.I., Abdinov, D.S., 1966. Effect of Admixtures on Some Physical Properties of Selenium. Phys. Status Solidi 13, K109–K113. https://doi.org/10.1002/pssb.19660130241.
Audiere, J.P., Mazieres, C., Carballes, J.C., 1979. Ageing and crystallisation of non-crystalline Se thin films: A tentative structural model. J. Non Cryst. Solids 34, 37–51. https://doi.org/10.1016/0022-3093(79)90005-X.
Baker, E.H., 1968. The vapour pressure and resistivity of selenium at high temperatures. J. Chem. Soc. A Inorganic, Phys. Theor. 4, 1089–1092. https://doi.org/10.1039/J19680001089.
Banotra, A., 2017. Effect of annealing on the physical characteristics of the vacuum evaporated SnxSy mixed phase thin films. Mater. Res. Express. https://doi.org/10.1088/2053-1591/aa982e.
Bindu, K., Lakshmi, M., Bini, S., Kartha, C.S., Vijayakumar, K.P., Abe, T., Kashiwaba, Y., 2002. Amorphous selenium thin films prepared using chemical bath deposition: Optimisation of the deposition process and characterisation. Semicond. Sci. Technol. 17, 270–274. https://doi.org/10.1088/0268-1242/17/3/316.
Chatterjee, E., Sen Gupta, S.P., 1986. Amorphous to crystalline phase transition of vapour grown selenium films. J. Mater. Sci. Lett. 5, 559–561. https://doi.org/10.1007/BF01728690.
Cullity, B.D., Stock, S.R., 2014. Elements of X-Ray Diffraction, 3rd ed. Pearson New Internation Edition, London.
D'Almeida, K., Napo, K., Safoula, G., Ouro Djobo, S., Bernede, J.C., 2000. Crystallisation of selenium thin films doped with iodine after evaporation. J. Mater. Sci. 35, 2985–2991. https://doi.org/10.1023/A:1004730811005.
Draper, H.N., 1873. Effect of light on the electric conductivity of selenium. Nature 7, 340. https://doi.org/10.1038/007340e0.
Fritts, C.E., 1897. On a new form of selenium cell, and some electrical discoveries made by its use. Am. J. Sci. 5, 888–889. https://doi.org/10.1126/science.5.127.888.
Gates, B., Mayers, B., Cattle, B., Xia, Y., 2002. Synthesis and characterisation of uniform nanowires of trigonal selenium. Adv. Funct. Mater. 12, 219–227. https://doi.org/10.1002/1616-3028(200203)12:3<219::AID-ADFM219>3.0.CO;2-U.
Hadar, I., Bin Song, T., Ke, W., Kanatzidis, M.G., 2019. Modern Processing and Insights on Selenium Solar Cells: The World's First Photovoltaic Device. Adv. Energy Mater. 9, 1–9. https://doi.org/10.1002/aenm.201802766.
Ito, H., Oka, M., Ogino, T., Takeda, A., Mizushima, Y., 1982. Selenium Thin Film Solar Cell. Jpn. J. Appl. Phys. 21, 77. https://doi.org/10.7567/JJAPS.21S2.77.
Jackson, P., Hariskos, D., Lotter, E., Paetel, S., Wuerz, R., Menner, R., Wischmann, W., Powalla, M., 2011. New world record efficiency for Cu(In, Ga)Se 2 thin-film solar cells beyond 20%. Prog. Photovolt. Res. Appl. 19, 894–897. https://doi.org/10.1002/pip.1078.
Kreel, L., 2012. Webb's physics of medical imaging, 2nd ed. CRC Press, London.
Kuisma-Kursula, P., 2000. Accuracy, precision and detection limits of SEM-WDS, SEM-EDS and PIXE in the multi-elemental analysis of medieval glass. X-Ray Spectrom. 29, 111–118. https://doi.org/10.1002/(SICI)1097-4539(200001/02)29:1<111::AID-XRS408>3.0.CO;2-W.
Legros, A., Shi, M.K., Mouton, A., Selmani, A., 1995. Effect of water impurity on the crystallisation of vacuum evaporated Se. J. Appl. Phys. 78, 3048–3051. https://doi.org/10.1063/1.360055.
Leijtens, T., Eperon, G.E., Noel, N.K., Habisreutinger, S.N., Petrozza, A., Snaith, H.J., 2015. Stability of metal halide perovskite solar cells. Adv. Energy Mater. 5, 1–23. https://doi.org/10.1002/aenm.201500963.
Niranjan, R., Banotra, A., Padha, N., 2020. Development of CuInSe2 thin films by SELD method for photovoltaic absorber layer application. J. Mater. Sci. Mater. Electron. 31, 3172–3183. https://doi.org/10.1007/s10854-020-02865-2.
Niranjan, R., Padha, N., 2021. Growth of γ- In2Se3 monolayer from multifaceted InxSey thin films via annealing and study of its physical properties. Mater. Chem. Phys. 257, 123823 https://doi.org/10.1016/j.matchemphys.2020.123823.
Özenbaş, M., 1990. Amorphous-to-crystalline transition of selenium thin films deposited onto aluminum substrates. Vacuum 41, 1339–1342. https://doi.org/10.1016/0042-207X(90)93951-E.
Qasrawi, A.F., Kayed, T.S., Elsayed, K.A., 2016. Properties of Se/InSe Thin-Film Interface. J. Electron. Mater. 45, 2763–2768. https://doi.org/10.1007/s11664-016-4414-8.
Roy, R., Choudhary, V.S., Patra, M.K., Pandya, A., 2006. Effect of annealing temperature on the electrical and optical properties of nanocrystalline selenium thin films. J. Optoelectron. Adv. Mater. 8, 1352–1355.
Smith, W., 1877. "Selenium", its electrical qualities and the effect of light thereon. J. Soc. Telegr. Eng. 6, 423–441. https://doi.org/10.1049/jste-1.1877.0033.
Stanbery, B.J., 2002. Copper indium selenides and related materials for photovoltaic devices. Crit. Rev. Solid State Mater. Sci. 27 https://doi.org/10.1080/20014091104215.
Stoumpos, C.C., Malliakas, C.D., Kanatzidis, M.G., 2013. Semiconducting tin and lead iodide perovskites with organic cations: Phase transitions, high mobilities, and near-infrared photoluminescent properties. Inorg. Chem. 52, 9019–9038. https://doi.org/10.1021/ic401215x.
J. Tauc, Amorphous and Liquid Semiconductors, (1973) Plenum Press, London. 10.1080/715120893.
Todorov, T.K., Singh, S., Bishop, D.M., Gunawan, O., Lee, Y.S., Gershon, T.S., Brew, K.W., Antunez, P.D., Haight, R., 2017. Ultrathin high band gap solar cells with improved efficiencies from the world's oldest photovoltaic material. Nat. Commun. 8 https://doi.org/10.1038/s41467-017-00582-9.
Tutihasi, S., Chen, I., 1967. Optical properties and band structure of trigonal selenium. Phys. Rev. 158, 623–630. https://doi.org/10.1103/PhysRev.158.623.
Wang, K., Shi, Y., Zhang, H., Xing, Y., Dong, Q., Ma, T., 2014. Selenium as a photo absorber for inorganic-organic hybrid solar cells. PCCP 16, 23316–23319. https://doi.org/10.1039/c4cp02821j.
Yuan, X.L., Min, S.W., Fang, Z.Y., Yu, D.W., Qi, L., 1991. Growth of rf-sputtered selenium thin films. Int. Conf. Thin Film Phys. Appl. 1519, 167. https://doi.org/10.1117/12.47330.

9